UNIVERSITY OF CALIFORNIA

Los Angeles

Polar Cap Precursor of Nightside Meso-scale Auroral Enhancements

A dissertation submitted in partial satisfaction of the

requirements for the degree Doctor of Philosophy

in Atmospheric and Oceanic Sciences

by

Ying Zou

2015

ABSTRACT OF THE DISSERTATION

Polar Cap Precursor of

Nightside Meso-scale Auroral Enhancements

by

Ying Zou

Doctor of Philosophy in Atmospheric and Oceanic Sciences

University of California, Los Angeles, 2015

Professor Lawrence R. Lyons, Chair

Although the large-scale auroral oval has been well examined, what controls the occurrence of meso-scale enhanced auroras remains ambiguous. The answer is critical for forecasting ionospheric scintillation and remote-sensing magnetospheric disturbances. One important meso-scale auroral enhancement is poleward boundary intensifications (PBIs), which are intensifications along the poleward boundary of the nightside auroral oval and are produced by magnetic reconnection, a fundamental energy conversion process in the magnetosphere. This thesis is dedicated to understand when and where PBIs and the associated magnetotail reconnection occur, spontaneously or driven by external forcing, based on coordinated observations of all-sky imagers (ASIs) and radars. We found that the occurrence of PBIs is consistently accompanied with narrow and fast flows near the auroral poleward boundary in the polar cap. They occur simultaneously with or 1–2 min before PBIs near the PBI longitude, and direct equatorward toward the auroral poleward boundary. They have a duration and width

comparable to those of PBIs. Although the prior flow evolution could not be obtained based on the limited radar field-of-view, a polar cap ASI can substantially expand our observing area by enabling flow tracing using airglow patches and polar cap arcs. It shows that deep in the polar cap, localized fast flows typically propagate at ~600 m/s, persist tens of minutes to hours, and are of a few hundred km width. They appear as channels of flow enhancements that are elongated in the noon-midnight meridian, and significantly contribute to magnetic flux convection across the polar cap. The mosaic ASI images further show that as these fast flow propagate equatorward from the magnetic pole and impinge on the nightside auroral poleward boundary, they are followed by intensifications within the auroral oval that are spatially connected to them and occur within a few minutes and <~ 10° longitudes. Such intensifications are major disturbances that do not occur until the impingement of polar cap flows, suggesting the intensifications to be triggered by these flows. Our results suggest that locally enhanced nightside auroras, and the associated magnetic reconnection, can be preceded by, and developed around, localized flow enhancements arriving at the auroral poleward boundary from the polar cap. This preceding signature in the polar cap is essential to understand the development of magnetotail reconnection, and gives the potential of forecasting the specific time and location of disturbances in the magnetosphere and ionosphere. The existence and importance of such polar cap precursor were not recognized in the past due to the lack of coordinated radar and ASI observations, as well as broadly covered mosaic from an ASI array.

The dissertation of Ying Zou is approved.

Richard M. Thorne

Vassilis Angelopoulos

Yukitoshi Nishimura

Lawrence R. Lyons, Committee Chair

University of California, Los Angeles

2015

Dedicated to all those who opened my eyes and made me fly.

Table of Contents

Acknowledgement

In full gratitude I would like to acknowledge Larry Lyons and Toshi Nishimura who have always instructed me with love. They always seek out the good in me and believe in me even more than I do. They are prominent scientists I truly admire, and their creativity, diligence, and passion in research enlighten my Ph.D. pursuit. I would also thank the rest of my thesis committee, Vassilis Angelopoulos and Richard Thorne, for all the insightful and encouraging comments and the wonderful classes they taught.

I would like to thank my parents. They are always a phone call away, and patiently listen and know just what to say. They have taught me to embrace the beauty of this world, and to me, the most beautiful thing is to have parents like them.

I want to thank my husband for appreciating me as I am, and building a fairytale life full of love.

Lastly, my sincere thanks go to my grandparents and my dogs who were always proud of me no matter what, although they did not live to see this.

Ying Zou

Los Angeles, California

September 4, 2015

Vita

Education

2012 Master of Space Sciences

Department of Atmospheric and Oceanic Sciences

University of California, Los Angeles, United States

2010 Bachelor of Space Sciences

School of Earth and Space Sciences

Peking University, Beijing, China

Employment

2011-2015 Graduate Student Research Assistant

2014 Teaching Assistant

Publication

Zou, Y., Y. Nishimura, L. R. Lyons, E. F. Donovan, K. Shiokawa, J. M. Ruohoniemi, K. A. McWilliams, and N. Nishitani (2015), Polar Cap Precursor of Nightside Auroral Oval Intensifications Using Polar Cap Arcs. J. Geophys. Res. Space Physics, submitted

Zou, Y., Y. Nishimura, L. R. Lyons, K. Shiokawa, E. F. Donovan, J. M. Ruohoniemi, K. A. McWilliams, and N. Nishitani (2015), Localized polar cap flow enhancement tracing using airglow patches: Statistical properties, IMF dependence, and contribution to polar cap convection. J. Geophys. Res. Space Physics,120, 4064–4078. doi: 10.1002/2014JA020946.

Zou, Y., Y. Nishimura, L. R. Lyons, E. F. Donovan, J. M. Ruohoniemi, N. Nishitani, and K. A. McWilliams (2014), Statistical relationships between enhanced polar cap flows and PBIs, J. Geophys. Res. Space Physics, 119,151–162, doi:10.1002/2013JA019269.

Zou, Y., Y. Nishimura, L. R. Lyons, and E. F. Donovan (2012), A statistical study of the relative locations of electron and proton auroral boundaries inferred from meridian scanning photometer observations, J. Geophys. Res., 117, A06206, doi:10.1029/2011JA017357.

Wang, B; Y. Nishimura, L. R. Lyons; Y. Zou; H. C. Carlson; H. U. Frey; S. B. Mende (2015), Analysis of close conjunctions of dayside polar cap airglow patches and flow channels by all-sky imager and DMSP, J. Geophys. Res. Space Physics, submitted

Nishimura, Y., et al. (2014), Day-night coupling by a localized flow channel visualized by polar cap patch propagation, Geophys. Res. Lett., 41, 3701–3709, doi:10.1002/2014GL060301.

Lyons, L. R., Y. Nishimura, B. Gallardo-Lacourt, Y. Zou, E. Donovan, S. Mende, V. Angelopoulos, J. M. Ruohoniemi, and K. McWilliams (2013), Westward traveling surges: Sliding along boundary arcs and distinction from onset arc brightening, J. Geophys. Res. Space Physics, 118, 7643–7653, doi:10.1002/2013JA019334.

Chapter 1. General Introduction

1.1 Aurora and Airglow

Aurora is caused by energetic (hundreds of eV to a few tens of keV) electrons and protons precipitating from the magnetosphere into the Earth's upper atmosphere. The precipitating particles ionize, dissociate, and excite ambient atmospheric neutrals, and the resultant products at excited states then deposit their excess energy into heat and into radiation [see flow chart in *Rees and Luckey,* 1974]. Depending on the type of the product and on the level of excitement, the radiated emissions occur in various wavelengths, giving the spectacular display of colors. The nightside auroral characteristic green-yellow (557.7 nm) and red (630.0 nm) colors come from atomic oxygen emissions. Emissions from atomic hydrogens (Hα, Hβ, Hγ) have also been detected and are produced by precipitating protons capturing an electron through charge exchange. Most nightside auroral emissions are radiated from an altitude range from 100 to 150 km, the specific profile being determined by the energy and the pitch angle distribution of precipitating particles, and the atmospheric composition [*Ree et al.*, 1976, 1977; *Lummerzheim et al.*, 2002]. Red line (630.0 nm) emissions tend to be emitted from relatively high altitude (150-300 km) [*Rees and Roble*, 1986; *Solomon et al.*, 1988], although the corresponding excitation can peak at lower altitudes. This is because the radiative lifetime of 630.0 nm is so long that the excited atom is likely to encounter de-excitation through the frequent collisions at low altitude. The intensity of auroral luminosity is determined by the energy flux of precipitation.

Aurora generally occurs within a continuous band (most likely ~67°-77° in geomagnetic latitude) circling the geomagnetic pole on each hemisphere, appearing as structureless diffuse luminosity or as clear-cut discrete structures, as seen in Figure 1.1. Diffuse aurora, although

faint, spreads over the entire auroral oval, i.e. being large-scale (thousands of km scale size), and exists almost permanently. The diffuse electron precipitation arises from scattering of magnetospheric trapped electrons into the atmospheric loss cone by electromagnetic waves [*Kennel et al.*, 1970; *Johnstone et al.*, 1993]. Although wave-particle interaction also leads to proton precipitation [e.g. *Fuselier et al.*, 2004; *Xiao et al.*, 2014], protons are predominantly scattered by stretched magnetic field lines that have a curvature comparable to the proton gyro radius [*Sergeev and Tsyganenko*, 1982; *Gilson et al.*, 2012]. Today's high resolution optical measurement suggests that diffuse electron aurora is actually finely structured, containing azimuthal luminous stripes of ~5-km width [*Sergienko et al.*, 2008]. Despite of the faintness, diffuse aurora dominates the precipitation energy input into the atmosphere [*Newell et al.*, 2009].

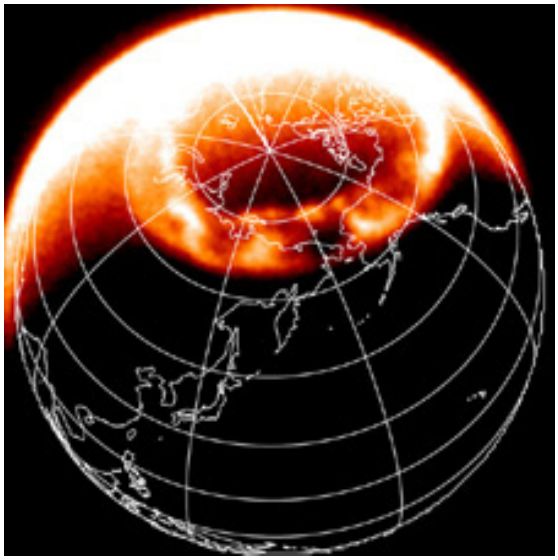

Figure 1.1 Electron auroral observation at northern hemisphere acquired with the Far-Ultraviolet Wideband Imaging Camera on the IMAGE spacecraft (http://www-spof.gsfc.nasa.gov/).

On the other hand, discrete auroras are enhanced in intensity and exhibit a wide variety of forms rapidly evolving on a time scale of a few to tens of minutes. Each discrete aurora is typically of tens to hundreds km scale size, i.e. being meso-scale. The discrete precipitation is produced by locally accelerated electrons through an electrostatic field parallel to the magnetic field vector. Such electric field is broadly distributed in altitude over thousands of km above the aurora, and can at times become substantially enhanced at certain thin layers (tens km) [e.g.

Hull et al., 2003], giving a total parallel potential of 1-10 kV. This field is caused by a shear in plasma bulk velocity and/or a gradient in plasma kinetic pressure in the magnetosphere [*Echim et al.*, 2009], both being common and important convection features [e.g. *Angelopoulos et al.*, 1992; *Xing et al.*, 2009]. The shear/gradient generates field-aligned currents connecting to the ionosphere, downward currents carried by upgoing ionospheric electrons and upward currents by downgoing magnetospheric electrons. The upward currents at low altitude is maintained by the electrostatic field, which functions to accelerate electrons downward and thus to prevent them from being repelled by magnetic mirror force [*Knight*, 1973]. Transient parallel electric field, carried by dispersive Alfvén waves, also produces discrete precipitation; however, it has a hundred-meter horizontal scale [e.g. *Wygant et al.,* 2002], as compared to the common kilometer scale. Recent studies suggest that the two types of accelerations are not distinct from each other, but rather the electrostatic acceleration can develop out of the transient one [*Hull et al.*, 2010; *Mella et al.*, 2011].

Auroras can thus almost instantaneously reflect and depict configurations and physical processes in the magnetosphere. The equatorward boundary of nightside diffuse proton auroras is demonstrated to well correspond to, and thus signify the inclination of magnetic field line near the equatorial plane [*Sergeev and Gvozdevsky, 1995*; *Donovan et al.*, 2003]. The equatorward boundary of diffuse electron aurora coincides with the inner edge of plasma sheet population [*Horwitz et al.*, 1986], whose location reflects the balance between electrons' sunward electric field convection, azimuthal magnetic drift, and loss due to wave scattering [*Fairfield and Vinas*, 1984]. The poleward boundary of auroras characterizes the boundary separating regions threaded by open and closed magnetic field lines in the magnetosphere [*Blanchard et al.*, 1995]. Within the auroral oval, north-south orientated auroras well correlate with high speed magnetotail flow bursts [*Sergeev et al.*, 1999], and east-west arcs at the

equatorward portion of the auroral oval are closely related to enhanced azimuthal pressure gradient in the equatorial plane [*Xing et al.*, 2011].

Aurora located poleward of the auroral oval has also been observed in localized regions and is named as polar cap arcs, polar cap being the region poleward of and encircled by the auroral oval. This region is magnetically connected to the solar wind, and is thus filled with tenuous and low-energy plasma with an energy flux usually too weak to produce optical emissions. Under certain solar wind conditions polar cap arcs emerge, appearing as discrete and sun-aligned arc structures (see Figure 1.2), and can propagate in various directions. At times they may connect to the auroral oval at one or both ends. Similar to arcs within the oval, they are caused by precipitating particles accelerated through a field-aligned potential drop and can be observed in 630.0 and 557.7 nm wavelength [*Zhu et al.*, 1997 and references therein]. Historically, various names have been used to describe these arcs, such as sun-aligned arcs, transpolar arcs, horse-collar aurora, and theta auroras. Recent categorization based on arcs' spatial structure and evolution (oval-aligned, bending, moving, midnight, and multiple arcs) suggests that each arc type occurs for a characteristic combination of upstream solar wind properties [*Kullen et al.*, 2002].

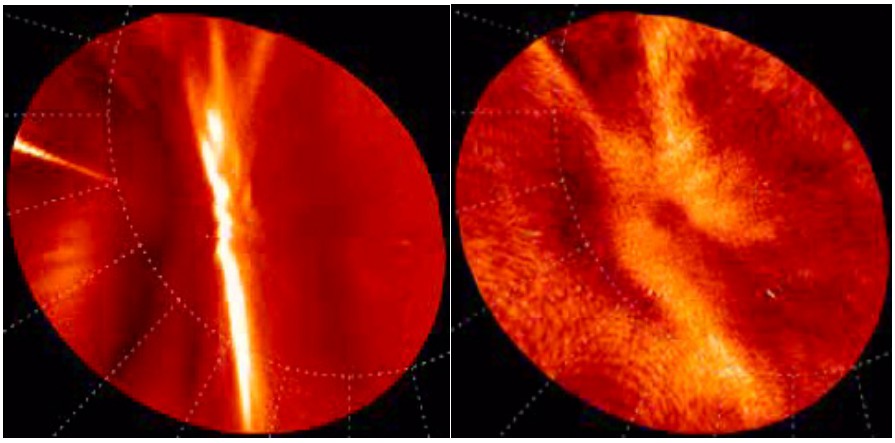

Figure 1.2 Polar cap arc (left) and airglow patch (right) at norther polar cap acquired by OMTI all-sky imager in 630.0 nm. Color indicates 630.0 nm intensity.

However, the driving mechanism of polar cap arcs still remains unclear and seemingly contradictory magnetospheric source regions have been identified based on observations, for example, arcs being mapped through open field lines to the mantle and magnetosheath, or through closed field lines to a bifurcated or expanded plasma sheet, or through closed field lines to the low latitude boundary layer (LLBL) [summarized in *Weiss et al.*, 1993]. Such controversy may arise from the complexity of various auroral phenomena of polar cap arcs and suggests that different auroral manifestations may have different generation processes. The commonly observed and subvisual intensity (hundreds of R) arcs have been shown to be sufficiently excited by field-aligned accelerated polar rain electrons on open field lines [*Carlson and Cowley*, 2005].

Another type of polar cap emission is airglow patches, regions with optically enhanced airglow emissions at 630.0 nm wavelength (Figure 1.2). Different from auroras, the ultimate cause of airglow is attributed to solar EUV radiation. One important process of generating nightside airglow is the recombination of atoms or molecules that have been photo-ionized or dissociated at dayside. Particularly, the 630.0 nm emission is produced by the slow (~ hours) recombination of atomic oxygen [*Cogger et al.,* 1980], and the emission intensity is determined by the magnitude and the altitude of plasma peak density [*Barbier et al.*, 1962]. The enhanced 630.0 nm emission of airglow patches is produced by localized high density of plasma above 200 km altitude (typically 2–10 times larger than the surrounding). This high-density plasma originates from dayside low-latitude sunlit ionosphere, and convects through the dayside cusp into the polar cap (plasma density can be further elevated here due to precipitation [*Rodger et al.*, 1994]), and across the dark polar cap with a timescale of ~2 h [*Oksavik et al.*, 2010]. It may stop and decay within the polar cap [*Hosokawa et al.*, 2001], or can continue to exit the polar cap entering the nightside auroral oval [*Zhang et al.*, 2013] and turn into auroral blobs there [*Crowley et al.*, 2000].

However, physical mechanisms of patch production, transpolar evolution, and exit are still under debate. For example, in order to explain why sunlit plasma enters the polar cap as segmented islands instead of a continuous tongue, several processes have been proposed including: intermittent entry through the large-scale or meso-scale expanding/contracting polar cap boundary [*Anderson et al.*, 1988; *Lockwood and Carlson,* 1992], time-dependent motion following the large-scale convection [*Sojka et al.*, 1993; *Valladares et al.*, 1998] or meso-scale flow channels [*Lockwood and Carlson,* 1992], and segmentation by flow jets through locally increased recombination [*Rodger et al.*, 1994]. Although all these processes would reconfigure high density plasma from the reservoir into patches, *Carlson et al.* [2006] argued that flow channel events are the dominant mechanism.

Both auroras and airglow are important elements affecting space weather as they can substantially disrupt trans-ionospheric radio waves. Discrete auroras are associated with strong shear in the plasma convection velocity in the ionosphere, as expected from the converging electric field surrounding upward field-aligned currents. And such shears produce Kelvin-Helmholtz instability [*Basu et al.*, 1990]. On the other hand, patches of high density plasma, such as airglow patches and auroral blobs, can drive gradient drift instability when their density gradients are orthogonal to the existing ionospheric current, such as Hall or Pedersen current [*Tsunoda*, 1988 and references therein]. Both instabilities cause otherwise relatively uniform plasma to develop electrostatic irregularities in the F region ionosphere, i.e. fluctuations in plasma density and electric field over scale sizes from 0.1 to 10 km [*Basu et al.*, 1988, 1990]. These irregularities can cause substantial radio scintillation, resulting in strong amplitude fading and phase fluctuations within operating frequencies of navigating satellites. They can also scatter radio waves, blind radar tracking, and disrupt or improve high-frequency communication. Although efforts have been made to forecast ionospheric scintillation [*Secan et al.*, 1997; *Wernik et al.*, 2007; *Prikryl et al.*, 2012], their empirical (statistical) approaches

can only characterize the average scintillation probability, and have limited value in realistically predict the structured spatial distribution or transient temporal occurrence.

In fact, despite of the long history of auroral observations, prediction of instantaneous auroral configurations remains challenging. Although the large-scale location and intensity of the electron auroral oval can now be predicted based on real-time upstream solar wind properties [*Newell et al.*, 2002], information on the occurrence of meso-scale (~< 100s km) enhanced auroras is still missing. Such localized intense precipitation signifies regions of strong energy conversion from electromagnetic field to particles, and enhanced transportation from the magnetosphere to the ionosphere, and the occurrence and distribution of these features provide fundamental information on how the magnetosphere gains, transports, and releases mass and energy from the solar wind into the Earth's system.

1.2 Convection in the Magnetosphere and Ionosphere

As solar wind approaches the Earth, the interplanetary magnetic field (IMF) interacts with the terrestrial dipole field and drives convection within the magnetosphere. For the most part of the convection, plasma is strongly coupled with magnetic field lines, where the two are constrained to move together. Southward IMF can connect to the terrestrial field at subsolar point through magnetic reconnection, and create field lines with one end on the Earth and the other end in the solar wind, i.e. open field lines (Figure 1.3). Such field lines are highly kinked and accelerate plasma along the field lines anti-sunward by magnetic tension force, transferring energy from field to plasma. As field lines move across the polar cap, they straighten, bend in the opposite direction due to the continuing anti-sunward flow of their solar wind ends, and stretch out at nightside in the extended lobe region. Here energy is transferred from plasma back to magnetic field and stored inside the magnetotail. Reconnection also exists in the tail, breaking open field lines in the lobe and forming closed field lines (both ends on the Earth) in

the plasma sheet. This process accelerates plasma towards dayside and liberates lobe energy back to plasma.

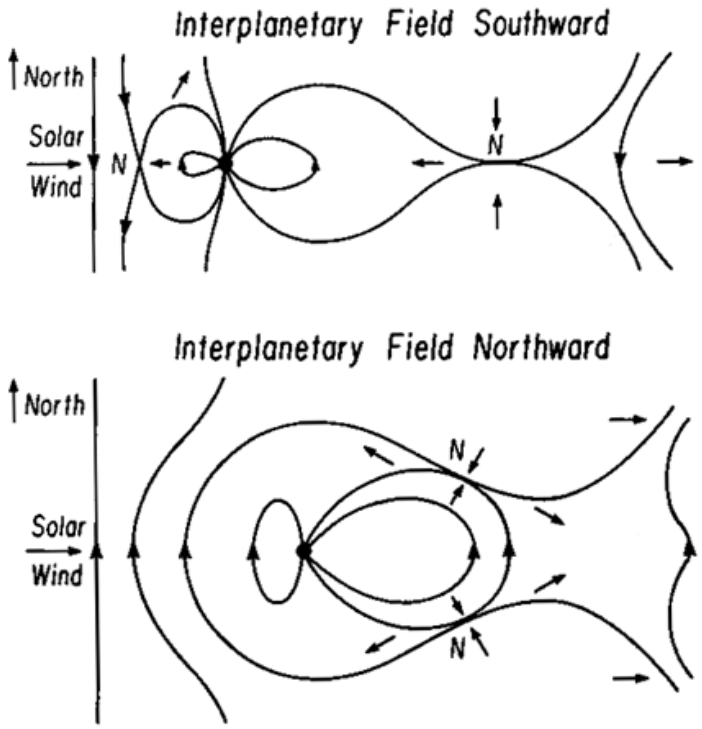

Figure 1.3 Schematic illustration of the magnetospheric convection, for southward, top panel, and northward IMF, bottom panel, Arrows illustrate plasma flow directions. [*Russel,* 1974]

Northward IMF may also result in reconnection, but it migrates to high latitude forming two reconnection sites in the conjugated hemispheres. There they remove flux from nightside and add newly reconnected flux to dayside. The reconnected flux then circulates around the magnetosphere towards nightside and replaces the loss. Compared with southward IMF, here the size of open field line region shrinks and the efficiency of convection decreases. Magnetospheric configuration is also believed to be different but this is still poorly understood.

Assuming magnetic field lines to be equipotentials, magnetospheric convection can be mapped down to the ionosphere. Southward IMF drives ionospheric plasma to convect anti-sunward within the polar cap, and to return sunward within the auroral oval, resulting in a two-cell pattern. The pattern is distorted as IMF deviates from the purely southward direction, for example, becomes asymmetric given an east-west component. This is because after dayside reconnection, convection is azimuthally deflected towards dusk or dawn by magnetic tension, resulting in an enlarged dusk cell for eastward IMF, and an enlarged dawn cell for westward

IMF. Convection becomes more complex and even develops into a four-cell pattern under northward IMF. (Coordinates used in this thesis are in Geocentric Solar Magnetospheric (GSM), where X axis is directed to the Sun, Z axis is the projection of the Earth's magnetic dipole axis on to the plane perpendicular to the X axis and directed towards north, and Y axis is given by the right hand rule directed towards east.)

The real magnetospheric convection is rarely in a steady state, as the rate of reconnection is time- and space- dependent. Reconnection signatures that are easy to measure include fast flow jets accelerated away from the reconnection region and magnetic structures with an enhanced field strength. Oppositely directed jets, as expected to emerge from a single reconnection site, have been continuously observed at the dayside equatorial magnetopause under southward IMF [*Phan et al.*, 2000]. Counter-streaming jets, as expected to occur in-between multiple reconnection sites, can also persist for hours under northward IMF [*Lavraud et al.*, 2006; *Retino et al.*, 2005]. Both results suggest that dayside reconnection can operate continuously without ceasing.

On the other hand, evidence regarding transient reconnection has been identified at the dayside magnetopause as flux transfer events (FTEs). They exhibit a localized enhancement in the magnetic field strength and a bipolar signature in the component normal to the magnetopause [*Russel and Elphic,* 1978], appearing as a magnetic cylinder about 1 *Re* in diameter protruding from and moving along the magnetopause [*Saunders et al.*, 1984]. They contain accelerated plasma as mixtures of magnetosheath and magnetospheric populations with densities intermediate between the two regions [*Paschmann et al.*, 1982]. Such structures may result from patchy reconnection [*Russel and Elphic,* 1978], single [e.g. *Scholer et al.*, 1988] or multiple [*Lee and Fu*, 1986] X-line reconnection, or vorticity-induced reconnection from Kelvin-Helmholtz waves [*Liu and Fu,* 1988]. And the corresponding shapes of FTEs would be an elbow-shaped flux tube, a temporal magnetic bulge, a plasmoid/flux-rope, and a magnetic

tube collocated with velocity vortex. FTEs tend to occur under southward IMF in an episodic manner. Whether this is due to their intrinsic intermittent nature or is driven by fluctuations in IMF or other solar wind factors [*Lockwood and While*, 1993; *Le et al.*, 1993; *Kuo et al.*, 1995] is unclear.

Nightside reconnection is often highly sporadic and localized, and is regarded as an independent process from dayside reconnection because the two are frequently unbalanced. Observations within the plasma sheet frequently detect flow bursts that are embedded in slow background convection and rise and fall in a timescale of the order of one minute [*Angelopoulos et al.*, 1992]. These flow bursts tend to occur sequentially for ~10-min intervals, i.e. bursty bulk flow events (BBFs), and appear as azimuthally confined channels of a few *Re* wide. BBFs can propagate both earthward and tailward, depending their locations relative to the reconnection region [*Angelopoulos et al.*, 1994]. In fact, nightside reconnection sites vary over a wide range of distances under different geomagnetic activity [*Nishimura et al.*, 2013], and both the near-Earth (~20–30R_E, *Nagai et al.*, 1998) and distant reconnection sites (60–120 R_E, *Zwickl et al.*, 1984) produce fast flow jets. Earthward propagating BBFs provide a dominant (70-80%) contribution to the total plasma sheet transportation, and upon arriving in the near Earth region (< 20 Re), they can be deflected [*Panov et al.*, 2010a] and even rebounded [*Panov et al.*, 2010b] due to the rapid increase in the repelling pressure gradient force from tail to dipolar field. During their transportation they bring energetic particles towards the Earth, depolarize magnetic field in the plasma sheet, and reconfigure equatorial pressure distribution both radially and azimuthally, substantially impacting the near Earth environment.

Patchy tail reconnections also produce localized magnetic structures within the plasma sheet identified as nightside flux transfer events (NFTEs) and plasmoids/flux ropes. Both are mesoscale (a few Re) bulge-like features propagating with BBFs, and exhibit a bipolar variation in the *Bz* and a compression in the *Bx* component. However, plasmoids or flux ropes

consist of closed loop-like or helical field lines, and demonstrate an almost symmetric bipolar *Bz* perturbation. They are formed by simultaneous reconnection at multiple X-lines distributed along a factional length of the plasma sheet. NFTEs are produced by impulsive single X-line reconnection and predominately carry magnetic flux of a single polarity, exhibiting asymmetric *Bz* variation. Nevertheless, both evolve into localized and transient dipolarization fronts (sharp increase of *Bz*) through flux pile-up as they are transported from the reconnection site towards the Earth [*Hesse and Birn,* 1991].

Recent simulations have suggested that dipolarization fronts, and associated flow jets, can form spontaneously under strong accumulation of magnetic flux in the tail and later trigger magnetic reconnection to occur in their wake [*Sitnov et al.*, 2013], indicating a reversed causality and temporal sequence between the two phenomena from the discussion above. This indicates that reconnection is a secondary disturbance of the dipolarization onset, and that the recognized impacts and characteristics of reconnection actually reflect those of this onset. Since whether or how commonly this process occurs in the magnetosphere is unknown, for now we still regard reconnection as the primary source causing the localized magnetic and flow features. Our discussion can still be applied to dipolarization onsets with modification.

Direct encounters of reconnection have also been identified, but remain rare. For example, within the nightside reconnection region, the current sheet that separates the oppositely-directed lobe magnetic fields is found to have two pairs of bifurcated currents and a flat and thin current in between [*Runov et al.*, 2003]. Magnetic field there is also observed to exhibit a quadrupolar configuration out of the reconnection plane, which is likely to be produced by microscopic physics of reconnection [*Øieroset et al.*, 2001; *Nagai et al.*, 2001]

Magnetic reconnection can directly dump plasma into the atmosphere producing a bright auroral spot almost instantaneously [*Phan et al.*, 2003]. In addition, the inhomogeneous magnetospheric convection can generate transient and localized ionospheric flow bursts and

discrete auroras within minutes. The delay results from the dynamic coupling between the magnetosphere and the ionosphere under time-varying conditions. A temporal change in the magnetospheric convection is communicated through shear Alfvén waves along the field lines into the conducting ionosphere, where waves get partially reflected and bounce between the origin of disturbance and the northern and southern hemispheres. A few Alfvén transit time (minutes) is thus required to accelerate the ionospheric plasma to the velocity corresponding to an approximate steady state, and possibly to establish the auroral parallel electric fields to maintain the field aligned currents emerging from the shear of magnetospheric convection [*Hull et al.*, 2010].

Dayside ionospheric flow bursts of up to 1 km/s are observed to occur near the poleward boundary of the auroral oval at FTE foot-points, and their velocity peaks with a few minute delay relative to each FTE [*Ephic et al.*, 1990; *Neudegg et al.*, 1999]. They last 10-15 minutes within the observing area and repetitively occur at a rate consistent with FTE periodicity [*McWilliams et al.*, 2000]. They extend a few hundred km in the east-west direction and direct first azimuthally and then poleward, as a response to magnetic tension and anti-sunward solar wind flow. These flow bursts are often accompanied with auroral structures propagating from the auroral oval to high latitude, i.e. poleward moving auroral forms (PMAFs). They can also transport large volumes of sunlit plasma that are captured within them into the polar cap forming airglow patches [*Carlson et al*., 2004].

Nightside ionospheric counterparts of BBFs have been identified as narrow channels of flow bursts and auroral streamers lying westward of them. Streamers originate from brightenings at the poleward portion of the auroral oval, i.e. poleward boundary intensifications (PBIs), and then extend equatorward as north-south oriented or tilted auroral arcs. They are produced by field-aligned currents of narrow BBFs (3-4 *Re* wide) at distant or mid-tail (Figure 1.4). Other auroral activity at the equatorward portion of the auroral oval, such as localized

intensifications (pseudo-breakups), can also be produced by BBFs and such BBFs are usually wide and have intruded close to the Earth (4-5 *Re* wide and 13 *Re* down tail) [*Nakamura et al.*, 2001]. The field-aligned currents of BBFs, and their ionospheric closure, also perturb ground magnetic field in the auroral zone and produce an equatorward propagating disturbance in magnetometer data. At times, magnetic field at low latitude also exhibit oscillations and these are excited by the deceleration of BBFs [*Cao et al., 2008*].

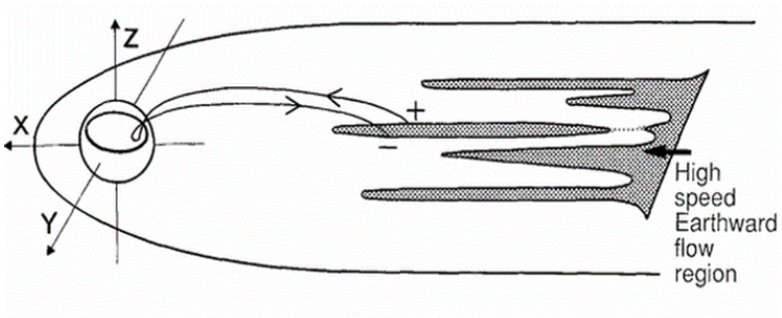

Figure 1.4 Schematic illustration of the relation between auroral streamers and BBFs. Precipitation of electrons accelerated in the BBF's upward field-aligned current forms the auroral streamer [*Sergeev et al.*, 2000].

Therefore, ionospheric convection reflects activity in the vast magnetosphere, and ionospheric measurements can provide a powerful monitoring of magnetospheric dynamics in multiple scales, over extended intervals, and across broad area. For example, nightside auroral observation can present an instantaneous map of plasma sheet reconnection/BBF distribution, as well as a time series of their evolution and impact at other regions. Such observations can hardly be accomplished by using the few point observations of spacecraft alone. Even given multiple satellites that are spaced out over long distances, one still needs to examine the simultaneous ionospheric observation to confirm that the observed features belong to the same or relevant processes, instead of being coincidental.

One outstanding question regarding magnetospheric convection is when and where magnetotail reconnection occurs, spontaneously or driven by external forcing. Reconnection occurs when the scale length of the magnetic field gradient becomes less than the electron and

ion inertial length scales. The sharp gradient results in an intense current sheet, where the sheared magnetic field and the plasma can diffuse and mix if resistivity or Hall effect is present. The former is provided by electron-ion collisions or by turbulence generated by instabilities (anomalous resistivity), and the latter by a separation of ions and electrons as ions become unmagnetized while electrons are still magnetized. However, both mechanisms should develop locally and sporadically in the space environment as suggested by observations, and the underlying reason is poorly understood. Therefore information on the necessary or favorable conditions for magnetic reconnection to take place is essential for understanding this physical process. Moreover, considering the contribution of reconnection to convection, this information will also promote our ability to forecast following dynamical evolution of the entire magnetosphere and ionosphere, which is one important goal of studying space weather.

In situ observations of magnetotail reconnection and its preceding conditions rely on the rare chance when the satellites are located at the right place and at the right time. Simulation of reconnections in the global magnetosphere is based on parameterization where resistivity is empirically switched on given certain threshold for the curl of magnetic field [*Raedar et al.*, 2001]. On the other hand, the ground-based observations, including optics and radars, can remotely monitor the occurrence of reconnection and its resultant enhanced convections over large area and long interval. Although they are not capable of determining the microscopic magnetic field configuration and particle distribution at the reconnection site, such observations provide important measurements of the preceding and surrounding conditions for reconnection to develop at meso- and macro- scales (tens to thousands km in the ionosphere). The investigation also echoes the challenge of auroral observation in Section 1.1, i.e. understanding when and where localized brightenings would occur.

This thesis is dedicated to understand the distribution of nightside large-scale auroras and the favorable conditions of the embedded meso-scales aurora to occur with emphasis on the

latter. The results suggest that locally enhanced nightside auroras are consistently preceded by, and developed around, fast flow bursts arriving at the poleward boundary of the auroral oval from the polar cap, and perhaps even from dayside. This indicates nightside reconnection to be externally triggered and to develop upon the intrusion of upstream flow bursts. This also traces the origin of nightside geomagnetic disturbances to regions that are traditionally believed to be quiescent or to have no direct relation to nightside reconnection, implying the existence of a meso-scale convection system that is regulating dynamic perturbations of the magnetosphere.

Chapter 2. Literature Review

2.1 Large-scale Distribution of Nightside Auroral Oval

Information on the large-scale distribution of the auroral oval is important for probing magnetospheric field configuration and plasma distributions. The 2-D location of the equatorward boundaries of electron and proton auroras, and its dependence on geomagnetic activity, have been extensively examined through various approaches. In situ measurements of low-altitude precipitating particles above the auroral zone have been assembled to derive a statistical auroral distribution [*Gussenhoven et al.*, 1981; *Hardy et al.*, 2008; *Hardy et al.*, 1989, 1991]. They show that the proton and the electron boundaries both move systematically to lower latitudes with increasing magnetic activity. And protons always extend equatorward of electrons on the duskside and poleward on the dawnside [*Gussenhoven et al.* 1987].

Spacecraft-based optical observations in multiple wavelengths can obtain not only statistical but also instantaneous global auroral images. Although electron auroral imaging has been obtained by early missions, such as Dynamics Explorer and Polar [*Frank and Craven*, 1988; *Liou et al.*, 2001], proton detection was not achieved until the IMAGE satellite [*Frey et al.*, 2001]. Superposed analysis of IMAGE observation reveals a similar distribution of auroral pattern as *Gussenhoven et al.* [1987] [*Mende et al.,* 2003; *Milan et al.,* 2009]. *Milan et al.* [2009] further showed that the proton duskside oval is located consistently equatorward of the dawnside oval, while the dawn and dusk locations of the electron oval are similar, indicating the proton oval to be more asymmetric than the electron's.

Ground-based optics presents a consistent auroral morphology in the premidnight sector with earlier studies [*Wiens and Vallance Jones*, 1969; *Fukunishi*, 1975; *Creutzberg et al.*, 1988; *Ono et al.*, 1987, 1989]. In the postmidnight sector, however, the relation of the electron

and the proton auroras is less definite, varying from overlap [*Fukunishi*, 1975] to electrons extending equatorward of protons [*Wiens and Vallance Jones*, 1969; *Fukunishi*, 1975; *Creutzberg et al.*, 1988]. *Fukunishi* [1975] suggested that this relative distribution can change with geomagnetic activity, i.e., the electron aurora is superposed on the proton aurora during quiet time, and extending equatorward of it during substorm expansion phase.

In terms of displaying a 2-D spatiotemporal evolution of the magnetosphere, all the above instruments are still limited. In situ particle measurements can only detect precipitation at a particular longitude upon each auroral-zone crossing, and are thus limited in providing an instantaneous auroral pattern. Optical observations, on the other hand, have not yielded a reliable equatorward boundary of the electron auroras, as the utilized emissions (ultraviolet including FUV and 557.7 nm) are not sensitive to low-energy electron ($\lesssim$1 keV) precipitation, which extends more equatorward than the higher energy precipitation. This can be improved through utilizing ground-based 630.0 nm observations.

Here we use optical observations from the NORSTAR meridian scanning photometer (MSP) array (including data from the period predating NORSTAR when these instruments were the CANOPUS MSP network) to reconstruct the spatial distributions of the equatorward boundaries of the electron and the proton auroras under different steady magnetospheric conditions. Although the employed instrument only scans over a narrow meridian, our results can be applied to all 630.0 nm all-sky imagers (ASIs), which have been deployed across the North America and operate simultaneously covering a region ~4-5 h wide in magnetic local time (MLT). We also compare the boundaries derived from MSP with those from white light ASIs, the agreement suggests that we can further widen our detecting region into white light field of views (FOVs), which can monitor auroral activity over a ~10 h MLT region.

The location of the poleward auroral boundary has also been widely explored and reasonable agreement has been obtained between in-situ electron measurements and optical

electron observation from both ground [*Blanchard et al*., 1997] and satellite imaging [*Kauristie et al*., 1999; *Baker et al*., 2000; *Carbary et al*., 2003; *Milan et al*., 2003; *Boakes et al*., 2008]. This boundary symmetrically expands equatorward and contracts poleward under different geomagnetic activity [*Mende et al.,* 2003; *Milan et al.,* 2009]. The in situ proton precipitation usually extends to higher latitude than that in imagers, where the flux becomes too weak to be resolved by optics [*Mende et al.*, 2003].

While these poleward precipitation boundaries presumably mark the open-closed field line separatrix, it is noteworthy that the two are not strictly equivalent. Instead, the former can at times be located ~ 1° equatorward of the later [*Wing and Zhang,* 2015]. This is partially because as electrons stream from the magnetotail towards the Earth, they undergo electric field convection, which at outer plasma sheet has an equatorward-directed component and brings the electrons to lower latitude than they initially are. Because of the long distance from the source region to the Earth, such effect becomes pounced for precipitation at high latitude.

2.2 Meso-scale Auroral Enhancements: Poleward Boundary Intensifications (PBIs)

PBIs are discrete auroral intensifications that occur along the poleward boundary of the nightside auroral oval and may extend equatorward as streamers. They are generally believed to be related to localized enhanced magnetotail reconnection. PBIs are the type of meso-scale auroral signature that is examined in this thesis.

PBIs occur repetitively during all levels of geomagnetic activity and their activation is one of the most intense meso-scale auroral disturbance [*Lyons et al*., 1998]. Two-dimensional optical observations show that PBIs can appear as north-south, tilted, east-west structures,

beads/swirls, and patches [*Zesta et al*., 2002] (Figure 2.1). Small-scale ray structures associated with Alfvén wave activity have also been detected [*Lynch et al*., 2012]. PBI precipitation is observed to be driven by electrostatic or Alfvénic acceleration, or both at the same time [*Hull et al.*, 2010; *Mella et al.*, 2011]. In fact, the electrostatic field is shown to develop out of the Alfvénic waves [*Hull et al.*, 2010].

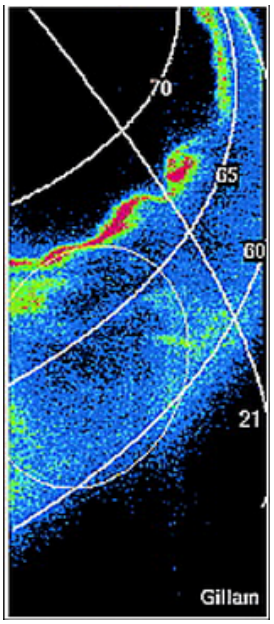

Figure 2.1. PBIs observed in satellite imaging [*Zesta et al.,* 2002]

PBIs and their streamers, have been shown to be one-to-one associated with earthward propagating BBFs and dipolarization fronts in the magnetotail [*Lyons et al*., 1999; *Zesta et al*., 2000; *Nakamura et al*., 2001], indicating that PBI occurrence well corresponds to magnetotail reconnection. Based on the average magnetic field configuration, PBIs correspond to narrow and extended (a few *Re* in width and >~10 *Re* in length) BBFs that are located at a distance of 30 *Re* or further away from the Earth [*Zesta et al.*, 2006]. Recently, PBIs are also found important for producing near-Earth disturbances by triggering the formation of substorms [*Nishimura et al*., 2010a; *Zou et al*., 2010; *Mende et al*., 2011]. They showed that PBIs lead to streamers that propagate toward the substorm onset meridian, and then induce the substorm.

PBIs' association with magnetic reconnection, origin of other auroral forms, and preceding occurrence of near-Earth disturbances motivate us to conduct a study to understand how PBIs are triggered. As reviewed below, coordinated observations of radars and imagers are particularly useful for investigating the surrounding and preceding convection around PBIs, and we employ such measurements in our study.

2.3 1-D Relation between PBIs and Localized Polar Cap Flow Enhancements

Until now the fundamental question of how PBIs are generated remains unsolved. PBIs have been found to be associated with equatorward directed ionospheric flow channels across the poleward boundary of the auroral oval from the polar cap [*de la Beaujardière et al*., 1994; *Shi et al*., 2012]. However, whether these flows form locally or propagate from somewhere else remains unknown until the recent the detection by *Nishimura et al*. [2010b, 2014], *Lyons et al*. [2011], and *Pitkänen et al*., [2013]. Using 1-D radar measurements, they show that contrary to the tradition assumption, polar cap convection is not uniform but has narrow channels (~0.2 h MLT) of fast flows propagating equatorward (as marked in Figure 2.2). As these flows approach the nightside auroral poleward boundary, PBIs develop nearby

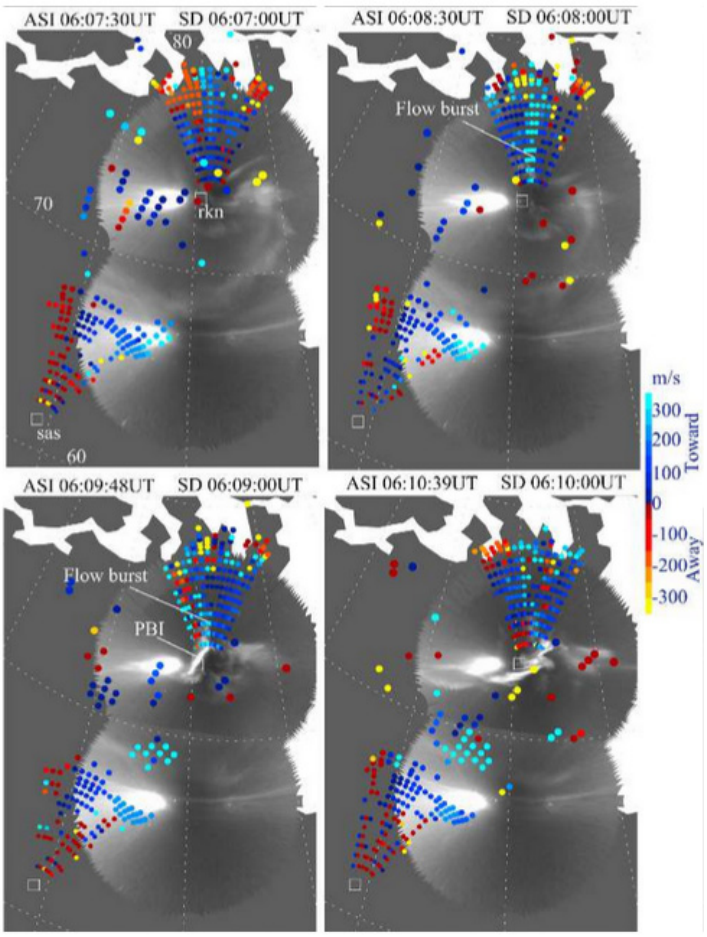

Figure 2.2 Snapshots of ASI observation (grey scale) overlaid with line-of-sight measurements (color-coded as the color bar) by radars near the magnetic midnight. Location of radar stations are marked as rkn and sas. The flow burst occurred in the central meridian and clearly show a longitudinally and enhanced equatorward flow in the polar cap extending down to the auroral poleward boundary (~73°). The PBI occurred ~1 min later at the same longitude as the flow. [*Nishimura et al*., 2010b]

within a few minutes (as marked in Figure 2.2). These studies highlight the existence and significance of locally enhanced convection within the polar cap, and suggest an unexpected but promising connection between these flows and PBIs.

The ionospheric observation indicates that fast flow jets exist in the open field line/lobe region and propagate towards low latitude. They can then traverse the open-closed field line separatrix, likely through an occurrence of localized magnetic reconnection (or locally developed dipolarization onset in the *Sitnov et al.* [2013] scheme). Reconnection generates plasma sheet flow channels whose duskside edges mark upward field-aligned currents, illuminated as PBIs in the ionosphere. In fact, these elements have been identified by in-situ satellites in association with PBIs in separate studies. *Lyons et al*. [2010] used satellites at the plasma sheet boundary layer and observed enhanced perpendicular flows moving across the separatrix towards the central plasma sheet. Signatures of reconnection have been identified by *Hull et al*. [2010] as an injection of new plasma population into closed field line region, which results in a local thickening of plasma sheet. Plasma sheet dipolarizations are detected by *Pitkänen et al*. [2013] after a localized polar cap fast flow reaches the auroral poleward boundary in association with a PBI development.

However, the above event studies cannot address whether the relationship between PBIs and meso-scale polar cap flow enhancements occurs commonly. The answer is important because if it is common, these flows then play an essential role in the development of localized magnetotail reconnection and the associated BBFs in the plasma sheet, and thus further contribute to substorm disturbances.

We determine the commonality of this association by using coordinated observation of a radar and an ASI. While the data set is similar to those used in previous studies [e.g., *de la Beaujardière et al*., 1994; *Shi et al*., 2012], the high sensitivity of ASIs makes possible detection of localized PBIs that cannot be resolved by global imaging, and the short-range radar

echoes overlapping with the ASI FOV can detect localized flows that could be missed in long-range echoes. We start with isolated and intense PBIs and study the probability of PBIs being associated with enhanced polar cap flows extending toward the auroral poleward boundary. For the correlating flows and PBIs, we further investigate the time lag of PBI initiations relative to flows, and compare their durations and longitudinal widths. We also perform a reverse study by starting with isolated polar cap flows to examine whether they are associated with PBI activation. By comparing the commonalities of flow-PBI association starting from PBIs and starting from flows, we will be able to tell whether flows and PBIs occur in pairs or whether the occurrence of one is more than the other, the former indicating a one-to-one correspondence.

Although optical identification of the auroral poleward boundary has been well examined in multiple wavelengths [*Blanchard et al*., 1997; *Kauristie et al*., 1999; *Baker et al*., 2000; *Carbary et al*., 2003; *Milan et al*., 2003; *Boakes et al*., 2008], the reliability of using white light has not been investigated. Since we use white light to identify PBIs, it is essential to test whether the identified PBIs truly reflect the most-poleward auroral electron precipitation near the precipitation boundary. This is performed by comparing white light ASI with in-situ particle measurement in two events.

2.4 2-D Tracing of Localized Polar Cap Flow Enhancements

The close connection between localized polar cap flow enhancements and PBI disturbances emphases the significance of these flow features and calls for comprehensive studies on their structure and evolution. Although radars directly measure ionospheric flows, backscatter echo regions are generally limited, particularly in the broad polar cap, and mostly give only 1-D line of sight (LOS) measurements. Thus by using radar measurements alone, it is difficult to trace flows over long distances and in 2-D, which might be the reason why such flow features were not widely identified in the past.

Here we examine the feasibility of flow tracing using ASIs, which cover a much wider area and monitor emissions in 2-D. Two common types of polar cap emissions are airglow patches and polar cap arcs. Except for some theta aurora, polar cap arcs are known to be associated with localized and enhanced anti-sunward sheared flows embedded in the large-scale convection [e.g. *Robinson et al.*, 1987; *Valladares and Carlson*, 1991; *Koustov et al.*, 2008], as expected of the converging electric field surrounding upward field-aligned currents. However, polar cap arcs mostly occur under northward IMF, when PBI and overall auroral activity is quiet. Airglow patches, on the other hand, are mostly formed under southward IMF, and thus their association with localized flows will lay important groundwork for studying polar cap flow-PBI association.

Airglow patches are shown to follow local ionospheric convection [*Weber et al.*, 1986]. This indicates that patch motion can potentially be modulated by, and thus reflect, localized polar cap flow enhancements. If this is generally true, airglow patches could then be used to visualize the spatial extent and 2-D motion of meso-scale flows, just as polar cap arcs, over their long travel within the polar cap.

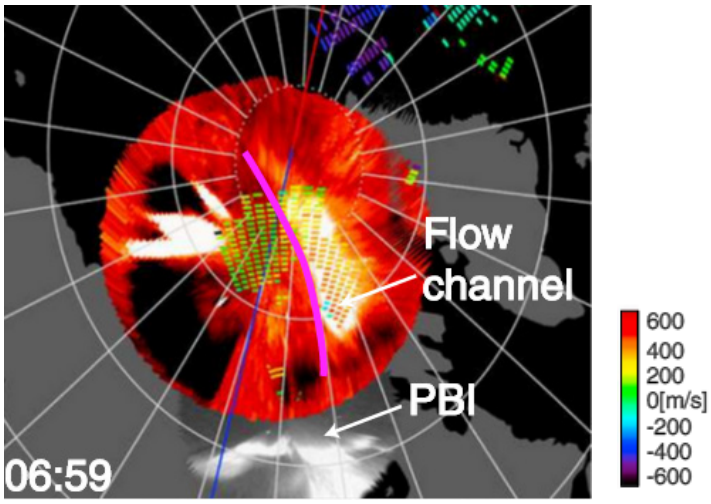

Figure 2.3 Snapshot of a 630.0 nm (red) and white light ASI (grey), overlaid with radar data. The red and blue lines mark the magnetic noon and midnight meridians. The bright elongated structure in 630.0 nm is an airglow patch, and its duskward edge is marked by the pink curve. This patch is collocated with a narrow channel of fast flow [*Nishimura et al.*, 2014]

Evidence shows that as airglow patches drift equatorward from the polar cap across the nightside poleward boundary, they are directly connected to PBIs and streamers [*Lorentzen et al.*, 2004; *Moen et al.*, 2007; *Nishimura et al.*, 2013], consistent with the polar cap flow-PBI

association. This leads to a hypothesis that airglow patches may be the optical representation of the radar measured polar cap flows. In fact, *Nishimura et al.* [2014] (Figure 2.3) detected a patch that was propagating equatorward with a collocated localized flow enhancement, suggesting the two to be potentially related.

While research on localized flow enhancements deep in the polar cap is very limited, narrow and transient flow enhancements near the dayside auroral poleward boundary have been widely identified as signatures of FTEs. As discussed in Section 1.1., FTEs are one important process, and likely to be the dominant process, of forming and transporting airglow patches into the polar cap. The fate of FTEs in the magnetotail is poorly understood and they have been postulated to sink into the magnetospheric lobe [*Sibeck and Siscoe*, 1984], or become connected to the ionosphere or open to the solar wind at both ends [*Lee and Fu*, 1985]. Recent observation identified multiple FTE encounters at distant magnetopause (67 *Re* downtail) and these FTEs seem to be produced at and transported all the way from dayside [*Eastwood et al.*, 2012]. If this is true, the corresponding ionospheric flow enhancements can continue to propagate anti-sunward over long distance from dayside carrying patches along, evolve into the localized flow features observed at the nightside polar cap, and then continue to traverse the poleward boundary of nightside auroral oval resulting in disturbances there. However, the generalization of this sequence requires flow tracing over wide areas.

We explore the association between localized polar cap flow enhancements and airglow patches at nightside polar cap and their statistical properties using coordinated observations of radars and a polar cap ASI. We find that the two are well collocated over a broad area in case studies and that this collocation is common in statistics, suggesting patches to be good optical tracers of these flow features over long distance and in 2-D. Based on the patch-flow associations, we determine the flow properties (velocity, duration, and width), their IMF dependence, and their contribution to polar cap convection.

2.5 2-D Flow Impact on Nightside Auroral Oval

Previous observations suggest that meso-scale flows in the polar cap can traverse the nightside auroral poleward boundary and relate to PBI activity through enhanced magnetotail reconnection. However, due to the imitated radar echo coverage and mostly 1-D LOS measurements, most of the previous flow observations have been limited to regions only a few degrees in latitude near the auroral poleward boundary, providing no direct information on the flow source and prior evolution. Even within the observing area, without continuous 2-D flow vector information, when and where these flows impinge on the separatrix in relation to auroral oval disturbances remains ambiguous. Such ambiguity limits our ability to evaluate the reported coupling between the polar cap and auroral oval activity, and thus calls for a better approach than radar measurements alone to investigate this association over large area and in 2-D.

The optically faint and diffuse nature of airglow patches does not allow for accurate determination of the flow impingement on the nightside auroral oval, particularly with the sensitivity of the currently available ASIs. Thus here we use polar cap arcs, which are in general much brighter and more discrete than patches and can thus highlight when and where flows contact the nightside auroral oval with high accuracy.

Optical observations from spacecraft have shown evidence that polar cap arcs can spatially connect to intensifications within the nightside auroral oval, indicating a close relation between polar cap and plasma sheet processes [*Murphree et al*., 1987; *Pellinen et al.*, 1990; *Henderson et al.*, 1996] (Figure 2.4). However, satellite imaging is limited to low sensitivity and resolution. Such connections have also been identified in ground-based 630.0 nm ASI observations for a few cases by *Nishimura et al.* [2013]. Although the ASI has high sensitivity, because only a single ASI is employed, spatial coverage is limited. These limitations of earlier studies have left many questions unsolved, particularly, how commonly do polar cap features

impact auroral oval activity and how strong is the response, and when and where does the response initiate. Now these questions can be resolved by utilizing an array of high resolution multispectral ASIs that was deployed in 2008.

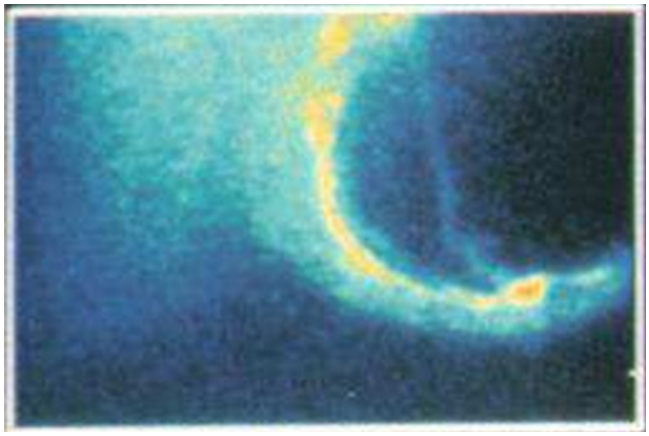

Figure 2.4 A connection of a polar cap arc to an intensification in the auroral oval. Dayside is toward the top left and the diffuse emission there is sunlight contamination. The region encircled by the ring-like auroral oval is the polar cap and the narrow and faint structure in it is polar cap arc. Its nightside end is connected to an intensification in the nightside auroral oval [*Murphree et al.*, 1987]

Polar cap arcs preferentially occur during northward IMF, while how they are formed remains ambiguous. Simulations have suggested arcs to be formed when IMF suddenly changes its orientation from northward. This change can lead to a relocation of dayside reconnection, creating a new open magnetic field line region separated from the original one. The closed field lines in between then drifts poleward producing arcs in the polar cap [*Chang et al.*, 1998]. The change can also introduce a rotation of the near-Earth plasma sheet relative to the far-tail one, and thus produces a displacement between precipitation from the two regions (main oval produced by near-Earth plasma sheet and polar cap arc by that far-tail plasma sheet) [*Kullen et al.*, 2004]. Alternately, it may create loops of magnetic field lines, which become disconnected from the Earth but capable of perturbing the shape of far-tail open-closed field line boundary, resulting in brief protrusion of closed field line precipitation into the polar cap [*Maynard et al.*, 2003]. However, these results only apply to intense and steady transpolar arcs [*Chang et al.*, 1998; *Kullen et al.*, 2004], or very short-lived arcs [*Maynard et al.*, 2003]. The most common polar cap arcs are likely to be produced by accelerated polar rain electrons along the open field lines [*Carlson and Cowley*, 2005]. The acceleration can be driven by flow shears in the lobe, as possibly produced by the time- and space- varying reconnections.

Note that not all meso-scale polar cap flow enhancements are related to polar cap emissions, and it is likely that not all disturbances in the auroral oval are related to these flows. Thus we do not intend to attribute all oval disturbances to polar cap arcs. Instead we focus on events where the arcs and associated flows can be traced continuously to the nightside auroral poleward boundary, so as to definitively evaluate any influence from the polar cap on auroral oval dynamics. We use arc motion towards the auroral boundary, and not intensity variations, since no consistent fading and brightening of polar cap arcs have been found relative to oval intensifications in superposed epoch analysis [*Weygand et al.*, 2001]. Although our database is biased to northward IMF and quiet geomagnetic conditions, we can specify how commonly polar cap flows precede nightside auroral intensifications over long distance and in 2-D during such conditions.

Here by combining radars with an array of 630.0 nm imagers, we characterize three types of nightside oval intensifications that we find in response to approaching polar cap arcs. We present case studies and a statistical study based on over 6 years of data to discuss the commonality of the occurrence of these oval disturbances, the time and location of their initiation, and their spatial sizes. The IMF and geomagnetic conditions of our events are also presented.

Chapter 3. Objectives and Instruments

3.1 Objectives

In order to understand the distribution of nightside large-scale auroras and the favorable conditions of the embedded meso-scale auroras to occur, we divide our project into the following four steps:

(1) **Determine the evolution of large-scale auroral oval**:

Examine the absolute and relative locations of the equatorward boundaries of the proton and the electron auroras, and their dependence on geomagnetic activity.

(2) **Investigate whether the occurrence of PBIs is commonly associated with localized polar cap flow enhancements just poleward of them in 1-D**:

Examine given isolated PBIs, whether fast flows appear in the polar cap near the same time and the same longitude, and vice versa. Compare the initiation time, duration, and longitudinal width of PBIs with those of flows.

(3) **Investigate feasibility of optical tracing of localized polar cap flow enhancements in 2-D and over long distance and determine basic flow properties:**

Evaluate the relationship between flows and airglow patches in their spatial extents, locations, and propagations, and statistically determine flow speed, duration and width.

(4) **Examine how and how often localized polar cap flow enhancements impact nightside auroral oval activity over long distance and in 2-D:**

Trace flows from high latitude to the poleward boundary of nightside auroral oval using polar cap arcs and examine their commonality of being followed by oval disturbances occurring in the vicinity. Determine when and where these intensifications initiate relative to the arcs.

3.2 Optical Instruments

3.2.1 Meridian Scanning Photometer (MSP)

MSP scans the sky from north to south along the magnetic meridian and detects emission intensity as a function of elevation angle. Observations from NORSTAR at Gillam (56.37°N, 265.40°E geographic) and Pinawa (50.15°N 264.12°E) stations are adopted. The two stations are on the same magnetic meridian (the so-called "Churchill Line"), and are located at favorable latitudes to detect the equatorward auroral boundaries under almost all geomagnetic conditions. Proton auroras are identified using 486.0 nm (Hβ) emissions, and are projected onto an altitude of 110 km, while electron auroras are identified using 630.0 nm, and are projected onto 230 km. Although these emissions generally come from a range of altitudes, such projection works reasonably well with small uncertainties (detailedly discussed in Section 4.2). In high-resolution mode, the MSPs scan along the magnetic meridian twice per minute.

3.2.2 Polar-Cap Multi-spectral All-Sky Imager (ASI)

ASI uses wide-angle lens (fisheye lens) to detect auroral emissions above the horizon in 2-D. The one at Resolute Bay (RESU, 74.7°N, 94.9°W geographic) is one of the Optical Mesosphere Thermosphere Imagers (OMTI) and measures polar cap emissions in multiple wavelengths [*Shiokawa et al.*, 1999, 2009]. Measurements at 630.0 nm wavelength are primarily used for studying airglow patches and polar cap arcs, and are obtained every 2 min with an exposure time of 30 s. They are projected onto an altitude of 250 km and because of this high altitude, the FOV covers a broad area of the polar cap up to the magnetic pole and allows for emission tracing over long distances. Due to the generally faint emissions, a running median intensity in the polar cap of 2 h is subtracted to enhance emission contrast to the background. Data at 557.7 nm wavelength are also used to distinguish between polar cap arcs

and airglow patches, which occur with and without substantial 557.7 nm emissions, respectively [*McEwen*, 1998]

3.2.3 Multi-spectral ASI Array

The utilized multi-spectral ASI array comes from Narrow-band All-Sky Camera for Auroral Monitoring (NASCAM) [*Donovan et al.*, 2003]. The most poleward located ASI at Resolute Bay (RESU, 74.7° N, 94.9° W geographic, collocated with OMTI RESU) detects emissions deep in the polar cap, and the rest ASIs (for example, TALO, RANK, GILL, and FSMI) mainly monitor emissions in the auroral oval. The combined FOVs cover a large area over ~20-30° in latitude and ~4 h in MLT, and thus enable detection of any optical association between the polar cap and the auroral oval regions. These ASIs measure multiple auroral emissions including 630.0 and 557.0 nm every 15 or 30 s, depending the time of operation. Although their sensitivity at 630.0 nm is somewhat low for tracing airglow patches, they can well capture faint emissions from low energy (~< 1 keV) precipitation, such as polar cap arcs, and those in the auroral oval. For easy visualization, faint emissions are enhanced by subtracting a running median as OMTI ASI.

3.2.4 White Light ASI Array

The white light ASI array is part of the THEMIS mission and consists of 21 ASIs that were deployed in the North American continent to broadly monitor nightside auroral activity [*Mende et al.*, 2008]. It has stations collocated with all the above optical instruments except at RESU, and thus allows for comparing auroral behavior at different wavelengths and complementing auroral observation when multi-spectral data are unavailable. The white light intensity is mainly contributed by the intensest 557.7 nm emission, and thus mostly provides

information of high-energy (> 1 keV) electron precipitation. It is projected onto 110 km height. Projection on 230 km has also been performed (Section 4.2), just as 630.0 nm emissions in NORSTAR, and shows that the low-energy precipitation could still be possibly identified at the equatorward border of high-energy precipitation.

3.3 Radars

Radars utilize the Doppler effect to measure the LOS velocity about plasma irregularities in the ionosphere. The utilized two radars are the most poleward located stations of Super Dual Auroral Radar Network (SuperDARN) in the northern hemisphere at Rankin Inlet (RKN, 62.8°N, 93.1°W geographic) and Inuvik (INV, 68.4°N, 133.5°W; both looking poleward) [*Chisham et al*., 2007]. They operate at frequencies between 8 and 20 MHz and electronically steer across 16 beam directions every 1–2 min. The backscattered echoes along each direction are binned into 45-km long range gates to obtain a LOS (mostly north-south oriented) flow speed within each range. Both radars have FOVs starting from a region just poleward of the most probable latitudes of the auroral poleward boundary and extending up to the magnetic pole, and thus allow for studying polar cap flow evolution and impact on the auroral oval. Within the common FOV, they also give 2-D merged flow vectors. They occasionally operate at high temporal resolution (8 s) along a particular beam.

3.4 Low Altitude Satellites

3.4.1 Defense Meteorological Satellite Program (DMSP)

DMSP consists multiple polar-orbiting satellites, which orbit near circularly around the Earth every 102 min with a height of 835-850 km. The orbits are of high inclination angle 98.8° and are Sun synchronous, mostly lying in dawn-dusk meridian plane. Data from the onboard

SSJ4 particle detectors are employed to examine the distribution of precipitating particles above the auroral oval, in order to validate the auroral boundaries identified in optical observations. SSJ4 has an aperture always points toward the local zenith, therefore can sample precipitating particles within the atmospheric loss cone. It detects both electrons and ions from 32 eV to 30 keV with 1-s resolution. Although this energy range is usually sufficient to capture diffuse electrons, a fraction of protons with energy higher than 30 keV could be missed.

3.4.2 Fast Auroral SnapshoT (FAST)

FAST satellite has an elliptical and near-polar orbit of 400 x 4000 km in altitude with a period of 133 min [*Carlson et al*., 1998]. Different from DMSP, FAST's orbit progresses around the Earth in local time and thus rotates to the midnight sector of the auroral oval and measures precipitation there. The particle detector on board records electrons and ions at different pitch angles within the energy range of 4 eV and 3 eV to 25 keV, respectively. In this study, only measurements at 0° (parallel to the magnetic field vector) is employed to acquire precipitation information.

Chapter 4. Evolution of Large-scale Auroral Oval

4.1 Methodology and Event Selecting Criteria

Before determining the equatorward boundaries of auroral emissions, we first smoothed and fitted the data to reduce fluctuations and noise. The Hβ (486.0 nm) intensity data were smoothed in time and in latitude, and were then fitted as a function of latitude at each sampling time using a double-Gaussian function in a similar way to *Mende et al.* [2003]:

$$I = a_0 e^{-(y-a_1)^2/2a_2^2} + a_3 e^{-(y-a_4)^2/2a_5^2} + a_6$$

The first two terms give two Gaussians, where a_0 and a_3, and a_1 and a_4, indicate the amplitudes and locations of the latitudinal emission peaks, respectively, and a_2 and a_5 give the associated widths. The constant term a_6 reflects the background, which is assumed to be independent of latitude. The linear term used by *Mende et al.* [2003] denoting airglow was dropped from the fitting function since it was already deducted in the standard NORSTAR data calibration processes.

A background emission was then subtracted from the fitted data to exclude any atmospheric scattering. Although a "background" term is already acquired explicitly in the fitting, it at times gives unrealistic estimations. Thus we separately defined the background as the most-poleward or the most-equatorward located emissions at each sampling time, whichever was lower. This selected a reference intensity at a location far away from the auroral oval and thus primarily filled with scattered auroral emissions.

The proton equatorward boundary was determined as the latitude that crosses an intensity threshold, which was set to 5 R. This threshold was required in order to select clear proton emissions and to reduce any possible ambiguity that may arise from residual noise. Although

the 5 R threshold was arbitrarily selected, it well depicted the equatorward edge of the Hβ emission band. In fact, the intensity gradient there is large, where the intensity increases 3–10 times from the region equatorward of the boundary to that just poleward of it (as seen in the following section) within ~< 0.2°, suggesting a small uncertainty.

A similar process was performed on the 630.0 nm data except that the fitting was skipped because of the sufficiently large signal-to-noise ratio. The background was defined as the average of the 4 smallest intensity values across the observing range at each sampling time, as the 630.0 nm data could be substantially contaminated by city or moon light. Here we used a 32 R noise threshold, and similarly found that a small modification of the threshold does not significantly change the boundary location. Although documented in a few papers [*Eather*, 1968; *Lummerzheim et al.*, 2001], contributions of proton precipitation to 630.0 nm emission are not well known. We consider such effects to be negligibly small because the 630.0 nm auroras have a different spatial distribution from that of the proton auroras as shown in Section 4.2.

One important uncertainty in determining the locations of the auroral equatorward boundaries comes from projecting the proton and the electron auroras onto a single altitude layer (110 km and 230 km, respectively) in the sky. Emissions usually come from a range of heights and have a finite width in their altitude profiles, for example, 40 km for 630.0 nm [*Solomon et al.*, 1988; *Jackel et al.*, 2003] and 10 km for Hβ nm emissions [*Söraas et al.*, 1974]. To investigate such uncertainties, we modified the projection heights to the low and high altitude limits of the emission profile, and investigated how different is the resultant boundary located from the default 110 or 230 km projection (Section 4.2).

We have surveyed the NORSTAR MSP data from 1997 to 1998 and from 2005 to 2010 during low solar activity, which we identified by times with F10.7 below 100. We selected events when the sky condition was favorable, the aurora intensity was above the noise threshold,

and the low-latitude boundaries of auroras were detected within the FOV. We categorized our results into three groups according to geomagnetic activity defined as quiet ($AE^* < 100$ nT), moderate (100 nT $< AE^* <$ 450 nT), and active ($AE^* >$ 450 nT) times, where AE^* represents the maximum *AE* index in the previous 3 h [*Meredith et al.*, 2009]. (The *AU*, *AL*, and *AE* indices reflect geomagnetic variations at aurora zone in the north-south component. *AU* and *AL* indices are respectively defined as the largest and the smallest values, and the difference is *AE*). We furthermore required geomagnetic activity to be quasi-steady, i.e. quiet time condition persisting longer than 6 h, and the moderate and active time conditions being steady magnetospheric convection (SMC) events [*Kissinger et al.*, 2011]. This enables us to limit the temporal effect, and the variation of our boundary location thus reflects the spatial shape of the auroral oval at different local times.

Following these criteria, we have found 89, 46, and 94 cases for the three categories, respectively. Two representative cases of quiet time are presented in Section 4.2 and those of the other two conditions are analyzed in a similar way and can be found in *Zou et al*. [2012]. A statistical morphology is presented in Section 4.3 by superposing individual boundaries from all cases. There the statistical boundary locations were calculated as the median value of all the individual boundaries in each category, together with additional temporal smoothing over 1 h.

4.2 Case Study: Quiet Time

An example of a quiet time case on Feb 17, 2009 is given in Figure 4.1. Figure 4.1a presents geomagnetic indices in a similar format following *Kissinger et al.* [2011]. However, only AE^* is used to detect the quiet period. As seen in the top panel, AE^* was smaller than 100 nT from 00 to 10 UT, and thus satisfied our quiet time definition. The quasi-steady activity indicates

that the variations of the auroral equatorward boundaries result from spatial morphology, rather than temporal evolution.

Figure 4.1b shows the emissions measured at Gillam as a function of magnetic latitude from ~20.5–2.5 MLT (03–09 UT). The top two panels show white light observations along the Gillam magnetic meridian from THEMIS ASI, which have been background-subtracted similarly as NORSTAR 630.0 nm data, and are projected onto altitudes of 110 and 230 km. The bottom two panels present NORSTAR MSP observations at 630.0 nm (electron auroras), and at 486.0 nm (Hβ, proton auroras) wavelengths. The boundaries of the electron and the proton auroras are marked as the red and white curves, respectively, derived using the method described in Section 4.1. As seen, they well mark the equatorward edges of the auroral luminosities. Both boundaries are overlaid on the white light observation.

The proton aurora initially extended equatorward of the electron aurora before ~21.5 MLT (04 UT). Both moved equatorward with increasing MLT until ~0.4 MLT (07 UT) and became roughly overlapped near 67° MLAT during ~21-0.4 MLT (0330–07 UT). After that, the proton boundary moved poleward, while the electron boundary continued to penetrate equatorward until ~2.0 MLT (0830 UT), resulting in an increasing separation. Before ~20.5 MLT (03 UT) and after ~2.4 MLT (09 UT), the proton aurora was too weak to for deter mining its boundary.

Figure 4.1 (a) Geomagnetic conditions on Feb 17, 2009 showing *AL*, *AU*, *AE* and *AE** (top), d*AL*/dt in nT/min (middle), and *AL* steadiness (bottom). The overlaid green curves indicate the segments that meet the requirements of a SMC defined by [*Kissinger et al.*, 2011]. (b) Emissions measured at Gillam as a function of magnetic latitude from 03 to 09 UT. Keograms along the Gillam magnetic meridian from the THEMIS ASI white light projected onto 110 and 230 km are shown in the top two panels. NORSTAR MSP observations at 630.0 nm, and 486.0 nm are shown in the third and fourth panel, respectively. The red and white curves indicate the boundaries of the electron and the proton auroras. The red dashed lines imply the uncertainties of the 630.0 nm boundary (c) Selected snapshots taken by THEMIS ASI at the Gillam station. White lines are isocontours of magnetic latitude of every 5° and longitude of every 15° in the AACGM coordinates. The blue lines indicate the magnetic midnight. The equatorward edge of the auroral oval is implied by the red arrows. [*Zou et al.,* 2012]

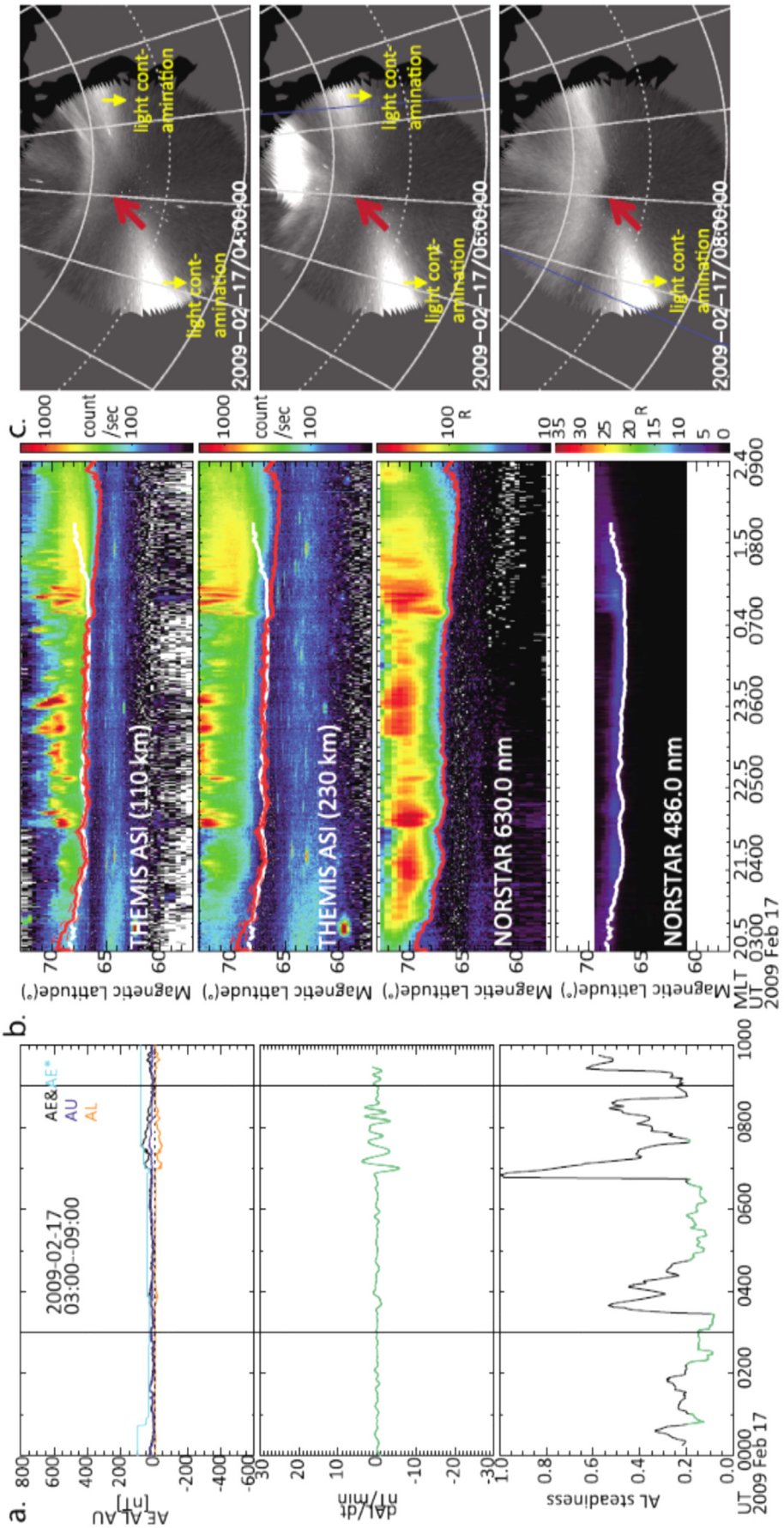
a.
b.
c.
2009-02-17
03:00--09:00
AE&AE*
AU
AL
AE AL AU
[nT]
dAL/dt
nT/min
AL steadiness
UT
2009 Feb 17
MLT
Magnetic Latitude(°)
THEMIS ASI (110 km)
THEMIS ASI (230 km)
NORSTAR 630.0 nm
NORSTAR 486.0 nm
count /sec
R
light cont-amination
2009-02-17/04:00:00
2009-02-17/06:00:00
2009-02-17/08:00:00

By comparing the electron and the proton auroral boundaries with the white light observation, we find that the electron boundary better depicted the equatorward edge of the white light auroral oval, which appeared as a transition from the light blue to the deep blue background color, at the projection height of 230 km than 110 km. In fact, the white light emissions projected onto 110 km extended significantly equatorward of the 630.0 nm boundary before 04 UT. This could not be due to high-energy precipitation, which ceases poleward of the low-energy precipitation. Rather, it resulted from inappropriate mapping of the low-energy precipitation to 110 km instead of 230 km. This indicates that the equatorward edge of the white light auroral oval was substantially contributed by the 630.0 nm emission and that THEMIS ASI can be used to infer the location of the electron auroral boundary. On the other hand, contributions from the proton aurora could not be clearly identified, as seen in the interval before ~21.5 MLT (04 UT) where the proton aurora extended further equatorward of the electron aurora, whereas the white light oval was still bordered by the 630.0 nm boundary. However, this could be due to the faint Hβ emission in this case. Examination of intense proton emissions is necessary.

To estimate the uncertainties arising from single-altitude projection, we modified the projection heights to the low and high altitude limits of the emission profile and the resultant boundaries are shown in the top two panels in Figure 4.1b as the red dashed lines for the 630.0 nm measurement. They differ from the origin boundary with an overall small (~0.2°) displacement, except around 20.5 MLT (03 UT) where it reached ~1°. This is because the auroral oval there was located far away from the zenith. Such boundaries of the 486.0 nm measurements are not shown since they basically overlapped with the original one with a negligibly small (~<0.2°) displacement.

Figure 4.1c shows selected snapshots from the THEMIS ASI at Gillam. White lines give magnetic latitude every 5° and longitude every 15° in Altitude Adjusted Corrected

Geomagnetic (AACGM) coordinates. The equatorward edge of the auroral oval is indicated by the red arrows. Although light contamination existed in the southwest FOV due to city light contamination, clear sky condition was found along the central longitude and along the central latitude. These 2-D snapshots show that the auroral oval was smoothly aligned in the east-west direction and stayed quasi-steady during this period. This suggests that the identified equatorward boundaries are not significantly affected by small-scale or rapid time changes but reflect the large-scale spatial structure. Furthermore, this demonstrates that a 2-D map of auroral boundary could be possibly inferred if the boundary location at one longitude, here the MSP longitude, is known.

Figure 4.2a shows that during this event, the footprint of the DMSP 13 satellite passed above Gillam (red X), footprint being mapped from the southern hemisphere using the T01 magnetic field model [*Tsyganenko,* 2002a, 2002b]. Figure 4.2b shows the DMSP integrated energy flux of precipitating electron and ions (top two panels) and differential electron and ion energy fluxes (bottom two panels) along the mapped trajectory. We focus on the differential fluxes for their better reflection of the low-energy precipitation that accounts for the emissions at the auroral oval equatorward edge. The equatorward boundaries of the differential fluxes, illustrated by the magenta lines, were consistent with the optical boundaries and the associated uncertainties, although the measured precipitating protons were limited to energies below 30 keV. This indicates that protons with energy above 30 keV did not contribute substantially in this event. The small discrepancy of the electron boundary was partially due to the gradual flux drop where a boundary cannot be uniquely determined. Figure 4.2b also shows that the equatorward boundary of the precipitating electrons was located near, but just equatorward, of the proton precipitation boundary, consistent with the optical observations.

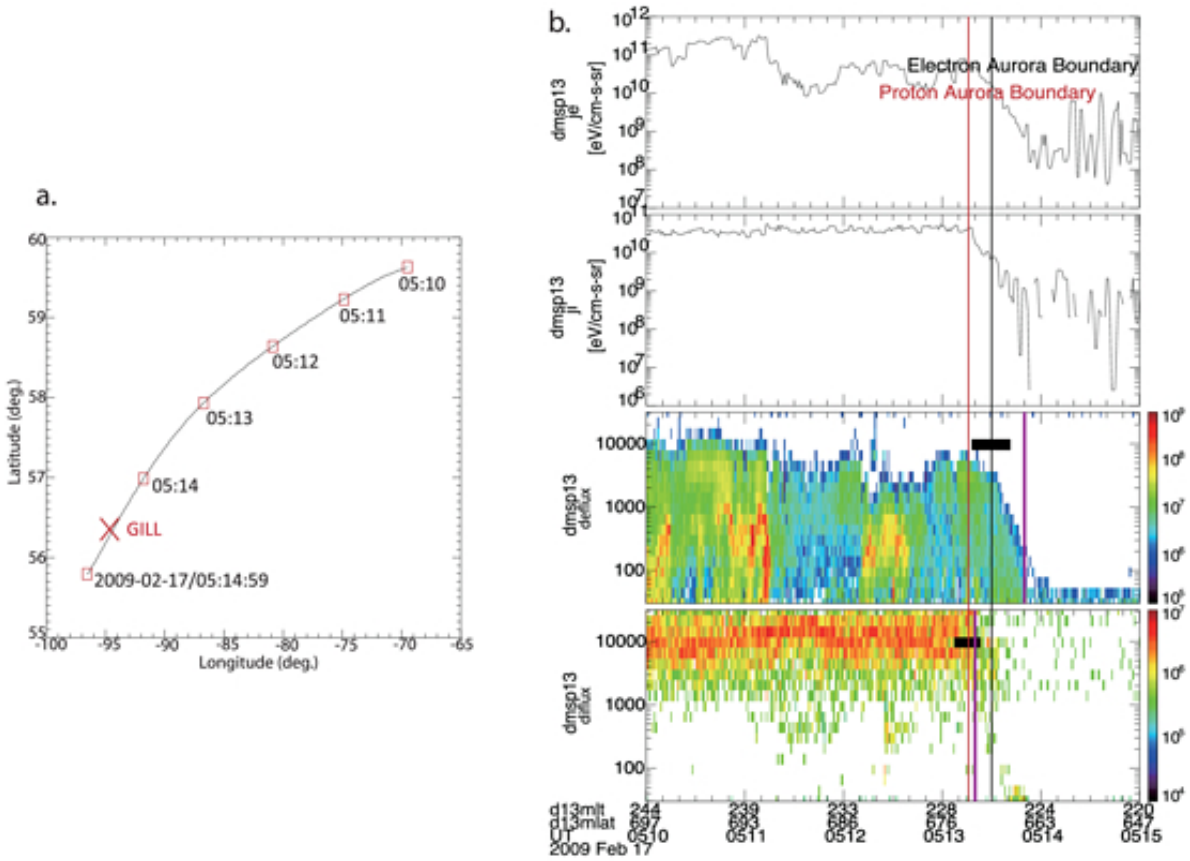

Figure 4.2 (a) The snapshot of the DMSP 13 satellite footprint mapped from southern hemisphere for the quiet time case, which crossed above the Gillam station. The black curve represents the mapped trajectory of DMSP13 spacecraft and the red squares imply the locations of the spacecraft at the time indicated on the right. The red cross shows the location of NORSTAR GILL station. (b) DMSP data along the trajectory with integrated electron and ion energy fluxes (top two panels), differential electron and ion energy fluxes (bottom two panels). The vertical black and red lines imply the mean locations of low latitude boundaries of the electron and the proton auroras shown in Figure 4.1b during this 5 min interval and the horizontal bars in the spectrograms indicate the estimated uncertainties resulting from the finite altitudinal distribution of the auroras shown in Figure 4.1b. The equatorward boundaries of precipitating particles are illustrated by the magenta lines. [*Zou et al.*, 2012]

Figure 4.3 shows a second example during a quiet geomagnetic period on February 23, 2007, when the proton aurora was more intense and extended further equatorward of the electron aurora than for the first example. The electron and the proton auroral boundaries depicted the luminosity cutoff of the NORSTAR observations. Between 22.5 and 23.5 MLT (05–06 UT), the proton aurora stayed at ~65–66° MLAT, equatorward of the electron aurora, which was located at ~66° MLAT. The white light auroral intensity (top two panels of Figure 4.3b) extended equatorward of the electron boundary and was delineated by the proton

boundary for both the 110 and 230 km altitude mappings. This implies that in this case the proton aurora was responsible for the most equatorward band of the diffuse glow in the white light observations. However, it is worthwhile to emphasize that this diffuse glow in white light is mostly contributed by emissions of the secondary electrons, which are generated during charge-exchange collisions of the precipitating protons and emit 557.7 nm radiation, because the relative intensity of the Hβ emission was still very small compared with the 557.7 nm emissions.

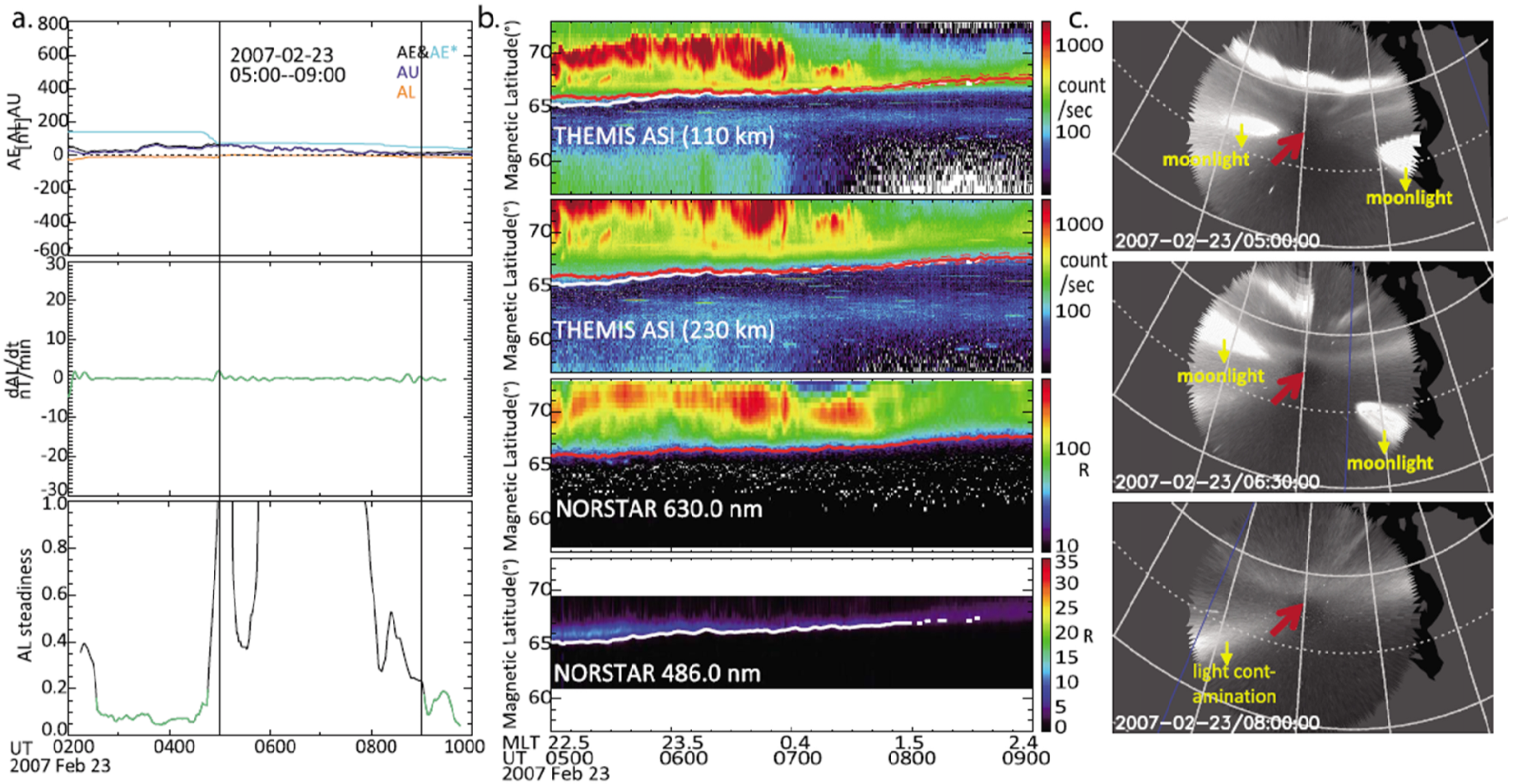

Figure 4.3 (a) Geomagnetic conditions for a second quiet time case on February 23, 2007 in the same format as Figure 4.1a. (b) Keograms from THEMIS ASI white light (top two), NORSTAR 630.0 nm (middle), and 486.0 nm (bottom) emissions for this quiet time case. (c) Selected snapshots taken by THEMIS ASI at the Gillam station. [*Zou et al.,* 2012]

4.3 Statistics

Having presented individual case studies above, we now discuss the statistical behavior of the electron and the proton auroral boundaries under different steady magnetic conditions. Figure 4.4 shows the boundary locations of the electron and the proton auroras during geomagnetic quiet (left), moderate (middle), and active times (right) as a function of MLT (UT). The vertical line in each panel indicates magnetic midnight. The upper panel of each column gives the equatorward boundaries of the proton aurora for individual cases (black) and the median (blue). The middle panels display the electron aurora boundaries in the same format. The bottom panels show the comparison of the median boundaries of the electron (red) and the proton auroras (blue).

During quiet times, the median boundary locations well represent individual cases within a deviation of ~1° MLAT. The proton aurora moves equatorward from ~67.5° to ~66.5° MLAT in the premidnight sector, and retreats poleward back to ~67° MLAT at 3 MLT (0930 UT). The electron aurora also moves equatorward in the premidnight sector, but with a larger displacement than the proton aurora, from ~67.8° to ~66.3° MLAT, and continues towards equatorward in the postmidnight sector until ~1.5 MLT (0800 UT). As a result, the proton aurora extends slightly equatorward of the electron aurora before ~21 MLT (0330 UT), collocates with it between 21-23 MLT (0330-0530 UT), and stays poleward of it afterwards with an increasing separation toward dawn.

During moderate times, the median locations again well reproduce the general trend of individual boundaries. Both the proton and the electron auroras extend to lower latitude than during quiet times. Different from quiet times, the electron aurora extends equatorward of the proton aurora throughout all MLT sectors. During ~20-0.5 MLT (0230 -0700 UT), the electron boundary shifts substantially equatorward, while the proton boundary displays a more moderate movement. After that, the latitude of the electron aurora continues to decrease until

1.5 MLT (0800 UT), roughly remains at the same location for ~1h, and then moves slightly poleward with increasing MLT. The separation between proton and electron auroras varies from ~0.6° on the post-duskside, to ~2.5° in the premidnight sector, and ~5° in the post-midnight sector.

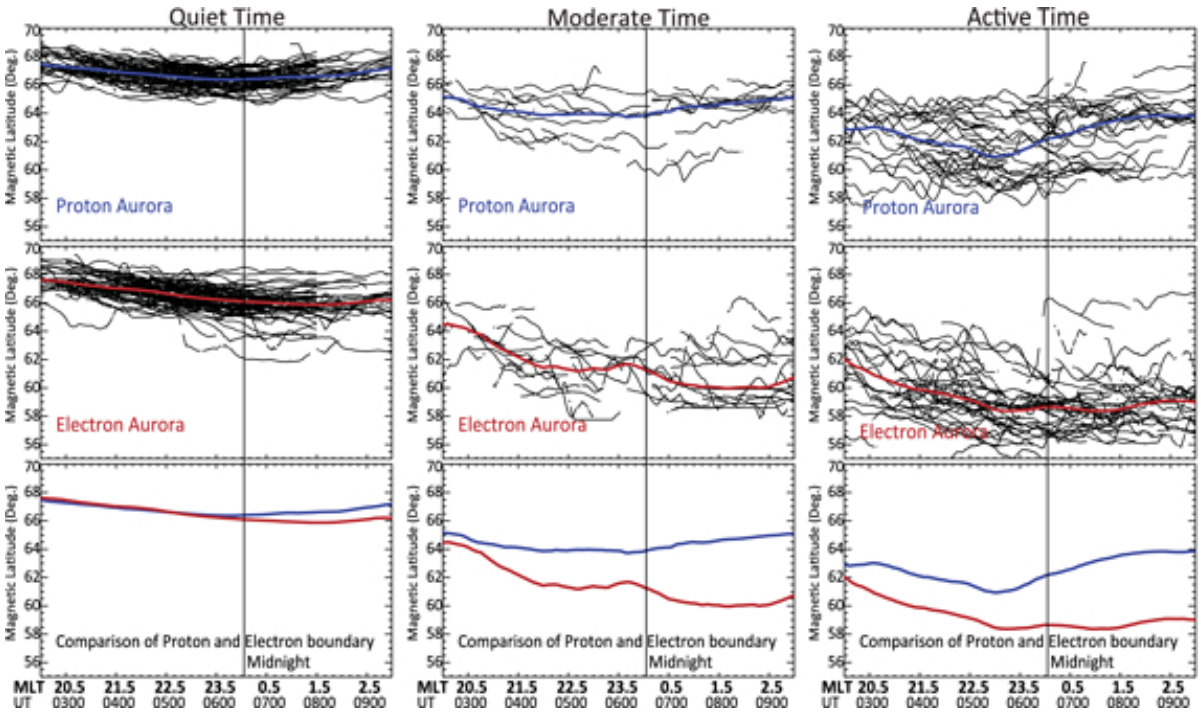

Figure 4.4. The boundary locations of the electron and the proton diffuse auroras during geomagnetic quiet (left), moderate (middle) and active times (right) as functions of MLT (UT) and MLAT. The vertical line in each panel indicates magnetic midnight. The upper panel of each column gives the equatorward boundaries of the proton aurora determined in individual cases (black) and the median (blue). The middle panels display the electron aurora boundaries determined in individual cases (black) and the median (red). Comparison of the median boundaries of the electron (red) and the proton auroras (blue) is plotted at the bottom. [*Zou et al.,* 2012]

During active times, the scattering of individual boundaries around the median locations becomes large (see a discussion below). Similar to moderate times, the electron aurora extends equatorward of the proton aurora throughout the observing MLT range. The median proton aurora boundary initiates at ~63° at 20 MLT (0230 UT), penetrates to lower latitude ~61° until 23 MLT (0530 UT), and retreats to higher latitude reaching ~64° at 3 MLT (0930 UT). On the other hand, the median electron boundary shifts abruptly equatorward, from 62.7° to 58.5° during 20-23 MLT (0230-0530 UT), roughly remains at the same latitude until 1.5 MLT (0800

UT), and then moves slightly poleward. Compared to the moderate category, both the electron and the proton auroras penetrate further equatorward and the separation between them on the post-duskside and dawnside becomes larger.

The following conclusions can be drawn from the comparison of the quiet, moderate, and active times: The crossover region of the electron and the proton auroral boundaries shifts from ~21–23 MLT (0330–0530 UT) for quiet times to duskward of the observable MLT range, or possibly disappear, for the moderate and active times. The overall separation between the electron and the proton auroras increases with increasing geomagnetic activity, the maximum being ~0.8° for quiet times but ~5° in MLAT for moderate and active cases. Furthermore, both the electron and proton auroral boundaries move equatorward with increasing geomagnetic activity.

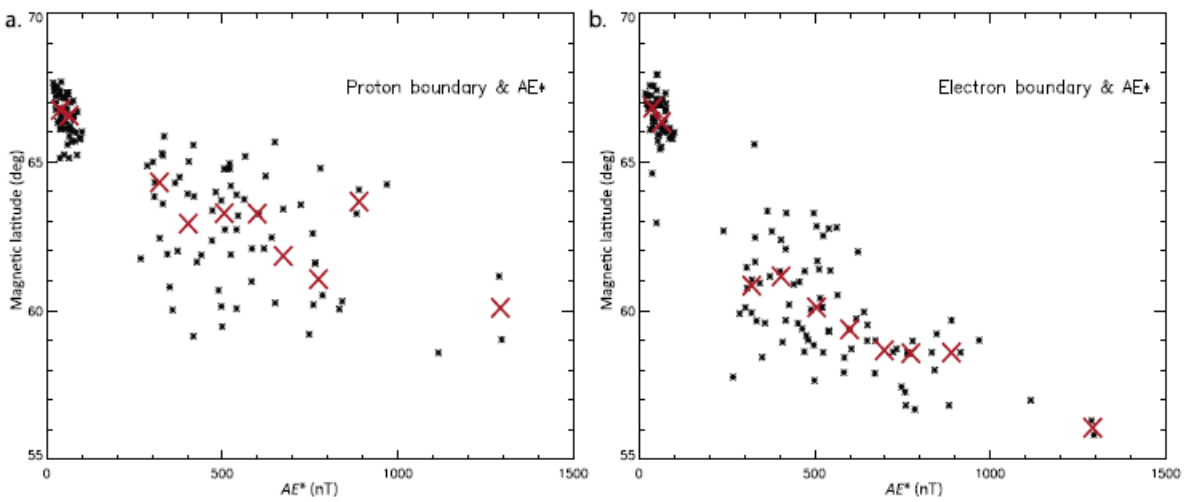

Figure 4.5 Relationship between the mean latitudes of the auroral equatorward boundaries and the mean AE* value during 04–07 UT for protons (Figure 9a) and electrons (Figure 9b). Each asterisk represents the mean boundary location and the corresponding mean AE* value for one case. The asterisks are then binned in each 100 nT range and the median value is given by the red crosses. [*Zou et al.,* 2012]

In order to explain the large scatter of individual cases in the statistical result, as well as to address the dependence of auroral boundary location on *AE**, we investigate the relationship between the mean auroral boundary locations and the mean *AE** value during 04–07 UT and present the results in Figure 4.5a and 4.5b for electrons and protons, respectively. Each asterisk

represents the boundary location and the corresponding *AE** value for one case. The asterisks are then binned in each 100 nT range and the median value is given by the red crosses. Both the electron and the proton auroral boundaries display a clear dependence on *AE**, i.e. moving equatorward with increasing *AE**, and this dependence is much more prominent for electrons.

4.4 Discussion and Summary

Here we discuss the inherent limitations in the above statistics. First, the different projection altitudes of the two emissions lead to uncertainties in determining their relative locations, considering that the geomagnetic field lines are oblique. This is estimated to be ~ 0.24° in MLAT. Although small, it still causes an underestimation of the separation when the proton aurora extends equatorward of the electron aurora, and an overestimation when it is reversed. This would also lead to a slight shift in MLT of the crossover region between the two auroras. Second, the proton precipitation is assumed not to generate significant 630.0 nm emissions, which could place the electron boundary further equatorward than it should be. It would also imply that the separation between the proton and electron auroras is larger than determined here. Third, auroral emissions are assumed to be emitted from thin layers at altitudes of 110 or 230 km, and the uncertainties have been analyzed to be as large as ~1° above.

We have examined the MLT distributions of the equatorward boundaries of the electron and the proton auroras based on NORSTAR MSP observations during quasi-steady geomagnetic activity conditions. The comparison with the THEMIS ASI data implies that the two types of auroras both contribute to the diffuse white light observations, which can be important for interpreting such observations, and that the THEMIS ASIs could be applied for obtaining the 2-D spatiotemporal evolution of the electron and the proton aurora. We also studied the conjunctions between NORSTAR MSP and DMSP satellite data to demonstrate the validity of our optical results. For all of these conjunction events, the precipitation measured

along the DMSP trajectories in either northern or southern hemisphere qualitatively agreed with the optical observations.

We draw two main conclusions:

1. During geomagnetic quiet times, the equatorward boundary of the proton aurora is situated equatorward of the electron aurora prior to 2100 MLT (0330 UT), and is reversed after 2300 MLT (0530 UT) with a latitudinal separation that increases toward dawn, indicating a crossover region at 2100–2300 MLT (0330– 0530 UT) in the premidnight sector.

2. During the moderate and active SMCs, the electron auroral boundary lies equatorward of that of the proton aurora throughout the entire nightside. From the post-duskside to postmidnight sectors, the latitudinal separation between them increases from 0.6° for moderate time and 1–2° for active time, to 5° MLAT. This result suggests that the overlapping region located at 21–23 MLT during the quiet times, moves toward duskward of the observable MLT range, or perhaps disappears during the moderate and active times.

The conclusions described above include important differences from previous works. Differences with prior optical observations can be attributed to the fact that 630.0 nm emission is more sensitive to lower energy (< 1 keV) electron precipitation than the 557.7 nm emission used in prior ground-based observations and the FUV in satellite imaging. The disagreements with the in situ measurements are more difficult to evaluate because the auroral distribution at 21–04 MLT sector was not observed by the DMSP spacecraft used by *Gussenhoven et al.* [1987]. Nevertheless on the post-duskside sector, they did not detect the equatorward penetration of the electron auroras during active SMCs as shown here. This could arise from the differences in geomagnetic conditions: large geomagnetic disturbances such as substorms were included in their data set but excluded from our steady geomagnetic intervals.

Chapter 5. 1-D Relation between PBIs and Localized Polar Cap Flow Enhancements

5.1 Event Selecting Criteria

We examine the relation between PBIs and localized polar cap flow enhancements using coordinated observation of THEMIS white light ASI and the SuperDARN radar both located at Rankin Inlet (RANK). The FOV of this ASI usually covers the poleward portion of the auroral oval and thus is suitable for identifying PBI activity. The radar located at the same location looks poleward into the polar cap regions, measuring LOS ionospheric flow speeds (roughly north-south aligned). Due to radar's low temporal resolution (1–2 min), we mainly discuss the auroral and flow evolution on the time scale of minutes. However, the occasional high temporal resolution (8 s) data enables us to study the flow evolution timing more precisely.

For our database, we required favorable sky condition and relatively good radar coverage, especially between the 0 and 11 range gates (~74°–78.5° MLAT), which are located just poleward of the most probable latitudes of the auroral poleward boundary [*Nishimura et al*., 2010a]. The short range of these echoes indicates that the radar signals only travel a short distance before getting backscattered [see, e.g., *Koustov et al*., 2007], so that the altitude of backscatter is expected to be in the *E* region ionosphere [*Gorin et al*., 2012; *Lyons et al*., 2011, Figure 11]. As a result, the flow magnitude will be less than the full E × B drift speed and limited below the ion acoustic speed (~400 m/s) [*Haldoupis*, 1989; *Koustov et al*., 2005], and the mean flow angle will be shifted from the E × B direction by ~20° [*Gorin et al*., 2012]. However, these do not influence our results because we only study relative changes in flow speed magnitudes instead of the absolute values.

The auroral poleward boundary should be clearly identified and be located equatorward of the radar echoes. We focused on the UT interval that places RANK close to the 24 MLT meridian, namely, 0400–0800 UT (2130–0130 MLT). Here, with expectation of two-cell convection, the north-south velocity component of polar cap flows, i.e. the component measured by the radar, is more likely to be the dominant flow component. While we cannot measure the azimuthal component, such motion is roughly parallel to the nightside open-closed boundary and is not expected to contribute significantly to flow's crossing the boundary.

For accurate identification of the auroral poleward boundary, we also compared the boundaries identified from optical images with those from in situ precipitation measurements from the FAST satellite. The optical poleward boundary was identified as the poleward most luminosity gradient, and the in situ poleward boundary was the poleward most gradient of the energetic electrons' differential energy flux or integrated energy flux.

5.2 Comparison of Auroral Poleward Boundary Detected by White Light ASI and FAST Satellite

Conjunctions between RANK ASI and FAST satellite in January–April 2009 were examined when sky conditions were clear, FAST passed across the RANK ASI station, and electron precipitation data were available. Two such conjunctions are found and one is presented as below. Figure 5.1 shows snapshots of the RANK ASI with the FAST satellite footprint, as well as FAST observations of electron energy spectrogram at 0° pitch angle and total energy flux on 16 February 2009. The snapshot displays the auroral oval just before FAST moved into the FOV and during the FAST traversal of the optical poleward boundary. North is at the top and west is on the left.

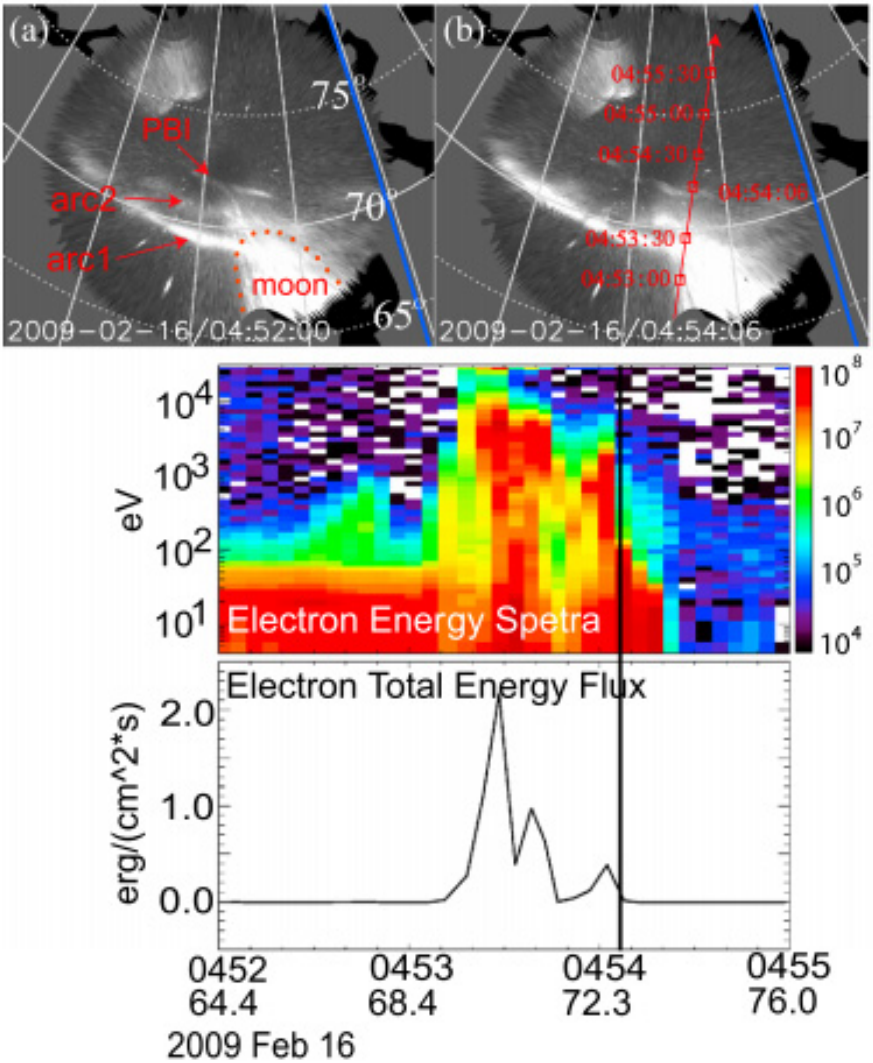

Figure 5.1 Snapshots of RANK ASI overplotted with FAST satellite footprints, as well as FAST observed electron energy spectrogram at 0° pitch angle and total energy flux. The two snapshots display the auroral oval just before FAST came into FOV and during FAST's traversal. White lines in the snapshots are isocontours every 5° magnetic latitude and every 15° longitude in AACGM coordinate. The blue lines indicate the magnetic midnight. FAST satellite footprint are denoted as red squares, and the direction of spacecraft motion is shown by the red arrow. Moonlight contamination and its reflection are indicated by text in the snapshots and the borders of them are also highlighted as the dotted red line. The time when FAST was mapped onto the optical auroral poleward boundary is also denoted as the black line in electron energy spectrogram and total energy flux. [*Zou et al.*, 2014]

There were thin intensifications aligned at ~72° MLAT (marked as PBI in Figure 5.1a). These arcs were identified as PBIs along the optical poleward boundary because no auroral emissions poleward of them were detected. Equatorward of the arcs, two azimuthally aligned arcs (arc1 and arc2 in Figure 5.1a) were observed. The FAST satellite passed across the ASI

FOV as shown in Figure 5.1b and mapped onto the poleward edge of the PBIs at 0454:06 UT. This time is also marked as the vertical line in the FAST observations.

The FAST observations, of both the electron energy spectrogram and the total energy flux, exhibited two peaks of precipitating energetic electrons during 0453:20–0453:50 UT, consistent with the arc1 and arc2 identified in the ASI. FAST encountered the most poleward peak of electron precipitation just before 0454:05 UT. This peak coincides with the PBI in ASI, and the smaller energy flux (~0.4 erg*cm^{-2} s^{-1}) agrees well with its fainter brightness than that of arc1 and arc2. After 0454:05 UT, the electron precipitation exhibited a rapid and substantial decrease in energetic electrons (>1 keV). The decrease is also clear in the total energy flux which dropped a factor of 3–4 within ~10 s. This dramatic drop-off is defined as the poleward boundary of the auroral precipitation [*Newell et al*., 1996] and has been used to determine the location of the auroral poleward boundary when comparing with optical observations [*Kauristie et al*., 1999; *Baker et al*., 2000; *Milan et al*., 2003]. Hence, the optical auroral poleward boundary derived from the white light ASI is consistent with the boundary of the main auroral oval inferred from low-altitude in situ particle measurements.

Previous works have compared the optical auroral poleward boundaries using specific wavelengths with in-situ data in large dataset, and showed a reasonable agreement with deviation varying from <1° to ~2° [*Blanchard et al*., 1997; *Kauristie et al*., 1999; *Baker et al*., 2000; *Carbary et al*., 2003; *Milan et al*., 2003; *Boakes et al*., 2008]. Our results, though limited to two cases, are consistent with and maybe show even better agreement, than previous works. This consistency implies that the sensitivity of the white light ASI is comparable with the other optical instruments used in previous work and that the potential uncertainty may also be limited to 1–2°.

The ~1° uncertainty is negligible for this study because the ASI captures the peak of the most poleward energetic precipitation even though the precipitating population on the flank of

the “inverted V” may be missed. This uncertainty is still small enough to ensure the flow channels observed are located in the polar cap. As shown later, the radar FOV is often located slightly poleward of the auroral poleward boundary and in the FOV, the observed flow channels usually span >4° in latitude. Therefore, the conjunctions between THEMIS ASI and FAST provide support for using white light PBIs to represent the most poleward energetic electron precipitation that is located along the poleward boundary of the main auroral oval.

5.3 Polar Cap Flow-PBI Association: Starting with PBIs

Isolated, intense PBIs were identified as those having only weak (<~1000 count/second) preceding auroral activity along the poleward boundary for > ~10 min and then a step-like intensity change (>500 count/second) in time. These PBIs should also be located within ± 1 h MLT from the radar station so that the flows associated with them have a high probability of being captured by the limited radar FOV. To define an enhanced polar cap flow, we required a >200 m/s increase in the equatorward flow speed above the background flow, background being the median value of the lowest 40% LOS speeds within 0-11 range gate at each scan. Such background is usually of small magnitude (<100 m/s) and smoothly varying with time.

Isolation and intense luminosity of PBIs were required in order to establish clear associations with polar cap flows. For example, the 1000 count/second threshold for PBI intensity is a reasonable distinction between faint, subtle auroras, such as diffuse auroras along the equatorward boundary (hundreds of count/s; see *Zou et al*. [2012, figures]), and bright, significant intensifications such as substorm brightening and expansion (thousands of count/s; see *Nishimura et al*. [2011, 2012, figures]). The 200 m/s threshold for flow speed filters the small background variations (~100 m/s) and picks out substantial flow enhancement. The 10 min separation between PBIs ensures that we obtain several data points to resolve the flow evolution in 1–2 min cadence.

5.3.1 Case Study

Figure 5.2a shows simultaneous observations from the RANK radar and ASI on 23 January 2009. The bright luminosity at the southeast corner is due to moonlight contamination, and the border of this contamination is marked as the dotted red line surrounding the moonlight. Initially, the auroral poleward boundary, identified as described in Section 5.2, was located at ~71° MLAT with faint auroral activity along it. Although it intersected the edge of the moonlight, moonlight there was weak and steady in time, so that variation in auroral activity, such as PBIs, can still be distinguished. The flow was weak (<100 m/s) initially within the polar cap region poleward of the boundary.

Starting at 0434 UT, the flow speed from the center to eastern part of the FOV increased to ~150 m/s directed equatorward, as marked by the orange arrow, and the area of flow enhancement extended toward the auroral poleward boundary. Associated with it, a faint PBI (mostly <1000 count/second, also marked by an orange arrow) occurred at 0438 UT. At 0440 UT, a further flow enhancement (marked by the red arrow) appeared in the central FOV of radar with a speed at least 200 m/s greater than that of the background, and penetrated toward the auroral poleward boundary. This flow enhancement was not a gradual built up but a sharp increase in time as seen better in the time series plot of Figure 5.2b. That it suddenly appeared across several range gates is a common feature of all the flows we studied and suggests the flow propagating time is shorter than the radar time resolution. This flow was immediately followed by an even more intense PBI (marked by the red arrow) with an abrupt and significant intensity increase from the first one (seen in Figure 5.2b). This PBI is above the threshold and is our main focus in this case. The enhancements of flow and PBI activity both persisted for ~10 min, and, after their disappearance, a third flow enhancement and PBI (marked by yellow arrows) were detected at 0453 UT, although this flow was almost outside the radar FOV. This case suggests that the PBIs were associated with and preceded by the enhanced flows just

poleward of them. These flows were narrow in longitude and were propagated towards the auroral poleward boundary, although it is not completely certain whether they arrived at the boundary due to the limited radar FOV.

Figure 5.2b shows the time series plot of the ASI and the radar observations for this case in both north-south (top four panels) and east-west (bottom two panels) slices. The longitudinal coverage of the ASI N-S slices is shown as partially transparent blue stripes in the first snapshot in Figure 5.2a. The flow measurements shown here are from beams that capture the start and the end of flows, and the background flow speed has been subtracted as described above to emphasize the >200 m/s equatorward flow enhancements.

The indicated flow-PBI sequences are the same as those identified in the 2-D snapshots and are highlighted by the arrows with different colors for different pairs of flow-PBI association. For example, as shown by the orange arrows, the moderate flow enhancement at 0434 UT was followed by a faint weak PBI initiated after 0437 UT. As indicated by the red arrows, the flow further exhibited significant enhancement at 0440 UT and then the isolated and intense second PBI appeared 1 min later. The flow persisted for 13 min and the PBI for 10 min, as shown by the rectangles. The width of the PBI during its first 2 min was 1.1 h MLT as visually measured from the 2-D snapshot. And the initial width of the region of flow enhancement spanned seven beams, determined from the half width of flow velocity profile from the bottom panel, corresponding roughly to a 0.35 h MLT width. The conversion from numbers of beams to longitudinal width in MLT is shown as the pink axis on the right side of the panel.

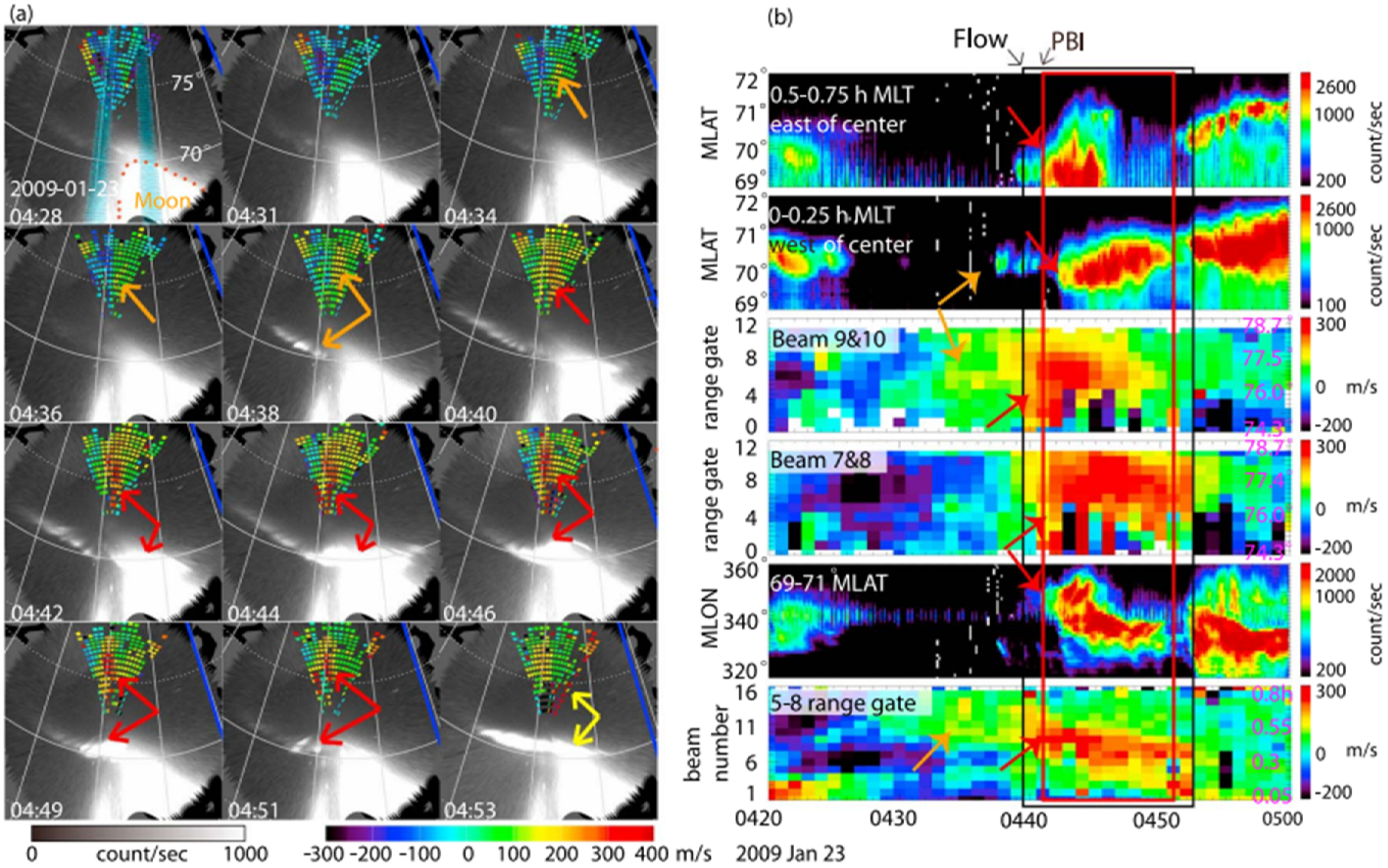
(a)
75°
70°
2009-01-23
Moon
04:28
04:31
04:34
04:36
04:38
04:40
04:42
04:44
04:46
04:49
04:51
04:53
0 count/sec 1000
-300 -200 -100 0 100 200 300 400 m/s
(b)
Flow
PBI
0.5-0.75 h MLT
east of center
0-0.25 h MLT
west of center
MLAT
72°
71°
70°
69°
2600
1000
200
100
count/sec
Beam 9&10
range gate
12
8
4
0
78.7°
77.5°
76.0°
74.3°
300
0 m/s
-200
Beam 7&8
78.7°
77.4°
76.0°
74.3°
69-71 MLAT
MLON
360°
340°
320°
2000
1000
5-8 range gate
beam number
16
11
6
1
0.8h
0.55
0.3
0.05
0420
0430
0440
0450
0500
2009 Jan 23

Figure 5.2 (a) Snapshots of simultaneous observation from radar and ASI both at RANK on 23 January 2009. Moonlight contamination is marked. Doppler velocity measured by radar is color coded as the color bar. Three pairs of flow-PBI association are identified and indicated as arrows of different colors. (b) Time series plot of ASI and radar observations. The top two panels show ASI N-S slices, as a function of magnetic latitude, at magnetic longitude 0.5–0.75 h MLT east of and 0–0.25 h MLT west of the center of FOV, respectively. The following two panels show the average velocity of certain two beams (as marked) as a function range gate, and magnetic latitude (right axis). The second panel from the bottom displays the ASI E-W slices within 67°–71° magnetic latitude range as a function of magnetic longitude. The bottom panel presents the median velocity for each beam among 5–8 range gates, i.e., each pixel represents the median flow speed from 5 to 8 range gates at a particular beam and at a particular time. The y axis is beam numbers 1–16, indicating beam directions which step in azimuth from west to east. A rough conversion of longitudinal width is made from number of beams (same y axis) to hours of MLT (pink on the right of the panel). The flow-PBI associations are highlighted as arrows, and particularly, the appearance of the second pair is indicated by rectangles. [*Zou et al.*, 2014]

While the previous event only has 1 min radar time resolution, the event in Figure 5.3 has high-resolution 8-s data and allows for a more accurate identification of the timing. Figure 5.3b shows the time series plot of a case on 2 April 2008 in a similar format as Figure 5.2b. The high resolution measurements along beam 8 are shown in the fifth panel. This beam is located at the center of the radar FOV and oriented toward magnetic north. Although the background has not been subtracted because of the beam's much higher time resolution than for the other beams (background calculation requires multiple beam measurements, see Section 5.1), the flow enhancements can clearly be seen. The auroral poleward boundary was quiet without significant intensifications until 0516 UT when the luminosity reached above the threshold at 0.5 h west of the center of the FOV (marked by the red arrow). This intensification spread out in longitude as seen in the east-west keogram of RANK (the sixth panel).

The low-resolution 2-min data (third and fourth panels) show the flow speed increased from $<\sim 100$ m/s to $>\sim 200$ m/s by 0516 UT, simultaneously with the onset of PBI intensification. The high-resolution data, however, shows that the flow enhancement actually initiated slightly earlier than 0516 UT. As clearly seen in the fifth panel, flow speed along beam 8 changed from dark blue (<0 m/s) to green and then to yellow (~100 m/s) during 0515–0516

UT, reaching orange and red at 0516 UT (> ~ 200 m/s). On the other hand, no substantial intensification of PBIs was observed until 0516 UT. Thus despite of the simultaneous appearance of the polar cap flows and the PBIs as shown in the low-resolution observation, the high-resolution data show that the initiation of the flow velocity enhancement actually preceded that of the PBI luminosity by ~1 min.

Representative snapshots for this flow-PBI association are shown in Figure 5.3a. The radar echo coverage was high along the central beams but limited at the western and eastern edges. Except for the persistent strong equatorward flows along the western beams, the flow within the rest of the FOV was weak. At 0516 UT, a fast flow channel appeared near the center FOV (red arrow) and extended toward the auroral poleward boundary. Until this time, the auroral emissions along the boundary remained faint. In the next two snapshots both the enhanced polar cap flow and PBI (red arrow) become highly visible. At 0528 UT, the second, even more intense, PBI was detected (orange arrow). To the east of the previous flow enhancement, we also see another flow velocity enhancement (orange arrow) which was only partially captured. This flow enhancement seems to be related to the second intensification.

The above two cases show that, associated with isolated and intense PBIs, there existed longitudinally narrow fast flows in the polar cap extending toward the auroral poleward boundary. Furthermore, both of the cases indicate that these flows appeared earlier than the PBIs. Their durations were comparable to and their widths were on the same order of PBIs. The PBIs that were not isolated or intense were also found to be associated with flow enhancements, although such PBIs are beyond the main focus of this paper. These results are consistent with *Nishimura et al*. [2010b] and *Lyons et al*. [2011], and the high-resolution data newly used here allowed us to identify the time lag with a much higher accuracy.

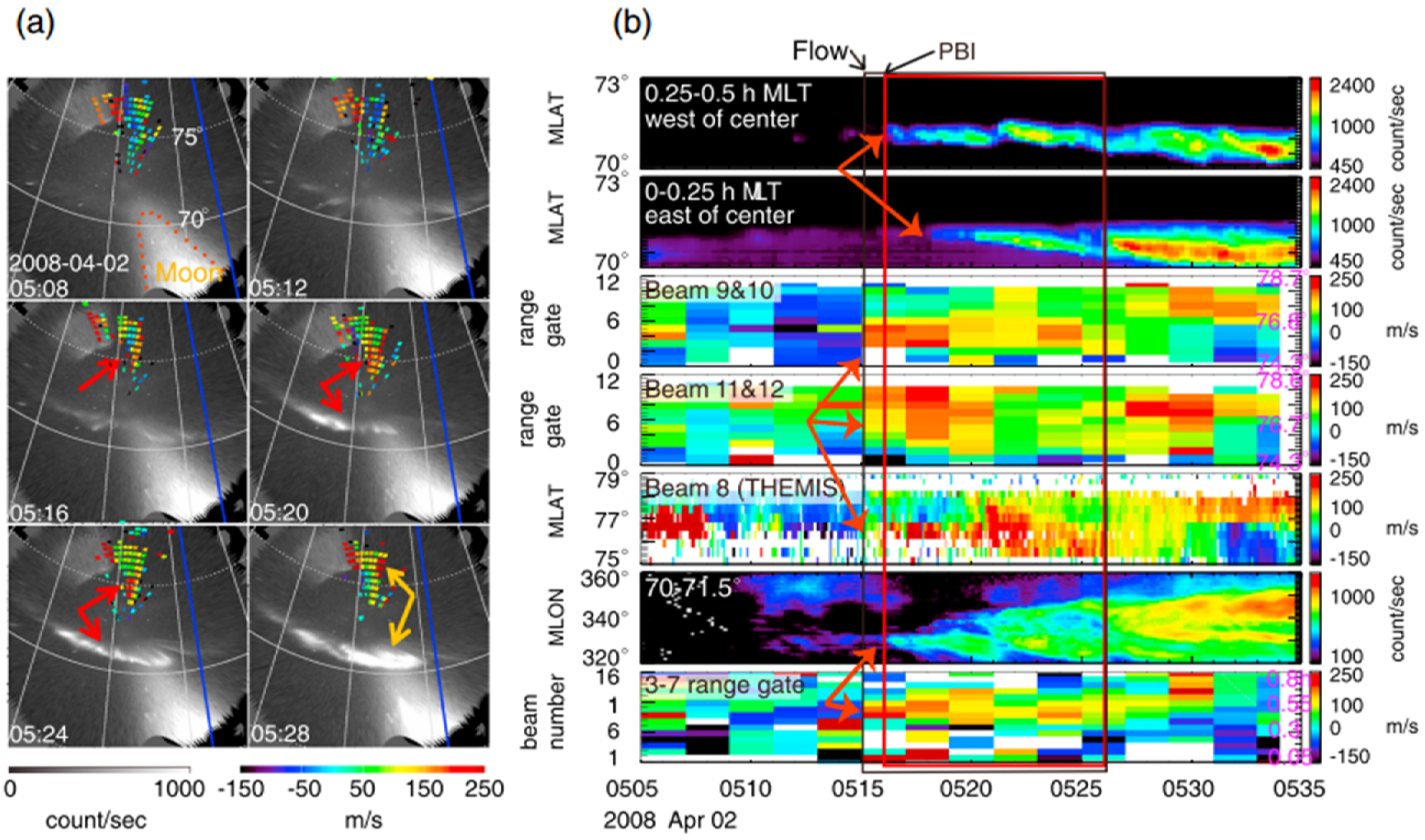

Figure 5.3 (a) Selective snapshots of simultaneous observation from radar and ASI on 2 April 2008 showing the flow-PBI association. Two pairs of flow-PBI association are identified and indicated as arrows of different colors. (b) Time series plot of ASI and radar observations in a similar format as Figure 5.2b except for the 8 s mode in the fifth panel. [*Zou et al.*, 2014]

5.3.2 Statistics

In 12 months of data (January–April of 2008–2010), we found 49 isolated intense PBIs, and their correlation with enhanced polar cap flows is shown in Figure 5.4a. Among these PBIs, 26 isolated PBIs were found to be associated with isolated enhanced flows (> ~ 200 m/s above the background), which were directed equatorward and well separated (~10 min) from previous transient flow activity, implying a one-to-one correlation (Figure 5.3 is an example). There were 15 PBIs associated with multiple equatorward flow enhancements. For these cases, the flow-PBI sequence still potentially exists, since the appearance of those multiple flows often seemed correlated with weaker PBI activity (below our intensity threshold) preceding the intense one (this is the case for the Figure 5.2 event, though the first flow burst was below our flow threshold). Three PBIs were associated with poleward flow enhancements. It is reasonable that some equatorward flows were located outside the radar FOV, and it is not uncommon for there to be flows with a tailward component longitudinally adjacent to the equatorward component as seen in the 0434 and 0436 UT panels in Figure 5.2a. Only five PBIs did not show any association with flow activity.

Considering the limitation of our observations, i.e., the radar FOV is limited and only the LOS component velocity is measured, the probability of PBIs being associated with enhanced polar cap flows (90%) is sufficiently high to conclude that PBI occurrence is commonly correlated with the channels of polar cap fast flows directed toward the open-closed field line boundary.

For the one-to-one association category, we also calculated the time delay between the appearance of flows and PBIs, onset of flow appearance being chosen when the flow velocity shows significant increased within the 0–11 range gate. As shown in Figure 5.4b, flows statistically occurred simultaneously with or 1–2 min prior to PBIs. Here, the simultaneous appearance is likely due to the limitation of the low temporal resolution radar data because

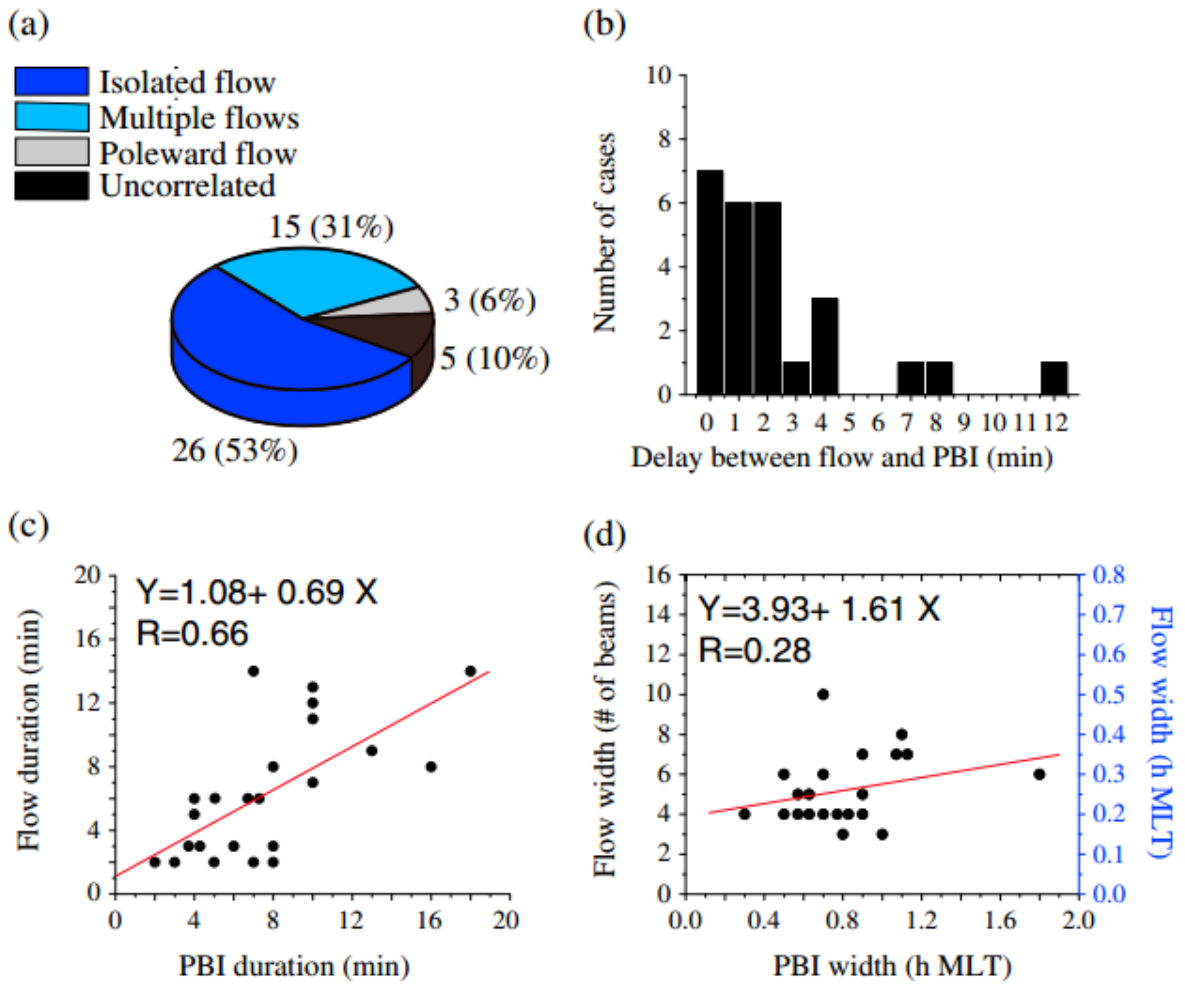

Figure 5.4 (a) Percentage of isolated intense PBIs being associated with enhanced equatorward flows. (b) Statistical time delays between the initiation of enhanced flows and PBIs. (c and d) Comparison of duration and longitudinal width of enhanced flows and PBIs, the linear fit result and correlation coefficient are also displayed. [*Zou et al.*, 2014]

the occasional high resolution data show that the flows still appeared slightly before PBIs. Figures 5.4c and 5.4d present a comparison of duration and width between flows and PBIs calculated in the same way as case studies. The linear fit result and correlation coefficient are also displayed. In Figure 5.4d we only include the cases where the polar cap flows were well captured with peaks located within the radar FOV. We can see a rough correlation of the durations of flows and PBIs and a tendency for a proportional relationship in their widths. We do not expect their widths to be highly proportional considering that PBIs only mark the field-aligned current width instead of the flow width. And as polar cap flows reach the auroral

poleward boundary, they can turn azimuthally resulting in a widened flow channel in the auroral oval.

We do not address the spatial correlation between PBIs and polar cap flows statistically here. Given the limited radar FOV, how equatorward these flows extended is uncertain, although that the flows directed equatorward to the equatorward edge of the radar FOV indicates them to be highly likely to impinge on the boundary. The longitudinal displacement between flows and PBIs is also uncertain. This is because only LOS component of flow velocity could be obtained and the missing azimuthal component can be important for estimating the precise MLT where flows contacted the poleward boundary. Nevertheless, we found that PBIs were statistically located 0.2 h MLT to the east of the flows, which is represented well by the second flow–PBI pair (marked by the red arrows) in Figure 5.2. This corresponds to a separation of ~0.9 *Re* in the y direction in the magnetotail, suggesting that PBIs and associated polar cap flows are longitudinally closed to each other.

5.4 Polar Cap Flow-PBI Association: Starting with Flows

Here we performed a reversed study to find whether isolated flow enhancements impinging on the auroral poleward boundary are also commonly related to PBI activity. Isolated polar cap flows were selected as those with quiet background-subtracted preceding flows (<200 m/s) for > ~10 min, and a step-like increase to above 200 m/s. This velocity enhancement should extend equatorward substantially (below range gate 6) so that it is likely to reach the poleward boundary. No requirements of spatial extent or duration of flows were imposed, but flows should be detected for more than two beams and two samples in order to be clearly distinguished from noise. Given these flows, we examined if new or further auroral intensifications occurred along the poleward boundary.

5.4.1 Case Study

Figure 5.5b shows the time series plot of the radar and the ASI at RANK. High temporal resolution data are available along beam 8 and shown in the third panel. Figure 5.5a displays representative 2-D snapshots of the flow-PBI association and the two pairs of association identified below are highlighted by arrows of red and orange, respectively. The flow was initially weak with an average velocity of < ~100 m/s for ~10 min. Along the auroral poleward boundary, there was an azimuthally aligned PBI that was gradually fading. At 0514 UT, a flow enhancement of >200 m/s was observed in the western part of the FOV (red arrow). However, the exact time of this enhancement has an uncertainty of ~1–2 min due to the 2 min resolution. The high resolution data in the third panel shows that the flow speed exhibited a slight and gradual increase from green (<100 m/s) to yellow (> ~ 100 m/s) during 0505–0512 UT, which was followed by an abruptly increase to >200 m/s during 0512-0513 UT. Thus the initial sign of substantial velocity enhancement was detected slightly after 0512 UT, almost 2 min before the onset time determined by the low resolution data. Almost simultaneously, a new PBI (red arrow) started to intensify. The auroral poleward boundary in this case was located at the equatorward edge of the radar FOV, and this flow was observed to extend all the way onto the boundary.

After the decay of the first flow enhancement, a second flow (orange arrow) began in the western beams of the radar at 0520 UT as seen from the low resolution data. Although the main part of this enhancement was located west of the central beam (beam 8), the high resolution data still captured the velocity increase at 0518:30 UT. Compared with the normal 2-min resolution, this provides a much more precise determination of the flow onset (~ 1.5 min earlier). Corresponding to the second flow, an even more intensified PBI (orange arrow) brightened at 0523 UT. Although unisolated flows are the not focus of this study, it also seemed to be correlated with a PBI intensification.

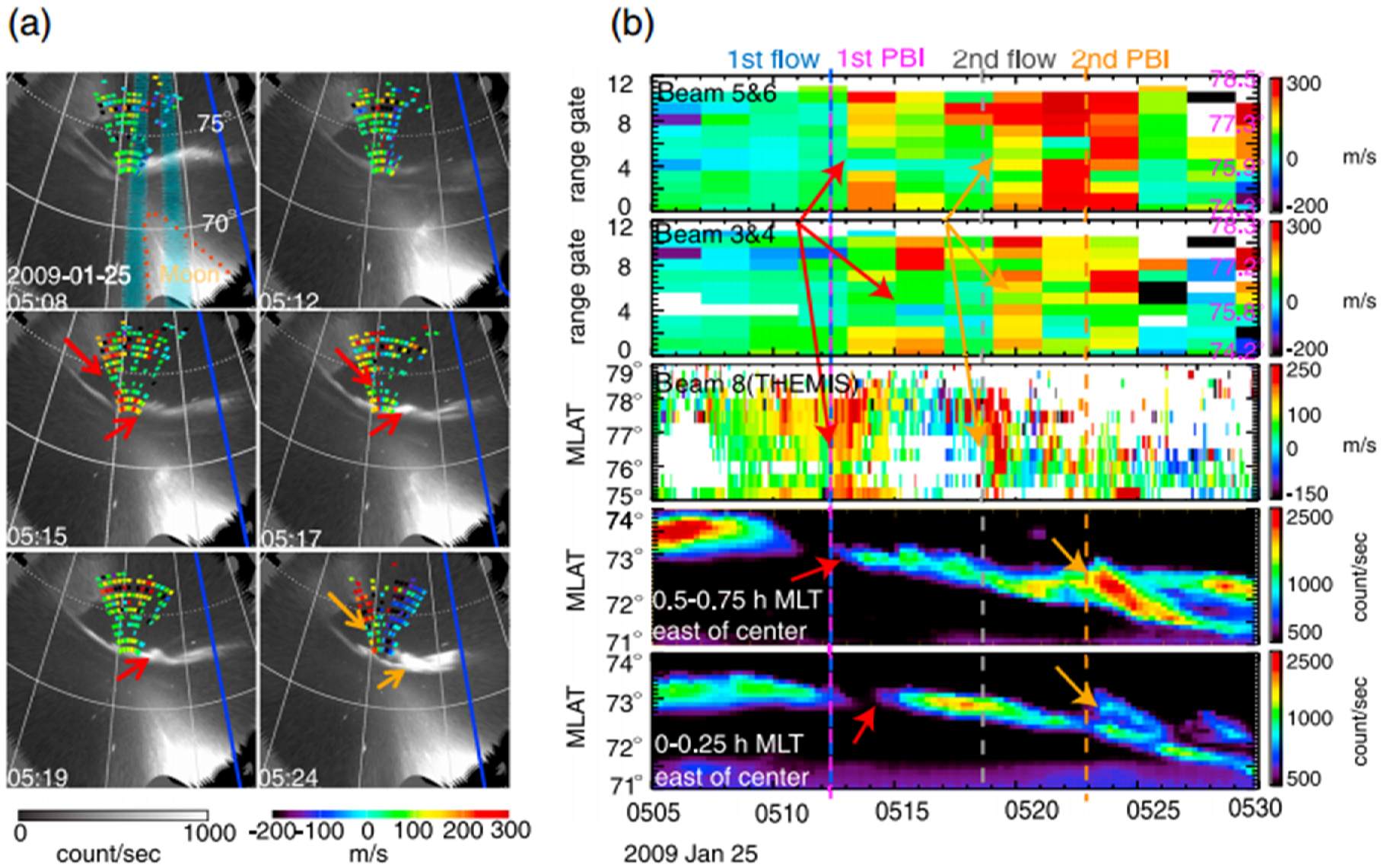
(a)
75°
70°
2009-01-25
Moon
05:08
05:12
05:15
05:17
05:19
05:24
0
1000
count/sec
-200 -100 0 100 200 300
m/s
(b)
1st flow
1st PBI
2nd flow
2nd PBI
Beam 5&6
Beam 3&4
Beam 8(THEMIS)
range gate
MLAT
m/s
count/sec
0.5-0.75 h MLT
east of center
0-0.25 h MLT
east of center
0505
0510
0515
0520
0525
0530
2009 Jan 25

Figure 5.5 (a) Selective snapshots of simultaneous observation from radar and ASI showing the flow-PBI association. Two pairs of flow-PBI association are identified and indicated as arrows of different colors. (b) Time series plot of radar and ASI observations in north-south slices. The top two panels show the average velocity of certain two beams (as marked). The third panel shows the 8 s THEMIS mode data. The bottom two panels show ASI observation. [*Zou et al.*, 2014]

5.4.2 Statistics

We selected 66 isolated enhanced polar cap flows over 4 months of data (January–April in 2009) and their correlation with auroral activity along the auroral poleward boundary is presented in Figure 5.6a. We identified 41 events (77%) that were directly associated with PBIs. Thirty-three (50%) events showed clear association with isolated PBI activity. This suggests a one-to-one correlation, and the percentage is similar to that for events selected based on PBIs (53% in Section 5.3.2). Isolated flows were also found to be related to multiple PBIs in 18 cases (27%). Those cases are still consistent with the flow-PBI association, since the occurrence of multiple PBIs often resulted from flows with equatorward flow components below our 200 m/s threshold or with poleward flows adjacent to equatorward flows lying outside the FOV. For nine cases, the flows were associated with substorms. Considering that substorms often originate from PBIs [*Nishimura et al.*, 2010a, 2010b], these flows may still correlate with PBIs that were perhaps too faint to identify due to light contaminations or were located equatorward of the FOV of RANK ASI, as sometimes occurs prior to substorm onset when the auroral oval becomes very narrow [*Nishimura et al.*, 2011]. Only six enhanced polar cap flows did not have a significant impact on observed auroral activity.

For the one-to-one correlated category, we calculated the time delay of the appearance between enhanced polar cap flows and PBIs. Similar to the statistics in Section 5.3.2, flows occurred either simultaneously with or 1–2 min earlier than PBIs. However, five cases were

found when the PBIs appeared earlier than the flows. The four of them showing a −1 min delay were within the uncertainty of radar temporal resolution, implying that they might still be consistent with the flow-PBI sequence, whereas the rest −2 min delay did display a reverse flow-PBI sequence, different from the remainder of our database.

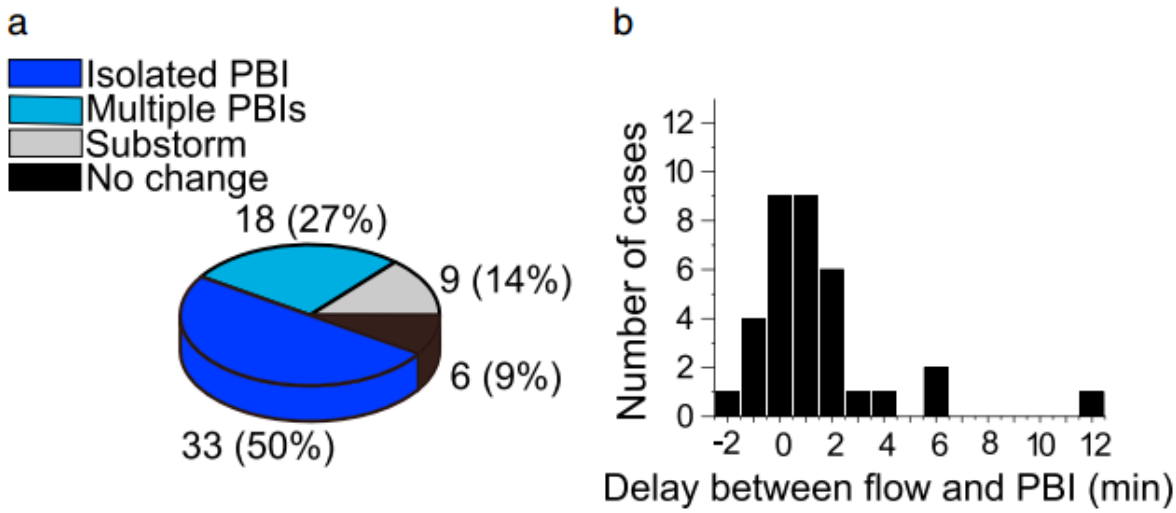

Figure 5.6 (a) Percentage of isolated enhanced equatorward flows being associated with PBI activity and (b) the statistical time delays between flows and PBIs. [*Zou et al.*, 2014]

5.5 Summary

We have investigated the relationship between enhanced polar cap flows and PBIs based on coordinated observations of the SuperDARN radar and THEMIS ASI, both located at Rankin Inlet, using case and statistical studies. We also investigated conjunction events with FAST and confirmed that the optical poleward boundary seen in the white light data well represents the poleward boundary of precipitating energetic electrons. Our case studies show a correlation in occurrence between longitudinally narrow enhanced polar cap flows that extend toward the auroral poleward boundary and PBIs. And this is found to be common in statistics. Particularly, 53% (50% for reverse study) of our cases show a one-to-one association. Flows occur simultaneously with or 1–2 min prior to PBIs. The simultaneous appearance is likely due to the low temporal resolution radar data since, based on occasional high time resolution data,

flows are detected slightly earlier than PBIs. There are rough relationships between the duration and widths of flows and PBIs.

We conclude that the occurrence of PBIs is commonly associated with enhanced polar cap flows, which are observed near and directed toward the auroral poleward boundary. Since PBIs are known to be associated with equatorward flows within the auroral oval, such association indicates that these polar cap flows traverse the auroral poleward boundary from the polar cap and enter the plasma sheet. The time delay between flows and PBIs further indicates that PBIs, and associated auroral disturbances, are likely to be driven by those mesoscale polar cap flow channels incident upon the separatrix. However, this interpretation can be biased considering that the 0-2 min delay is comparable to the Magnetosphere-Ionosphere communication time. Information on prior evolution of these flows is necessary for determine their roles in plasma sheet disturbances.

Chapter 6. 2-D Tracing of Localized Polar Cap Flow Enhancements

6.1 Event Selecting Criteria

Motivated by the close association of localized polar cap flow enhancements with PBIs, we explore tracing of flow evolution across the polar cap using airglow patches. We use coordinated observations of the Resolute Bay (RESU) ASI and SuperDARN radars at Rank Inlet (RKN) and Inuvik (INV), which are available since the winter of 2008. Here radar measurements deep in the polar cap are examined, where echoes get backscattered in the *F* region ionosphere. We focused on clear-sky conditions during ~0300–1100 UT (~2000–0400 MLT at RESU) for monitoring evolution of airglow patches in the nightside polar cap. Airglow patches were identified at 630.0 nm wavelength as ≥30 Rayleighs above background with no substantial 557.7 emissions (typically ≤50 Rayleighs). We required them to propagate into (not emerge within) the ASI FOV within ±4 h MLT from magnetic noon. We further required them to exhibit a clear and quasi-steady motion where different portions of them move consistently in a certain direction for ≥20 min and to roughly retain their shape during the propagation. This quasi-steady condition (≥20 min) excludes rapid changes in the large-scale convection pattern and selects conditions where the patch motion is likely to be influenced well by, and thus reflect, imposed localized flow structures under quasi-steady background convection. To identify the polar cap flow structures around patches, we required good LOS radar echo coverage on and adjacent to the patches for >~10 min.

6.2 Case Study

Figure 6.1 shows snapshots of coordinated observations of the RESU ASI and RKN and INV radars on 1 December 2011. The radar measurements are shown as thick and thin arrows representing merged 2-D flow vector and LOS velocity, respectively. The color and the length of the arrows indicate the flow speed, and the arrow direction with respect to each dot (for LOS) or empty square (for merged vectors) gives the flow direction. The ASI images were taken at 630.0 nm wavelength and are shown in a grey scale. The bright crescent on the dawnside is due to intense auroral emissions of the dawnside auroral oval. In these snapshots, the white lines are isocontours every 5° in magnetic latitude and every 15° longitude in AACGM Coordinates. The blue and red lines mark the midnight and noon meridian.

The airglow patch we focus on was located in the postmidnight sector of the polar cap region and was elongated in the noon-midnight direction. Collocated with this patch, as seen from the merged flow vectors (thick arrows), we can identify a longitudinally narrow flow feature having substantially larger speeds (~600–700 m/s; red arrows) than the adjacent flows (~400 m/s; green/yellow arrows), which we consider as background large-scale flows. The flow enhancement is also shown clearly in LOS measurements in Figure 6.1f as orange arrows at 79–83° MLAT on the airglow patch, surrounded by the blue and green arrows on its west and east sides. The sharp flow speed gradients well marked both edges of the patch, suggesting the flow azimuthal width to be similar to the patch width. Here the flow width was ~200 km. The width is determined by determining the full widths at half maximum of the flow velocity profiles in the direction perpendicular to the patch orientation (given by its longest dimension direction) within the flow enhancement and taking the median of these values as the width. The longitudinally narrow flow enhancement remained collocated with the patch for 16 min before the patch faded.

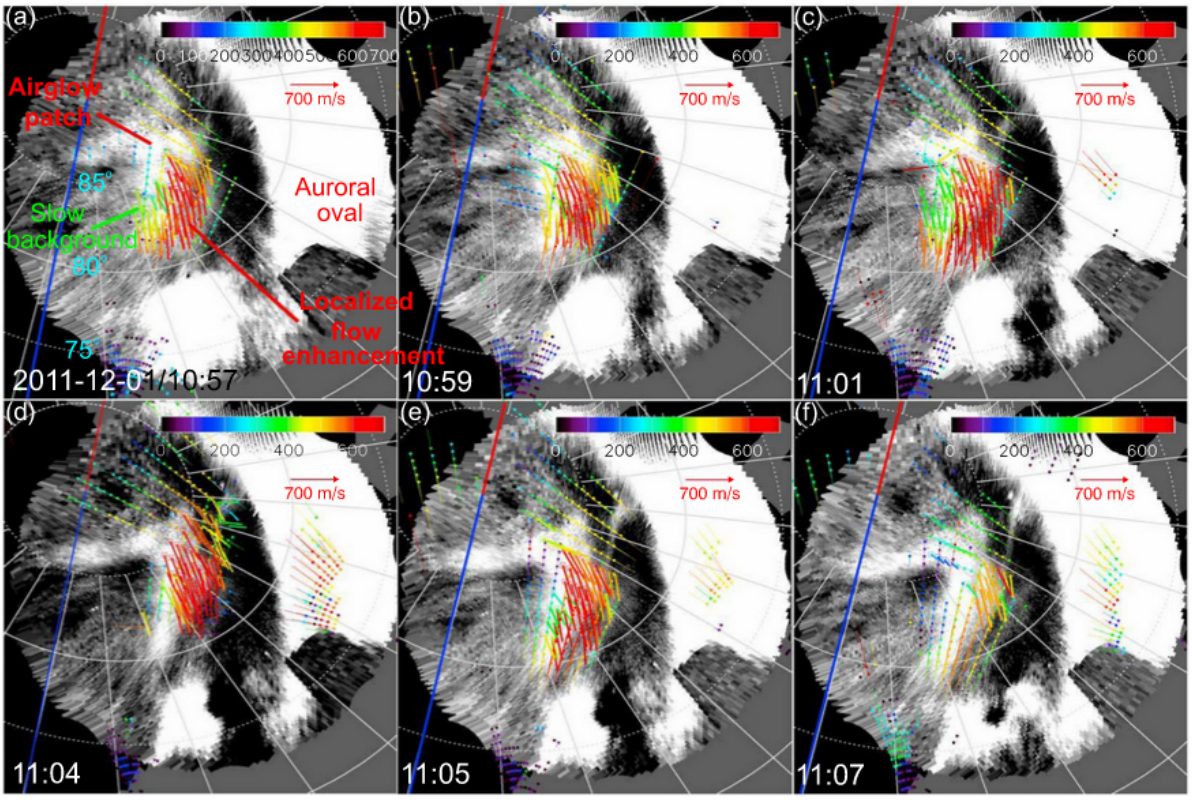

Figure 6.1 (a–f) Snapshots showing polar cap flow structures surrounding an airglow patch on 1 December 2011 based on coordinated observations of the RESU ASI and SuperDARN at RKN and INV. The radar measurements are shown as thick and thin arrows representing merged 2-D flow vectors and LOS velocity, respectively. The color and the length of the arrows indicate the flow speed, and the arrow direction with respect to each dot (for LOS) or empty square (for merge vectors) gives the flow direction. The ASI images were taken at 630.0 nm wavelength and are shown in a grey scale. The bright crescent on the dawn side is due to intense auroral emissions of the dawnside auroral oval. The localized polar cap flow enhancement and airglow patch are marked as text. [*Zou et al.*, 2015a]

The direction of the localized flow enhancement was consistent overall with the patch propagation direction, which were both mainly in the noon-midnight direction with a slight tilt toward east. We also estimated the patch propagation speed to be ~500 m/s, based on the straight-line distance between the start and end point of the patch propagation (~500 km) and propagation time (16 min). This is close to the enhanced flow speed (600–700 m/s). The straight-line assumption underestimates the actual curved trajectory, so that the actual optical speed should be closer to the flow speed.

Note that the collocation of the localized flow enhancement and the airglow patch can had an uncertainty of ~50 km, for example, as seen in Figure 6.1c. This is likely due to the different

sampling times of the radar and the optical measurements. The optical measurement has an exposure of 30 s for 630.0 nm wavelength [*Shiokawa et al.*, 1999], while the radar measurement along each beam is taken successively within 1 min as the radar antenna steers across the FOV [*Chisham et al.*, 2007]. This can also be caused by mapping uncertainties produced by projecting 630.0 nm emission onto a single height of 250 km.

Thus, this localized polar cap flow enhancement was collocated with the airglow patch and its shape, speed, and 2-D direction were well reflected by the simultaneous shape, speed, and motion of the patch. Such association was steady and persistent in time, at times persisting >1 h [Figure 3 in *Zou et al.* 2015a]. This indicates the potential for using airglow patches as an optical tracer of these flows, i.e., using radars to detect localized flows in their limited echo region and employing an ASI to infer their shape and direction in 2-D.

6.3 Statistics

We have surveyed the winter months during 2008–2012 using the criteria listed in Section 6.1 and identified 93 airglow patches. Because of the generally limited merged vector availability, we only required good coverage of LOS data from radar look directions oriented within 40° of airglow patch motion [Figure 2 in *Zou et al.* 2015a]. We can thus examine if localized flow enhancements exist in a major component of patch motion direction with a reasonable number of samples. We used LOS speeds for all statistical analysis in this section to be consistent among cases with and without merged vectors. Although we did not set any requirements on the level of geomagnetic activity, large geomagnetic storms (minimum $Dst < -50$ nT) are not present in our events because of unfavorable sky conditions or limited radar echo coverage on those days.

To define an airglow patch as being related to a substantial, localized flow enhancement, we required flow speed on the patch to be ≥200 m/s greater than the background flow outside

the patch for ≥10 min. The ≥10 min requirement ensures that the observed flow patterns are quasi-steady features. Note that we do not study all localized flow enhancements but only those seen associated with airglow patches. This is because the field-aligned irregularities of airglow patches enable strong backscatter of radar echoes, providing generally good echo coverage on flow features [*Hosokawa et al*., 2009a].

6.3.1 Occurrence and Properties of Localized Polar Cap Flow Enhancements

Figure 6.2 presents the strength of association between localized flow enhancements and airglow patches by comparing their durations in the available common FOV of the ASI and radars, which usually covers a 4–5 h MLT wide area from ~80° to 85° MLAT. Durations of patches and flows give the lengths of time when patches exhibit clear propagation and when localized flows are observed over patches, respectively. For unassociated patches, the flow duration is set to be 5 min for illustration purpose. Airglow patches with and without collocated localized flow enhancements are referred to as "associated" and "unassociated" cases, respectively. We found that 62 cases (67%) were associated with localized flow enhancements, and for the majority of them (40), the association persisted throughout most (>70%) of their propagation (dots above Y (flow duration) = 0.7 * X (patch duration)). Furthermore, for 83% of associated cases, the initial detection of flows was at about the same time as airglow patches entering the common FOV, indicating that their source region was located outside the common FOV on the dayside.

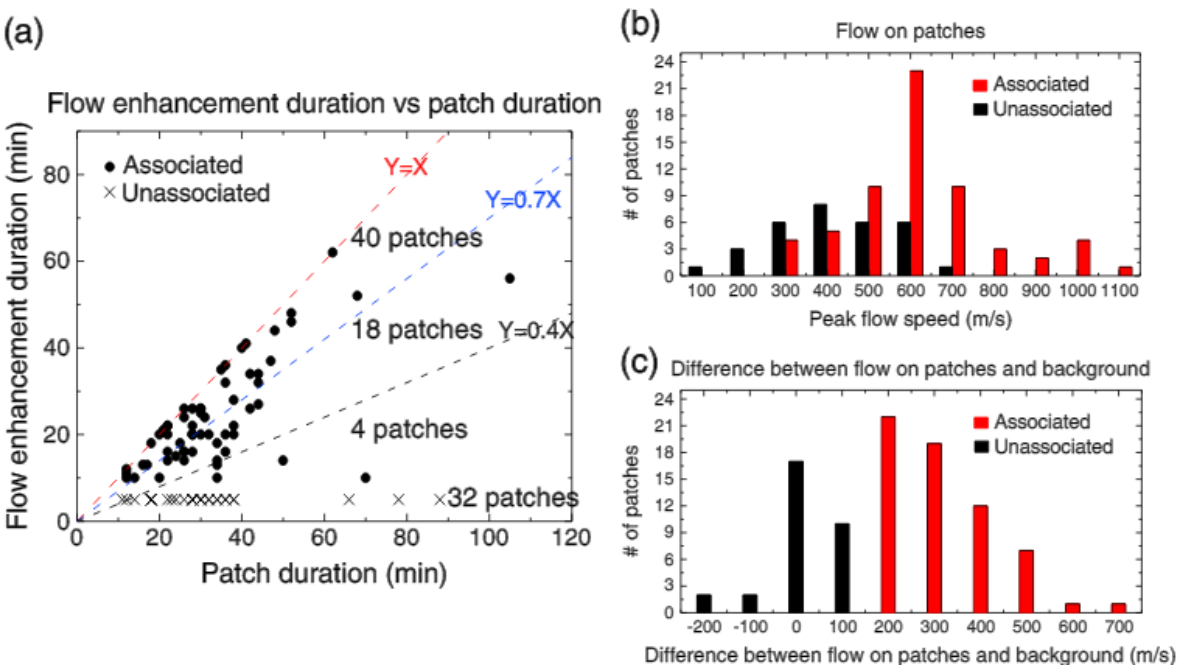

Figure 6.2 (a) Duration of localized polar cap flow enhancements versus the duration of airglow patches in the available common FOV of the ASI and radars. The dots and crosses represent the patches with and without collocated localized flow enhancements according to our definition, respectively. (b) Flow speed on airglow patches for both associated (red) and unassociated (black) cases. Each flow speed shown here is the largest 10 min running average during the time when localized flow enhancements are present (for associated cases) or during the entire patch tracing time (for unassociated cases). (c) Difference between flows on and outside airglow patches. The flow difference is averaged throughout the flow (associated cases) or airglow patch (unassociated cases) tracing. [*Zou et al.*, 2015a]

Note that in our database, localized polar cap flow enhancements either decreased to the background convection speed within the FOV (like cases $Y < 0.7\,X$) or persisted all the way to outside the FOV or to an angle unfavorable for LOS detection (like cases $Y > 0.7\,X$), with no flows lasting longer than airglow patches (no dots above $Y = X$). This is likely due to the fact that these flows can transport patches quickly to the edge of our FOV from the dayside, the transport time being shorter than the decay of enhanced electron density in patches.

Figure 6.2b compares flow speeds on airglow patches for associated (red) and unassociated (black) cases. All flow speeds have been spatially averaged across the flow enhancement and airglow patch region for associated and unassociated cases, respectively. Here they were also temporally smoothed over a 10 min running window to exclude transient (a few minutes) fluctuations, and the maximum value of the smoothed speed is presented. The

flow speed on unassociated airglow patches had a broad distribution varying from 200 to 600 m/s with a peak at 400 m/s, which is about the typical speed of large-scale polar cap convection under moderate IMF conditions [*MacDougall and Jayachandran*, 2001]. On the other hand, the speed of associated cases was statistically larger with a narrow peak at 600 m/s and reaching 1000 m/s for a few cases. This difference suggests that airglow patches can either follow the slow large-scale convection (unassociated cases) or localized flow enhancements (associated cases), depending on whether localized flows are present. Figure 6.2c gives the difference between flows on and adjacent to (regarded as background convection) airglow patches averaged within the flow (associated cases) or patch (unassociated cases) duration. The flows on and outside the unassociated airglow patches were about the same, while for associated cases the flow difference was mostly 200–300 m/s. Although the LOS flow speeds shown here are smaller than the actual 2-D velocity, they should be representative of the actual flow feature considering our selection of LOS components along the major component of the patch motion.

Figure 6.3a shows length of time (duration) that we observe localized flow enhancements as a function of time-averaged flow speed, based on cases where they traveled a similar distance (a straight line distance of 800–900 km) within our FOV. The duration follows that expected for the plasma to move across the radar FOV with the average flow speed on the patch (blue curve). The approximation from using straight line distance and LOS velocity leads to some of the scatter of the observed durations relative to that expected.

Figure 6.3b shows the width of localized flow enhancements as a function of flow speed. The flow width and speed were taken when radar coverage was occasionally sufficient to capture the slow background flows on both sides of the flow enhancements. This panel does not show a clear speed dependence (correlation coefficient being 0.26), and the flow width was

typically about 200–300 km. However, this result is limited by the available radar coverage and may thus bias to flows with narrow widths.

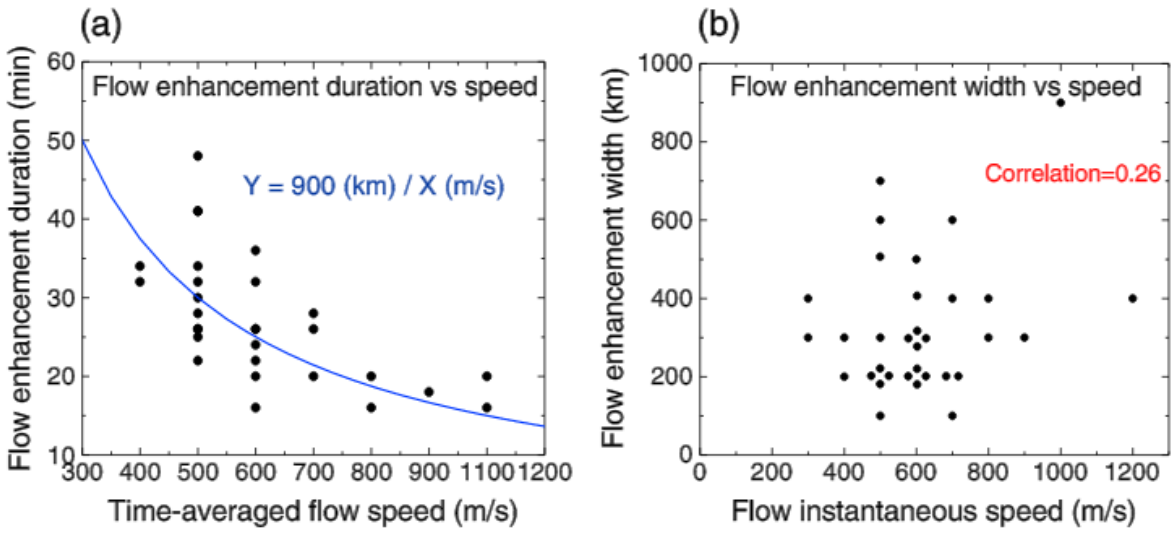

Figure 6.3 (a) Duration of localized flow enhancements across our tracing area as a function of average flow speed. The cases included here are those where airglow patches and associated localized flow enhancements traveled a similar distance (800–900 km) across the radar FOV. (b) Width of localized flow enhancements as a function of flow speed. The cases included here have sufficiently large radar coverage to capture the slow background flows on both sides of the flow enhancements. [*Zou et al.*, 2015a]

6.3.2 IMF Dependences of Localized Polar Cap Flow Enhancements

To obtain general information on localized flow enhancement origin and propagation processes, we explored dependences of the flow's occurrence and properties on IMF conditions using the associated events described above. We used the OMNI 1 min resolution IMF from 2 h before the start of our tracing until the end of the tracing to account for the history of flow evolution all the way from the dayside to our FOV in the nightside polar cap. The 2 h length is a rough estimate based on the curvilinear travel from the possible dayside source region at ~75° to the poleward edge of our tracing area (~85° in the nightside) with a speed at 600 m/s, with

the inclusion of some important IMF conditions preceding the flow formation. We also experimented using 1 h or one and a half hour; similar results are obtained.

The flow occurrence shows distinct dependence on IMF clock angle as follows. Clock angle is the angle between GSM north and the projection of the IMF vector onto the GSM *y*-*z* plane and is determined as the arctangent of B_y/B_z. Figure 6.4 presents the IMF clock angle variation for each event, divided into three different categories of variation over time: quasi-steady, oscillating, and turning. Quasi-steady IMF clock angle (Figures 6.4a and 6.4d) events varied within a ±30° range from the average of each case except for brief (≤30 min, i.e., <25% of the interested interval) excursions. Oscillating IMF (Figures 6.4b and 6.4e) events exhibited large variations (>30°) for >30 min that oscillated or appeared randomly distributed for most times. These variations are still considered slow because of their long periodicity (~1 h). Turning IMF events (Figures 6.4c and 6.4f) showed only a large clock angle shift (>30°) from one component ($\pm B_y$ or $\pm B_z$) dominated regime to another. One example showing the shift from $+B_y$ to $-B_z$ dominance is illustrated in red.

This categorization enables rough evaluation of the reliability of using median IMF clock angles to represent the overall IMF behavior within our interested interval. Medians from oscillating and turning categories are less representative than those from quasi-steady category because of the large IMF variations. Especially for turning cases, a median value may be biased to one of the IMF states in each case. To limit this uncertain bias, we took the median value of the first hour in turning cases, instead of the entire interested interval, focusing on the flow generation process. Despite the possibly large uncertainties, oscillating and turning cases only constitute a small portion of our database and thus will not influence the overall clock angle distribution significantly.

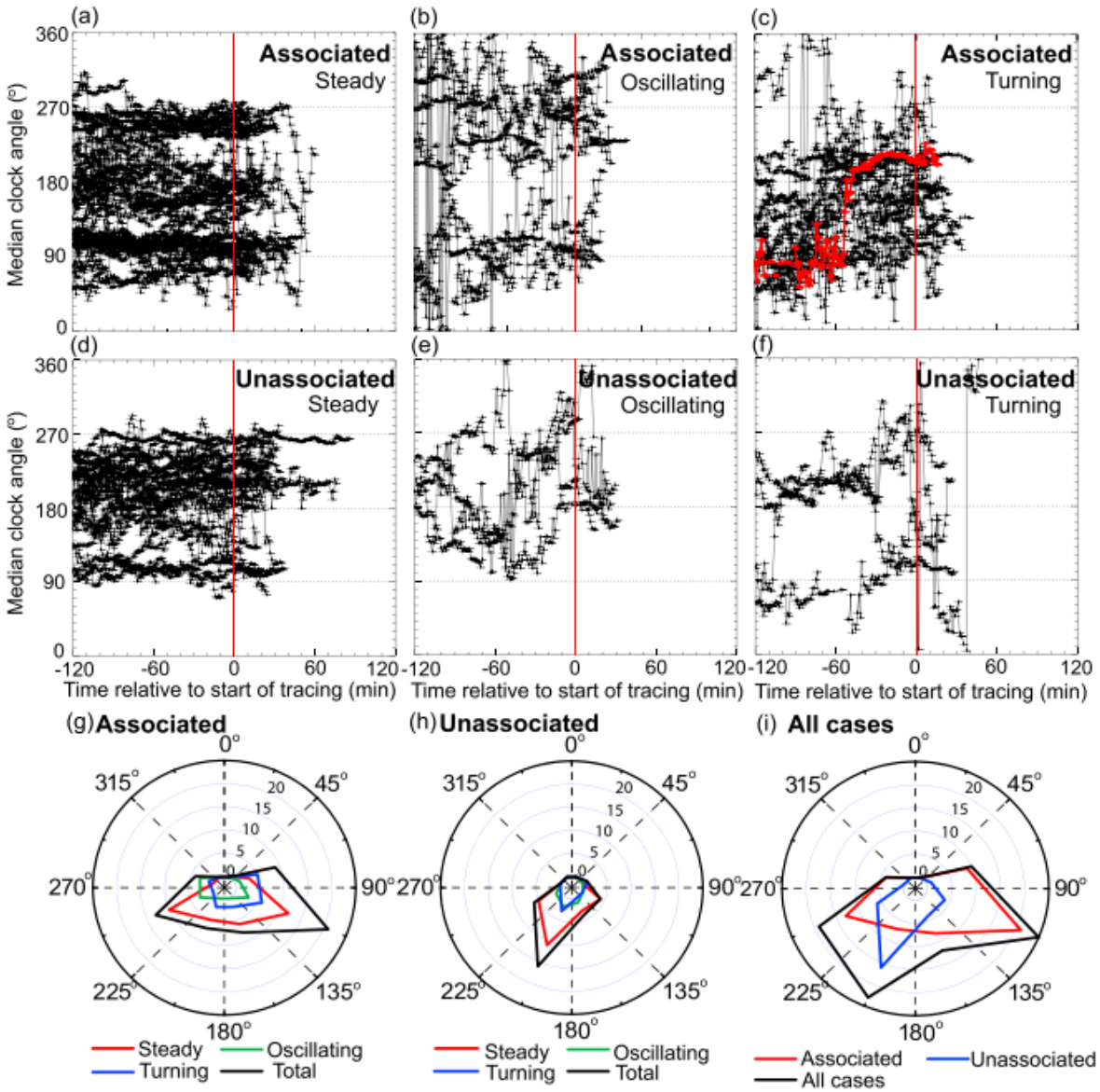

Figure 6.4 (first two rows) Superposed IMF clock angles since 2 h before the start of our tracing until the end of the tracing for associated and unassociated cases. Events are divided into three categories based on the steadiness of clock angles: quasi-steady, oscillating, and turning. (bottom row) Diagram of median IMF clock angle distribution for (g) associated, (h) unassociated cases, and (i) the sum of them. Radial axis shows the number of airglow patches, and its labels are marked in the figure. Values from different categories are shown in different colors. [*Zou et al.*, 2015a]

Figure 6.4g shows that the quasi-steady cases (red) of associated events were mostly observed under southward IMF, and they occurred more frequently under $\pm B_y$-dominant IMF ($90° < \theta_{clock} < 135°$ and $225° < \theta_{clock} < 275°$) than $-B_z$-dominant IMF ($135° < \theta_{clock} < 225°$). The same $\pm B_y$ preference is also clear for oscillating cases (green), except without a discernible B_z dependence. Turning cases (blue) favored $+B_y$. The sum of three categories

(black) of associated cases suggests that localized polar cap flow enhancements were most likely to be observed under $\pm B_y$-dominated IMF with a slight bias toward $+B_y$ over $-B_y$ and for $-B_z$ over $+B_z$. Interestingly, $-B_z$ with a slight $-B_y$ gives the highest probability for airglow patches propagating with the background convection without a localized flow enhancement, as seen in Figure 6.4h for all the three categories. Such an IMF orientation has been found to give a symmetric two-cell convection pattern (see Figure 5 of *Ruohoniemi and Greenwald* [2005]).

The comparison of all cases with the associated and unassociated categories is shown in Figure 6.4i. Besides the different clock angle preferences discussed above, it is also noteworthy that the clock angle distribution of the sum of two categories resembles that of dayside PMAFs found by *Xing et al*. [2012], consistent with PMAFs and associated flows being the source of airglow patches and their commonly associated polar cap flow enhancements.

Similar to our findings on localized polar cap flow enhancements, the IMF clock angle has also been found to lead to distinctly different auroral configurations on the dayside. *Sandholt et al*. [2004] found that B_y-dominated IMF leads to intense PMAF activity, while a weaker and more latitudinally restricted but longitudinally wide auroral band was observed under $-B_z$-dominated IMF. The difference in PMAF behaviors suggests different flow structures associated with them, which may account for the IMF clock dependences of flow features in the nightside polar cap.

Figure 6.5 shows the average speed of localized polar cap flow enhancements during our tracing versus IMF clock angle. Quasi-steady clock angles leaded to moderately fast flows whose speed varied from 300 to 700 m/s with a peak occurrence at 500–600 m/s. The oscillating clock angle category contained very fast flows reaching 800–1000 m/s. There were also flows with moderately large speed, as green dots between 500 and 700 m/s, but no flows below 500 m/s, resulting in generally larger speeds than those under quasi-steady conditions. Flows in turning cases exhibited a variety of velocities, from 300 to 900 m/s.

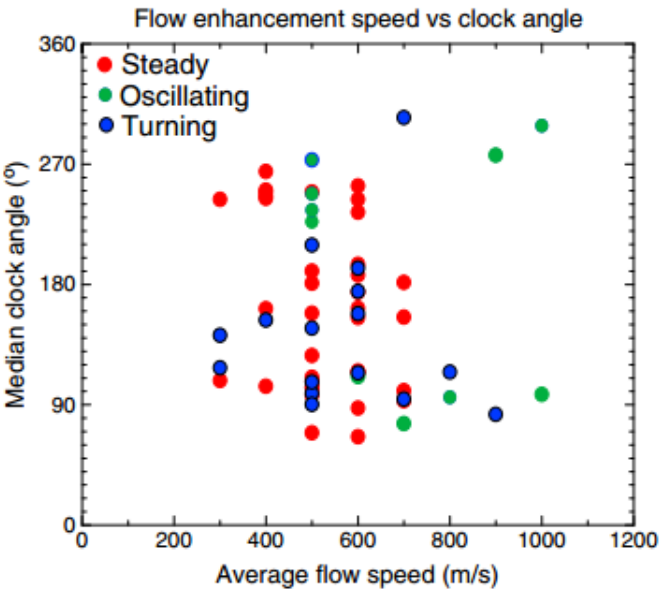

Figure 6.5 Speed of localized polar cap flow enhancements versus IMF clock angles. The speed shown is averaged during our tracing of flow enhancements, and the dots of red, green, and blue correspond to the cases from quasi-steady, oscillating, and turning categories. [*Zou et al.*, 2015a]

Besides flow speed, the averaged orientation and direction of localized flow enhancements were also examined as a function of IMF clock angle as shown in Figures 6.6a and 6.6c. Localized flow enhancements appear as channels, and the tilt of these channels from the noon-midnight direction is defined as orientation. The flow channel orientation was derived from airglow patch orientation considering that patches correspond to regions of flow enhancement. On the other hand, flow directions were determined through merged vectors if available or through propagation direction of airglow patches, which were both temporally averaged to reflect the flow/patch representative evolution throughout our tracing. For comparison, similar features were also measured among unassociated cases although these patches were not associated with localized flow features (Figures 6.6b and 6.6d). The sign of angles are defined as illustrated in the figure.

As shown in Figure 6.6a, under quasi-steadily $\pm B_y$-dominated IMFs (red dots), the common IMF condition for associated cases, airglow patches and associated flow enhancements tended to be elongated along (<60° or >120°) the noon-midnight meridian. Deviation from this meridian became significant as the relative contribution of $-B_z$ increases, suggesting a trend of increasing flow enhancement orientation angles with respect to the IMF clock angles, as seen from the linear fitted result. Oscillating cases (green dots) generally

showed a similar distribution except for two dots (around (0, 300) and (170, 80), marked by black arrows). These two dots were still consistent with the trend of red dots considering the symmetry at 0 and 180°. The turning cases (blue dots) showed large scattering, probably because their median clock angles were not representative for the entire flow evolution. This suggests that flow enhancements tend to be observed as a channel that is elongated in the noon-midnight meridian and the deviation from this meridian increases as the B_z contribution increases.

Figure 6.6b shows the airglow patch orientation when no localized flow structures were present. Compared with associated events, unassociated category had more cases occurring under $-B_z$-dominated IMF and the patches there were elongated closer to the dawn-dusk direction, with orientations between 60° and 130°. Their orientation angles also increased with the IMF clock angles, and this trend resembles that for associated cases with ~10% difference in fitted results.

Figure 6.6c shows the direction of patch-associated localized polar cap flow enhancements, as a function of IMF clock angles. For all three categories, the flow directions show clear IMF dependence, pointing toward dusk (dawn) for $+B_y$ ($-B_y$) dominated IMF. Similar B_y dependence can also be found for unassociated cases (Figure 6.6d). However, flows from the majority of associated cases were directed with an angle (clustered around −30°) from the noon-midnight meridian, while unassociated cases showed a more parallel (clustered at ~0–10°) direction, which is a result of the strong IMF B_y and B_z contributions, respectively. Comparing the fitting results from the two categories suggests that given same clock angles, flow directions on associated patches are more parallel to noon-midnight meridian than those on unassociated ones, as a result of a larger antisunward flow component of localized flow enhancement than the background as seen in Section 6.2.

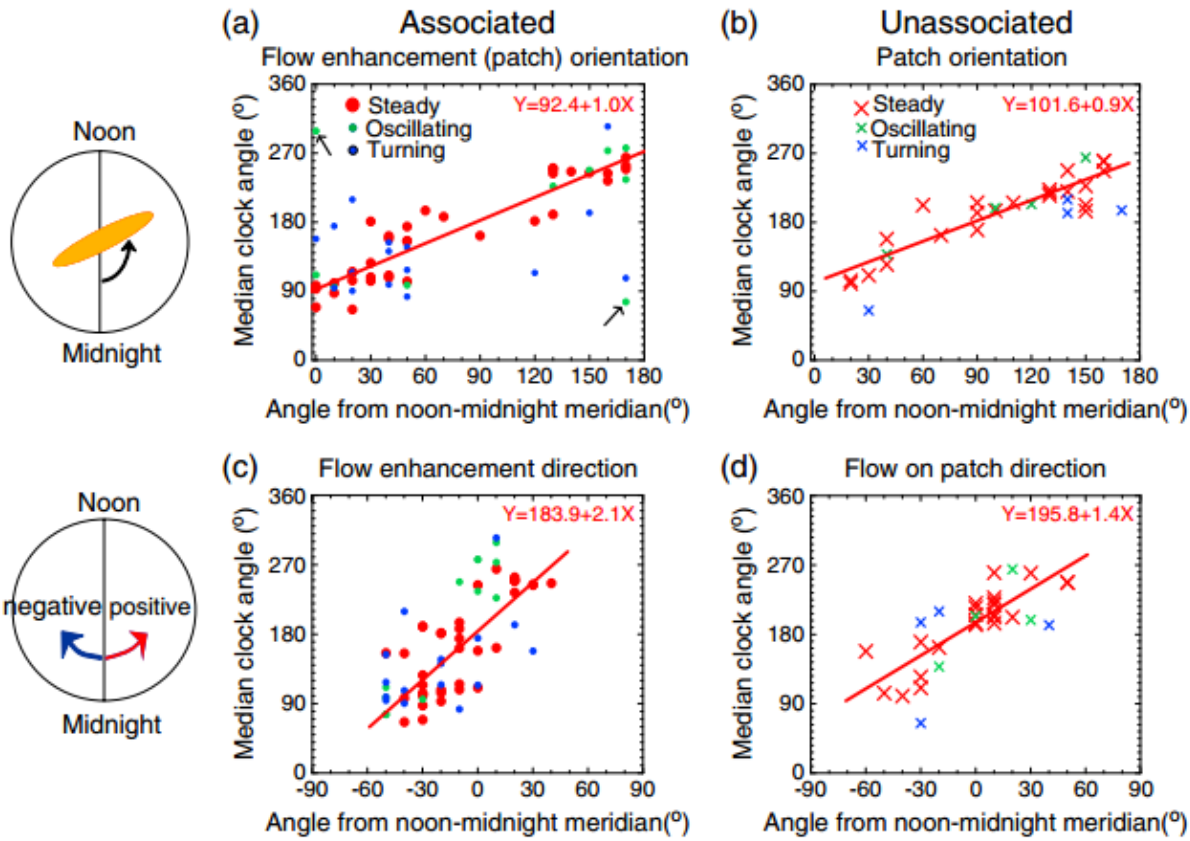

Figure 6.6 Orientations and propagation directions of airglow patches and associated flows for (a and c) associated and (b and d) unassociated cases. Angles are of 10° resolution. The orientation angle varies from 0° to 180° relative to the noon-midnight meridian in an anticlockwise direction. The propagation direction is defined to be positive toward dawn and negative toward dusk, varying from −90° to 90°. The dots and crosses of red, green, and blue represent the cases in quasi-steady, oscillating, and turning categories. The red dots and crosses are plotted in a larger size owing to their steadiness of the IMF and are linearly fitted. [*Zou et al.*, 2015a]

The flow direction dependence on IMF is consistent with *Hosokawa et al*. [2009b], who showed that the drift velocity of airglow patches is directed toward dusk (dawn) when the IMF B_y is positive (negative). However, their determination of the 2-D airglow motion is based on cross-correlation analysis over a fixed window at zenith between consecutive images. Therefore, their patch velocity reflects instantaneous velocity near the zenith and can be averaged with the background velocity if both are present in the window.

6.4 Contribution of Localized Polar Cap Flow Enhancements to Convection

To estimate the contribution of localized polar cap flow enhancements to the total convection across the dawn-dusk meridian, we performed a simple calculation of the potential drop across the flow enhancement and its ratio to cross polar cap potential. The meso potential was calculated as the product of magnetic field at 250 km altitude, flow speed, and flow width. The cross polar cap potential was taken from the convection maps available on the SuperDARN website http://vt.superdarn.org/ at Virginia Tech [*Ruohoniemi and Baker*, 1998]. Calculations were performed for the case studies in *Zou et al.* [2015a], and the inputs and results are shown in Table 1.

Table 1. Potential Drops Across the Flow Enhancements and Their Ratio to Cross Polar Cap Potentials for Events in Section 3[a]

	Φpc (kV)	Flow Speed (m/s)	Flow Width (km)	Flow Potential (kV)	%
1-12-2011/10:54–11:08	48	600	200	6.6	14
23-2-2009/07:44–07:53	45	900	200	9.9	22
4-3-2011/04:55–05:08	53	700	100	3.85	7
5-11-2011/08:20–09:02	48	600	300	9.9	21
27-11-2011/06:20–07:11	53	500	300	8.25	16
25-2-2012/05:47–06:27	49	500	600	16.5	34
18-11-2012/07:16–07:50	46	800	400	17.6	38
5-3-2010/07:06	41	800	300	13.2	32

[a]Columns from left to right are the time of the event, averaged cross polar cap potential, averaged flow enhancement speed, representative flow enhancement width, calculated flow enhancement potential, and its ratio to cross polar cap potential.

We used the time-averaged cross polar cap potential and flow enhancement speed during our flow tracing interval, and the flow width when echoes coverage was sufficiently large, so that the mesoscale potential and its ratio were representative throughout our tracing. However, for the case in the bottom row, the localized flow enhancement exhibited large variations during its evolution and an instantaneous potential was calculated instead. Depending on the flow speed and width, the potentials of the eight localized flow enhancements varied from a few to more than 10 kV, and this magnitude accounted for ~10–40% of the cross polar cap potential.

Such a contribution by each patch is substantial considering their narrow width. Since multiple patches in the polar cap may all be related to localized flow enhancements, these flow structures may even become the dominant transportation process in the polar cap.

This transport by localized polar cap flow enhancements is similar to that of narrow flow channels in the plasma sheet, i.e., BBFs, which have been shown to be responsible for >30% of the total earthward transportation in the plasma sheet [*Angelopoulos et al*., 1994] and up to 60–100% when BBF occurrence maximizes. These numbers are obtained by calculating the ratio of the y component of electric field when BBFs were observed by the satellites to the whole sampling time. Despite the differences in calculating methods, the comparable values suggest that localized flow enhancements in polar cap can transport large amount of magnetic flux, just as BBFs do in the plasma sheet.

This transport by localized flow enhancements deep in the polar cap (~10 kV) is also comparable to that of dayside disturbances associated with magnetic reconnections. *Lockwood et al*. [1993] estimated the convection contribution of a PMAF to be 10–60 kV, depending on the specific altitudinal profile of the emitted 630.0 emission. *Elphic et al*. [1990] found the potential across an ionospheric flow burst at the dayside cusp in conjunction of an FTE to be >~10 kV. Based on satellite observation, *Newell and Sibeck* [1993] inferred the FTE potential to be <~10 kV. The consistency in contribution to convection across the polar cap and the dayside cusp suggests that the localized flow enhancements we observe may originate from dayside reconnection and propagate all the way deep into the nightside polar cap.

6.5 Summary

Motivated by the important connections of localized polar cap flow enhancements to nightside auroral activity, we combine measurements of SuperDARN with the Resolute Bay ASI to examine the feasibility of studying these flow features with airglow patches being their

optical tracers. We also statistically investigate the properties of flow enhancements that are associated with airglow patches, their IMF dependence, and contribution to polar cap convection.

Our case studies show narrow flow enhancements collocated with airglow patches of similar longitudinal widths. The flow direction and speed are consistent with the airglow patch motion. Such association is found to be common (67%) in statistics. And it is common for these flows to persist almost throughout (>70%) the airglow patch evolution.

The associated flows tend to propagate at a speed of 600 m/s, and their speed is usually 200–300 m/s above the background. The flow duration within the radar FOV is as expected from the time it takes the plasma to move across the radar FOV with the average flow speed on the patch. The azimuthal flow width, however, is not velocity dependent and can vary from 100 to 900 km with a peak occurrence at 200–300 km.

We also explore the IMF conditions that are possibly responsible for localized polar cap flow enhancements. Our cases occur mostly under $\pm B_y$-dominated, but southward, IMF, with a slight bias toward $+B_y$ over $-B_y$. Occurrence under $-B_z$-dominated IMF is much lower. In contrast, when localized flows are not identified over patches, the preferential IMF condition is $-B_z$-dominated, indicating that the patches are being carried by large-scale convection. The sum of the two distributions resembles the clock angle dependence of dayside PMAFs [*Xing et al.*, 2012], suggesting that PMAFs, as well as the associated fast flow bursts, may be the source of localized flow enhancements in the polar cap. Also, our flows' preference to $\pm B_y$ may be related to the different PMAF behaviors that have been observed as a function of IMF clock angles.

Speeds of localized flow enhancements are generally larger when IMF clock angles exhibit large oscillations than when they stay quasi-steady. Flow orientations, as inferred from airglow patch orientations, are mostly directed quasi-parallel to the noon-midnight meridian

and turn toward azimuthally as the relative contribution of B_z increases. The flow directions well agree with the polarity of B_y, directing toward dusk (dawn) for positive (negative) B_y, consistent with the tilt of background large-scale two-cell convection [*Ruohoniemi and Greenwald*, 2005].

Electric potentials across localized flow enhancements vary from a few to more than 10 kV and can account for ~10–40% of the cross polar cap potential. Such contribution is substantial and may even become predominant if multiple patches propagate in the polar cap and are all related to localized fast flows

Chapter 7. 2-D Flow Impact on Nightside Auroral Oval

7.1 Event Selecting Criteria

Optical flow tracing enables us to trace flow evolution over broad region and in 2-D, and thus promotes the study of the impact of localized polar cap flow enhancement on the nightside auroral oval. We utilize coordinated observations of multispectral (including 630.0 and 577.7 nm) and white light ASIs and SuperDARN radars that have been available since 2008. We have surveyed the northern winter months (Oct-Dec and Jan- Mar) from 2008 to early 2013 and focused on clear sky conditions during 0300-1100 UT (2000-0400 MLT at RESU). The polar cap was identified as an area poleward of the auroral oval (~<110 Rayleigh except for polar cap arcs and patches [*Blanchard et al.*, 1997]). Polar cap arcs were selected as discrete and intense 557.7 nm emissions (>100 Rayleigh), which clearly differentiate arcs from airglow patches. Disturbances in the nightside auroral oval were not required to be seen when searching events, but were identified later if they occurred within ±10-20 min and ~1-2 h MLT from the time and location of the arc contacted with the auroral oval. Although good radar echo coverage was not required for every case due to the already known association of arcs and flows, we used available echo region around an arc to validate existence of a localized, isolated fast flow parallel to the arc (~>a few hundred m/s above flows in other area). We focused on arcs and associated flow channels that were deep in the polar cap (widest separation being >1000 km from the auroral oval) and were isolated and quasi-steadily propagating for >~ 1h, transient and dynamic activity being excluded to avoid finding coincidental events.

7.2 Case Study

We identified three types of auroral oval disturbances that occurred in response to polar cap arcs. The auroral oval in the first type exhibited distinct auroral arc systems at its poleward and equatorward portions, while the following two types had only a single arc. The poleward boundary activity may have been either undetectably small or located so close to the equatorward arc that it cannot be optically resolved. These two categories of auroral ovals are referred as thick and thin ovals, respectively. Note that the term does not necessarily reflect the absolute latitudinal thickness, and even the thick oval is still confined in latitude due to the quiet geomagnetic conditions of polar cap arcs. Here we present two cases, one being in a thick oval, the other one being poleward-expanding intensification within a thin oval. The third type of response can be found in *Zou et al.* [2015b]

7.2.1 Thick Oval: PBI

Figure 7.1 presents a sequence of the 630.0 nm snapshots where the polar cap arc was found to be associated with PBI activity within a thick auroral oval on Feb 6, 2013. White lines are isocontours every 5° in magnetic latitude and every 15° longitude in AACGM coordinates. The blue and red lines mark the midnight and noon meridians. A running median intensity over 2 h has been subtracted to enhance the emission contrast to the background, except for Figure 7.1a. Figure 7.1a shows absolute intensity and retains the faint and continuous emission from the nightside auroral oval, and the poleward boundary of the oval is identified by the dashed light blue curve. LOS radar flow measurements from SuperDARN at RKN station are also shown.

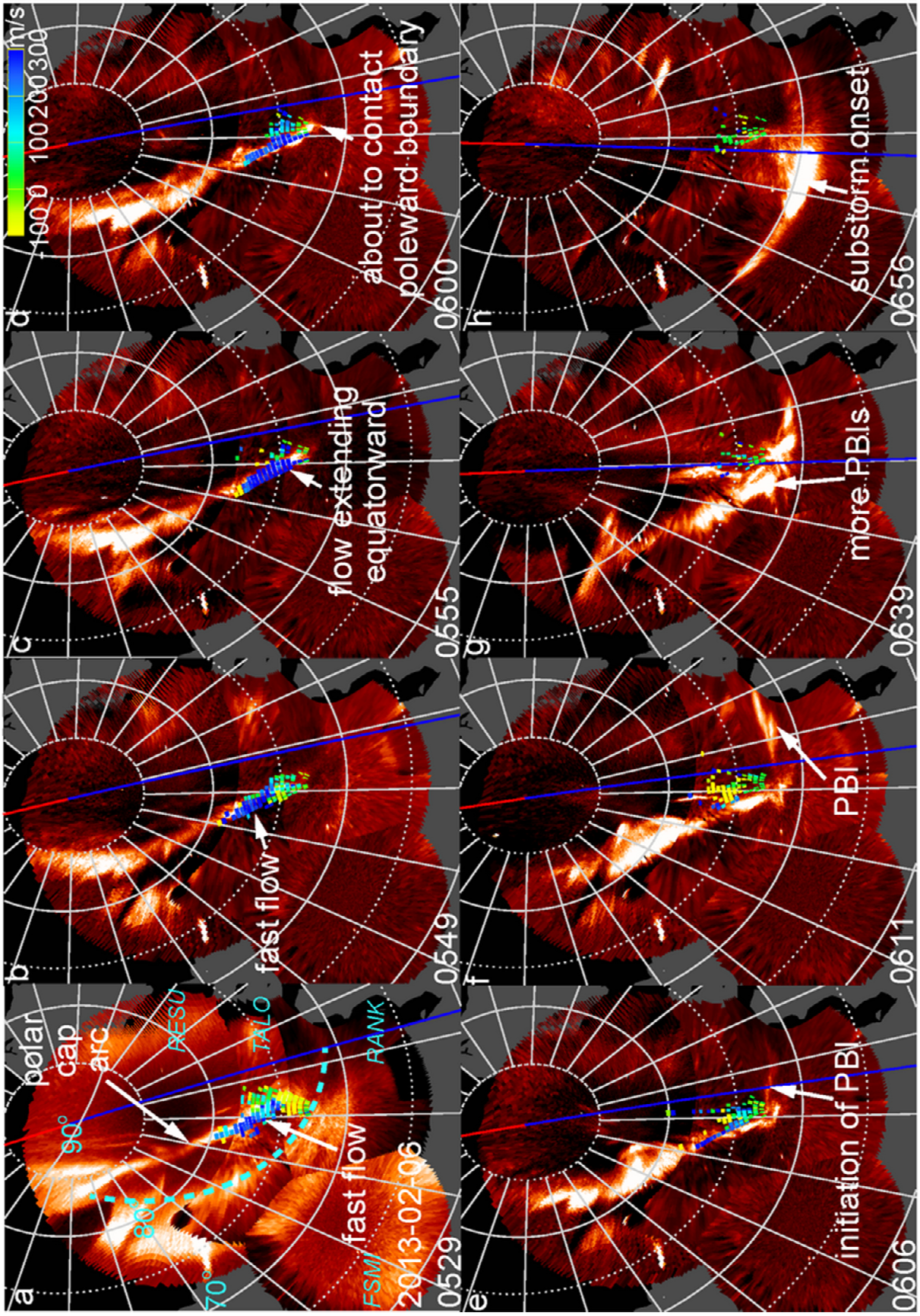
a
polar cap arc
90°
80°
70°
RESU
TALO
RANK
FSM
fast flow
2013-02-06
0529
b
fast flow
0549
c
flow extending equatorward
0555
d
-100 0 100 200 300 m/s
about to contact poleward boundary
0600
e
initiation of PBI
0606
f
PBI
0611
g
more PBIs
0639
h
substorm onset
0656

Figure 7.1 630.0 nm snapshots showing the association of a polar cap arc to PBI activity within a thick auroral oval on Feb 6, 2013. White lines are isocontours every 5° in magnetic latitude and every 15° longitude in AACGM Coordinates. The blue and red lines mark the midnight and noon meridian. A running median intensity over 2 h has been subtracted except for Figure 7.1a. Figure 7.1a shows absolute intensity and retains the faint and continuous emission from the nightside auroral oval, and the poleward boundary of the oval is marked as the dashed light blue curve. Radar data (0-20 range gates) from SuperDARN at RKN station are also shown. [*Zou et al.*, 2015b]

A polar cap arc within the RESU imager FOV slowly drifted duskward and equatorward for ~ 2 h. This is not the auroral poleward boundary because there was no emission on either side of the arc, and it extended to near the magnetic pole. This arc was spatially aligned with a longitudinally narrow flow enhancement (dark blue colored flow data point), and, as it extended equatorward, the flow also penetrated from ~76° to ~74° MLAT towards the auroral poleward boundary (Figure 7.1b and 7.1c). The flow observations showed a sharp azimuthal gradient in velocity along the dawnside edge of the flow (Figures 7.1b-d). Along the flow's duskside edge and thus beyond the radar FOV, a gradient is also expected to exist as is required to give the upward field-aligned currents associated with the arc. Therefore this was not an enhancement in two-cell convection but a localized flow feature associated with the arc, although only a portion of the flow was captured here. Its LOS speed was ~300 m/s, ~200 m/s larger than in the surrounding region. This speed underestimated the full $\mathbf{E} \times \mathbf{B}$ drift because the radar echoes here were from short-range backscatter near the radar and were thus from the E-region, where flow speed is limited to below the ion acoustic speed (~400 m/s) [*Haldoupis*, 1989; *Koustov et al.*, 2005]. The width and speed of the flow agree with those identified by using radar observations only [*Nishimura et al.*, 2010; *Zou et al.,* 2015], indicating that they are of the same phenomena identified with different approaches.

The correspondences on location and motion between the polar cap arc and the localized flow enhancement enable flow tracing beyond the radar FOV. The arc (and hence flow aligned with it) existed deep in the polar cap long before it propagated equatorward into the radar FOV. It extended further equatorward of the radar FOV in the direction marked by the arc and

impinged on the auroral poleward boundary at 0600 UT and at ~333° MLON, as determined from the visual contact of the arc with the poleward boundary (Figure 7.1d).

Just to the east of the polar cap arc, an oval intensification initiated (Figure 7.1e). This was the only major oval disturbance within our FOV and within the ~ 1 h interval before the contact of the polar cap arc with the oval. It appeared as the most poleward intensification located along the auroral poleward boundary, i.e. a PBI, and its western edge was attached to the arc. The direct spatial connection and proximity in time and space indicate that this PBI was not coincidental but closely related to the arc. In particular, the spatial connection suggests a traversal of the localized polar cap flow lying adjacent to the arc across the open-closed field line boundary, and directly linking to a fast flow channel in the auroral oval and plasma sheet. This PBI then intensified and drifted eastward out of the imager FOV (Figure 7.1e).

The polar cap arc subsequently remained in contact with the nightside auroral oval, and more PBIs formed around the contact longitude (Figure 7.1g) until the arc faded away ~1 h later. During this time, small auroral filaments also developed in the polar cap to the east of the preexisting arc. Although these transient structures are not the focus of this study, they may relate to the multiple field-aligned currents developed around an arc predicted by *Zhu et al.* [1993]. In the meantime, an arc formed along the equatorward boundary of the auroral oval, and the PBIs extended southward towards the equatorward arc. At the same longitude, a subsequent substorm-like brightening occurred along the equatorward arc (Figure 7.1h).

Figure 7.2 shows the time series plots of this event. From top to bottom, it presents OMNI IMF, 630.0 nm keograms integrated over all meridians of RESU and RANK, flow measurement by the RKN radar, 630.0 nm keograms from the PBI meridians from RANK and all meridians of FSMI, and magnetometer data from RANK. The polar cap arc–PBI–substorm onset sequence can be identified and is marked by the solid pink curve. Plots as in Figure 7.2 enable us to quantify the temporal relation between the contact of polar cap arcs on

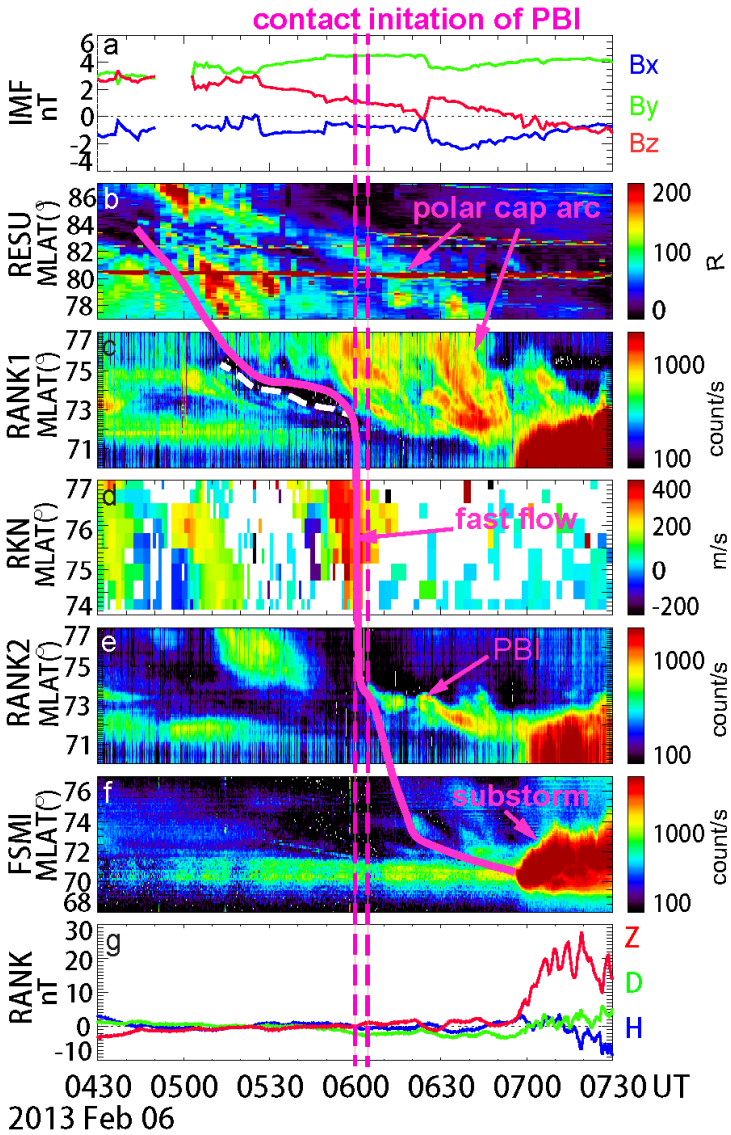

Figure 7.2 Time series showing the association of the polar cap arc to PBI activity shown in Figure 1. From top to bottom: OMNI IMF, 630.0 nm observation of the polar cap arc from RESU and RANK, flow measurement by RKN radar along beam 1, 630.0 observation of the auroral oval activity from RANK and FSMI, and magnetometer data from RANK. The 630.0 nm keograms integrate emissions from almost the entire longitudinal range of the images except for Figure 2e which centered at the PBI longitude. The polar cap arc – fast flow – PBI – substorm onset sequence is shown as solid pink curve. The dashed white curve marks the auroral poleward boundary. [*Zou et al.*, 2015b]

the auroral oval and the associated oval disturbances. The contact time (first vertical dashed pink line) was identified as the time of closing of the latitudinal gap between emissions of the arc and the auroral poleward boundary. The poleward boundary in this case was diffuse, and was thus determined as the boundary (dashed white curve in Figure 7.2c) between the faint continuous emissions, i.e. auroral oval (a couple hundred count/s at < 72-73° MLAT) and the dark region (<100 count/s at ~74°), i.e. polar cap. This gives a contact time at 0600 UT. No substantial oval disturbance was observed until the initiation of the PBI at 0604 UT (Figure 7.2e, second dashed line). This finite time delay would indicate the time scale of instability growth in the plasma sheet and of M-I communication time.

We also determined the longitudinal relation between polar cap arcs and their related PBIs by examining the 630.0 nm ewogram (not shown), which shows the time-dependent east-west auroral evolution at a certain latitude. We found that the central longitude of the PBI initiated 11° east of that of the polar cap arc at the contact time (also seen in Figure 7.1e). Note this displacement resulted purely from the finite longitudinal width of the PBI (15°) and the arc (8°), as they two were spatially connected with each other at their eastern and western edges, respectively (Figure 7.1e).

The radar detected a localized fast anti-sunward flow associated with the polar cap arc (Figure 7.2d). A careful examination of Figure 7.2c and 7.2d shows a ~2 min uncertainty in using polar cap arcs to trace localized flow enhancements. While the flow enhancement (>~ 300 m/s) reached 74° MLAT at 0556 UT in Figure 7.2d, the polar cap arc had already extended to the same latitude at 0554 UT in Figure 7.2c. This difference could result from the 630.0 nm mapping uncertainties and only 1-D flow measurements, and it could partially reflect the longer (1 min) resolution of the radar data. It could also suggest a real offset of the front locations of the arc and the flow, which would require further examination of the 2-D flow pattern surrounding the leading edge of an arc and is beyond the focus of the current study.

One should note that the magnetic perturbations associated with the observed PBI were small (Figure 7.2g), magnitude being only a few nT, likely due to the prolonged northward Bz and quiet geomagnetic condition. Also, although the auroral brightening and poleward expansion at ~0700 UT appeared like a typical substorm, its magnetic perturbation was quite small (a few tens of nT). Nevertheless, the quietness does not deemphasize the importance of the PBI, because it was the only major optical intensification in the auroral oval within the preceding 1 h and over the 5-h MLT observing range, and its equatorward extension led to a subsequent, significant auroral brightening and expansion.

7.2.2 Thin Oval: Poleward Expanding Intensification

Figures 7.3 and 7.4 show the association of a polar cap arc with poleward-expanding intensifications within a thin auroral oval on Mar 17, 2010. Red line observation at the GILL station was not available, and white light measurements from THEMIS ASI are shown in grey scale instead. The polar cap arc was propagating duskward and equatorward and its evolution well traced a narrow, fast, equatorward-directed flow moving with it (Figure 7.3a and 7.3b). The arc extended equatorward of the FOV of RESU, likely into GILL. Although GILL could not detect faint and fine structures due to its partially cloudy sky condition, TALO white light observation in Figure 7.4c affirms the arc's extension at least to 73° MLAT. Note the white light emission is insensitive to low-energy precipitation (only a few tens count/s increase from the background) and thus in general does not favor polar cap arc detection.

An intensification along the only resolvable arc developed within GILL at a longitude seemingly to be a continuation of the polar cap arc orientation (marked as intensification 1 in Figure 7.3c and Figure 7.4d). This intensification exhibited substantial poleward expansion of a surge (from Figure 7.3d to 7.3e, > 3° in MLAT), indicating a substantial change in magnetic topology in the magnetotail. Although this expansion resembles auroral substorms, it is unclear whether it started from the equatorward arc or not given this thin oval. Therefore we call it a "poleward-expanding intensification". Its westernmost edge was marked by and propagated together with the polar cap arc, suggesting that the arc associated fast flows within the polar cap continuously flowed towards, and possibly across, the auroral poleward boundary into the region of disturbance.

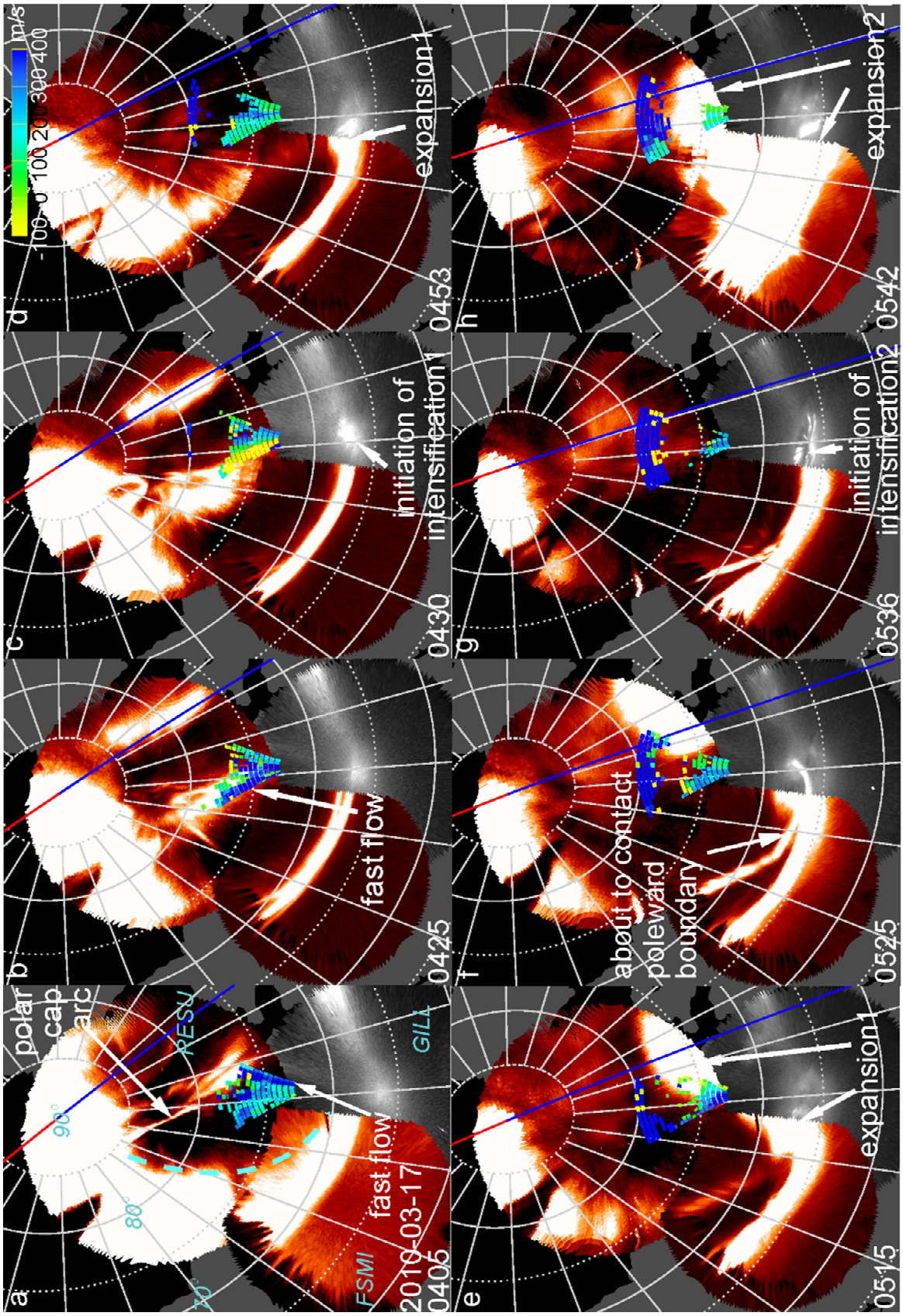
a
polar cap arc
90°
80°
70°
RESU
FSMI
GILL
fast flow
2010-03-17
0405
b
fast flow
0425
c
initiation of intensification 1
0430
d
-100 -0 100 200 300 400 m/s
expansion 1
0453
e
expansion 1
0515
f
about to contact poleward boundary
0525
g
initiation of intensification 2
0536
h
expansion 2
0542

Figure 7.3 630.0 nm snapshots showing the association of a polar cap arc to poleward expanding intensifications within a thin auroral oval on Mar 17, 2010, in a similar format as Figure 7.1. The intense emissions near magnetic noon within RESU FOV was due to sunlight contamination. [*Zou et al.*, 2015b]

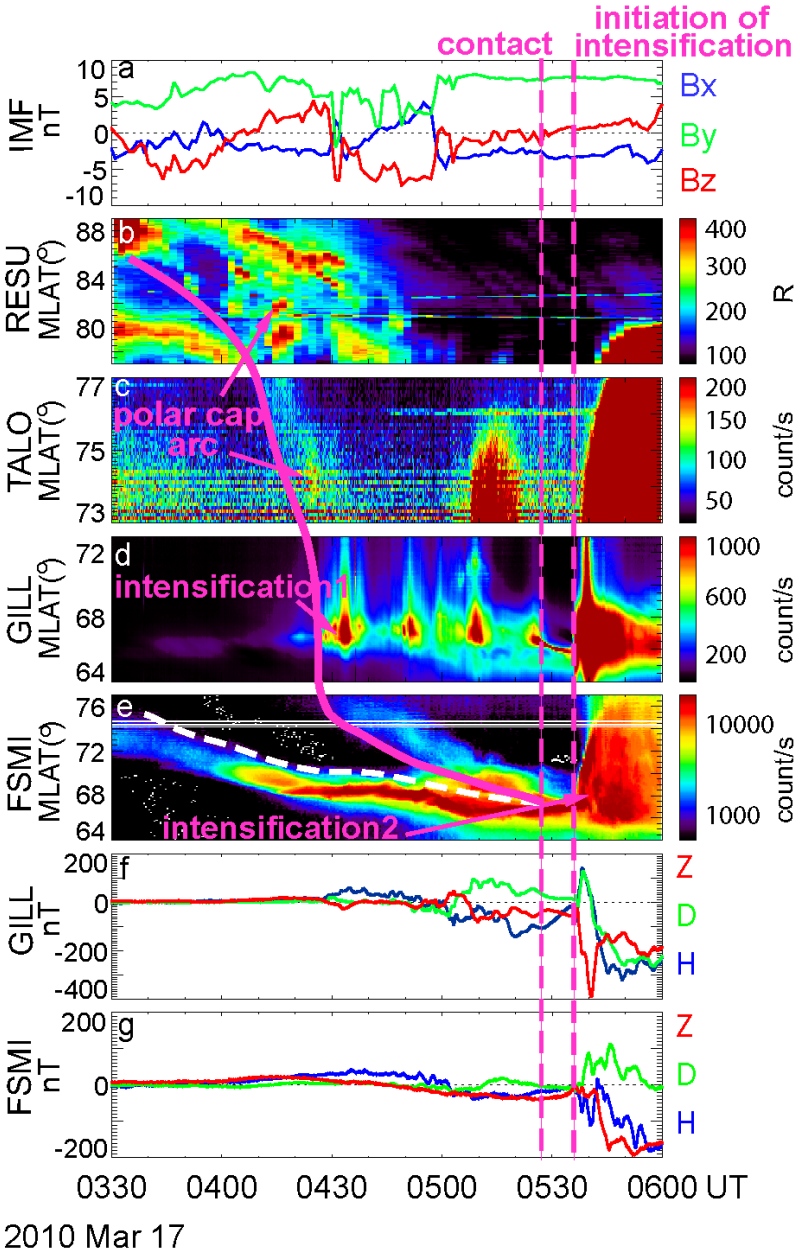

Figure 7.4 Time series showing the association of the polar cap arc to poleward expanding intensifications shown in Figure 5, in a similar format as Figure 2. Panel b-e are 630.0 nm observation from RESU, white light observation from TALO and GILL, and 630.0 nm observation from FSMI. RESU and GILL keograms integrate emissions from almost the entire longitudinal range of the images, and TALO and FSMI keograms center on the longitude of the polar cap arc and the longitude of its contact with auroral oval, respectively. [*Zou et al.*, 2015b]

As intensification 1 subsided, the polar cap arc re-brightened and continued its contact with the auroral oval at an angle almost parallel to the oval (Figure 7.3f). Following this and at the same longitude, a second intensification initiated (Figure 7.3g) and again expanded substantially poleward all the way to ~80° MLAT. This sequence is also identified in the keogram of Figure 7.4e, which presents observation around the contact longitude (~6° wide).

The auroral poleward boundary is marked by the dashed white curve, as inferred from the poleward edge of the only detectable arc within the oval. The bulge of light extending poleward of the white curve between 0450 and 0525 UT was mainly due to atmospheric scattering of emissions of intensification 1 from other longitudes. The polar cap arc extended equatorward towards and impinged onto the poleward boundary at 0527 UT, and 9 min later the oval intensification initiated and expanded poleward. This disturbance has substantial magnetic perturbation, ~300 nT (Figure 7.4f).

7.3 Statistics

Using criteria listed in Section 7.1, we identified 34 steady and long-lasting polar cap arcs. Although such long-lasting arcs are not as common as short-lived ones which have an average lifetime of ~tens of minutes [*Zhu et al.*, 1997], they enable us to exclude transient and dynamic polar cap processes and to thus avoid finding coincidental association with auroral oval disturbances. The identified arcs were typically of a few hundred R in 630.0 nm, mostly below the detection threshold of low-sensitivity satellite imaging (~ kR), and were likely due to accelerated polar rain on open field lines [*Carlson and Cowley,* 2005]. This is consistent with our simultaneous radar measurements surrounding the arcs, which showed localized enhanced flows directed anti-sunward, the same direction as convection of open field lines.

We examined how commonly polar cap arcs were associated with significant disturbances within the nightside auroral oval as they extended to and collided on the auroral poleward boundary. To define an association, we required the arc to be spatially connected to the oval intensification. The intensification should be substantial and quasi-steady, i.e. persisting >~ 10 min with a peak intensity > 1000 count/s. Its initiation time and median longitude within the first 2 min were measured in a similar way to the events in Section 7.2, and were then compared with the contact of the polar cap arc with the auroral oval in order to derive time lag and

longitudinal separation. Its localization was quantified as its initial longitudinal width within the first 2 min. The IMF and geomagnetic conditions of the observed polar cap-auroral oval coupling was also examined.

The identification of such contact or connection is subject to mapping altitude uncertainties, which are on the order of tens of km given a mapping altitude of 250 km [*Solomon et al.*, 1988; *Jackel et al.*, 2003]. This is equivalent to <~ 2 min uncertainty in time (assuming a 700 m/s fast flow), and <~3° uncertainty in longitude at 75° MLAT. These uncertainties are too small to affect our conclusions.

7.3.1 Basic Properties of Polar Cap-Auroral Oval association

Figure 7.5a shows the occurrence frequency of different types of responses in the auroral oval after contact by a polar cap arc. Four categories are presented: PBIs, intensifications in a thin oval with and without poleward expansion, and no substantial oval response. For 85% of the events, the contact by a polar cap arc was followed by intensifications in the auroral oval within one of the three categories exemplified by the three case studies in Section 7.2. These intensifications were all major disturbances that were distinctly different from the otherwise quiet aurora activity. In 32% of events, oval disturbances appeared as the most poleward intensifications within the oval, i.e. PBIs under a thick oval. These PBIs may or may not extend equatorward leading to small substorm or pseudo-breakup activity. When the oval was narrow (thin oval), oval disturbances appeared as intensifications of the only detectable arc (53%), which sometimes exhibited substantial poleward expansion (> 3° latitude, 21%). Only 15% of our cases showed no substantial oval responses. This does not necessarily mean an absolute lack of responses in those cases, since faint or transient intensifications below our thresholds were observed in 3 of the 5 cases.

Figure 7.5b shows the time lag of oval intensifications relative to the impingement of polar cap arcs on auroral poleward boundary. Here the impingement was required to occur well within one 630.0 nm ASI FOV to avoid uncertainties introduced when taking measurements from two different ASIs. Clear sky condition with almost no clouds was also required. Most of the oval intensification occurred within 11 min from the time of impingement, which is likely due to the time scales of oval instability development and M-I communication. This time delay was about the same for all three types of oval responses, though was slightly shorter for the PBI category (≤ 8 min). The long-delay case (15-17 min) had faint and transient

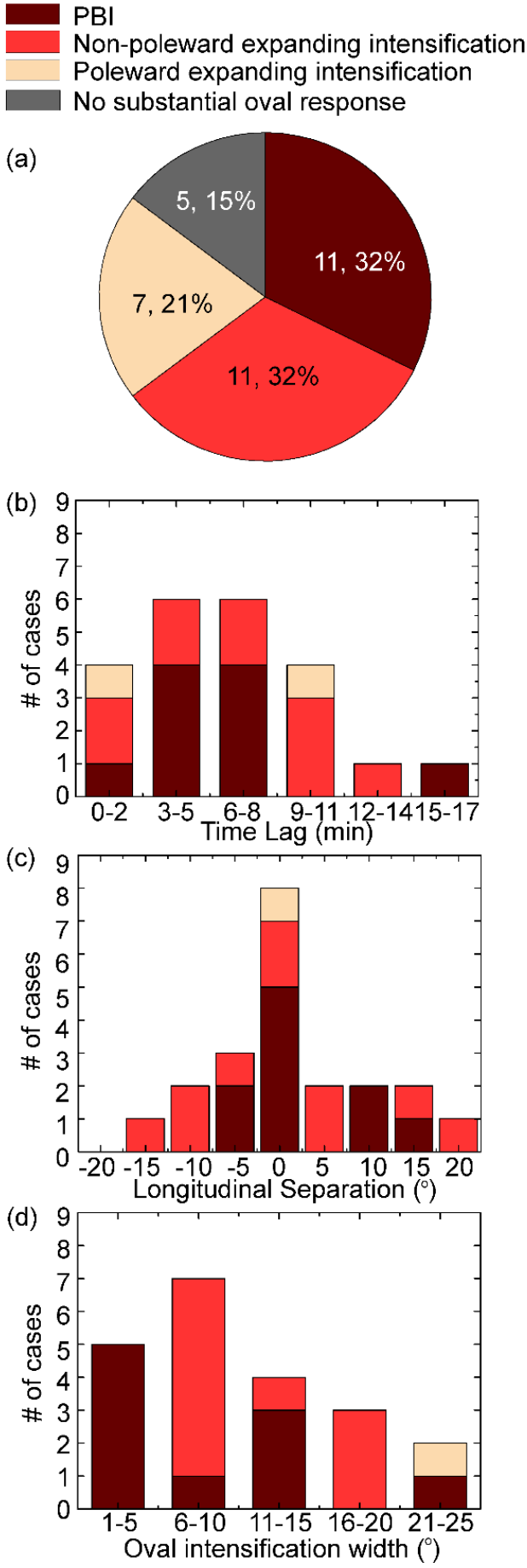

Figure 7.5 (a) Occurrence Frequency of auroral oval intensifications in association with polar cap arcs. (b) Time lag of oval intensifications relative to the time when polar cap arcs contact the auroal oval. (c) Separation of oval intensification initiation longitude (within first 2 min) relative to the longitude where polar cap arcs contact the auroral oval. Positive (negative) values indicate oval intensifications to locate east (west) of the contacting location. (d) Longitudinal width of oval intensifications within first 2 min of initiation. [*Zou et al.*, 2015b]

PBIs below our selection criteria in association with the polar cap arc before the larger PBI formed.

Note that the time lag here is longer than what is derived based on radar measurements alone [*Zou et al.*, 2014] (0-2 min). This may result from a possible offset between leading edges of fast flows and polar cap arcs, as seen in Figure 7.2, making the determinations on when they reach the auroral poleward boundary slightly inconsistent from one to the other. It could also be due to differences in magnetic-field aligned communication times between magnetotail reconnection events and the field-aligned currents flowing into the ionosphere giving rise to auroral disturbances [*Song and Vasyliūnas*, 2002]. Nevertheless, both results suggest a short time lag indicating that polar cap arcs and associated fast flows are closely followed by oval disturbances in time.

Figure 7.5c shows the longitudinal separation of oval intensifications from the impinging longitude of polar cap arcs. The narrow peak at 0° suggests almost no longitudinal separation. The spread of the distribution was mostly limited within ± 1 h MLT. Note this separation was contributed by the finite longitudinal width of oval intensifications and polar cap arcs as the two were spatially connected with each other. The initial longitudinal width of oval intensifications, as shown in Figure 7.5d, was mostly localized (<~ 1 h MLT).

7.3.2 IMF and Geomagnetic Dependences of Polar Cap-Auroral Oval Association

To investigate the IMF and geomagnetic conditions of the observed polar cap-auroral oval coupling, we have examined OMNI solar wind data from 2 h before until 1 h after polar cap arcs reached the auroral oval. This covers conditions for polar cap arcs to form, extend

equatorward, and impinge on the oval, as well as conditions when oval intensifications occurred. Median values over this 3-hour interval are shown for the three IMF components and IMF clock angle in Figure 7.6a-d, and the maximum value for *AE* index is shown in Figure 7.6e. Clock angle is the angle between GSM north and the projection of the IMF vector onto the GSM *y*-*z* plane. Included events are the same as Figure 7.5b-d.

Figure 7.6a-d shows that our events mostly occurred under –*Bx*, +*By*, and +*Bz*, and |*By*| tends to be larger than |*Bz*|. +*Bz* has been long recognized to correlate with polar cap arc occurrence. The occasional presence under –*Bz* is due to arcs' slow response to changes of IMF polarity with a time delay of a few tens of minutes [*Troshichev et al.*, 1988; *Valladares et al.*, 1994]. However, arcs' dependence on *By* and *Bx* remains controversial in the literature. Arcs' locations have been found to be either *By* independent [*Lassen and Danielesen* 1978; *Rairden and*

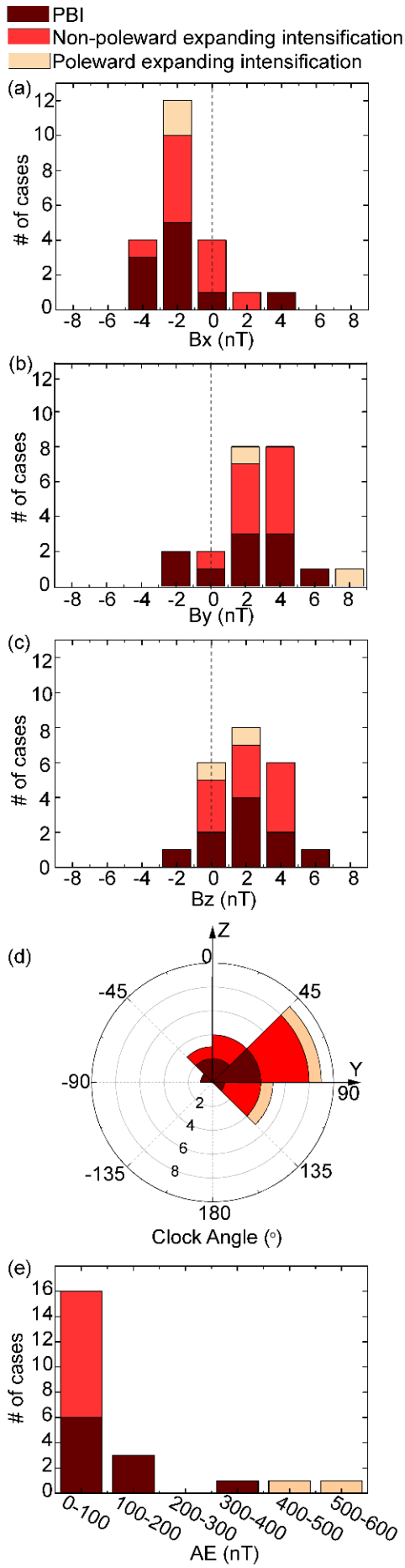

Figure 7.6 (a-d) Median values of IMF *Bx*, *By*, *Bz* in GSM coordinate and clock angle from 2 h before until 1 h after the time when polar cap arcs impinge on the auroral oval. (e) Maximum values of AE index within the same time interval. [*Zou et al.*, 2015b]

Mende 1989], or to be located preferentially in the premidnight (postmidnight) sector for positive (negative) *By* [*Gussenhoven*, 1982]. Such discrepancy might arise from the differences in the specific time interval used for averaging *By* [*Fear and Milan*, 2012]. Our results on +*By* preference might simply be a consequence of much more frequent arc occurrence on the dawnside of the polar cap than on the duskside, as reported by *Valladares et al.* [1994]. The dawnside arcs drift duskward across the polar cap under +*By* condition and thus could possibly impinge on the nightside auroral poleward boundary. The dawn-dusk drift dependence on *By* could be seen in the three case studies and the statistical analysis by *Rairden and Mende* [1989] and *Hosokawa et al.* [2011]. Just as for *By*, both no *Bx* dependence [*Ismail et al.*, 1977; *Gussenhoven,* 1982] and negative *Bx* preference [*Kullen et al.*, 2002] have been reported for polar cap arcs. It is noteworthy that the same negative *Bx* dependence was also found for polar cap electron acceleration region by *Burch et al.* [1979], which was interpreted as a result of interconnection of antiparallel IMF and magnetotail magnetic field lines. The dominance of *By* over *Bz* shown in Figure 7.6d is consistent with *Kullen et al.* [2002].

Our events mostly occurred under quiet geomagnetic conditions, with a peak occurrence at 0-100 nT in *AE* (Figure 7.6e), which is expected from the +*Bz* preference of polar cap arcs. Compared with intensifications during more active conditions, our oval disturbances have small magnetic perturbations. These small perturbations are still of importance, because they are the major disturbances during the presence of the long-lasting polar cap arcs, which we have considered here. The poleward-expanding intensifications produce the largest perturbations among the three categories and thus have the largest AE magnitude.

7.4 Summary

We have studied the impact of localized polar cap fast flows on nightside auroral oval activity by combining radar and 630.0 nm optical measurements. Good correspondences have

been found between the location and motion of localized flow enhancements and polar cap arcs when radar echoes are available. This enables us to trace flows using polar cap arcs over long distances and in 2-D, and to thus provide answers to questions that could not be resolved by using radar measurements alone, such as the flow source and evolution and the 2-D relation of flows to oval intensifications.

We characterized three types of nightside oval intensifications in response to polar cap arcs that impinge upon the auroral poleward boundary: PBIs, and non-poleward and poleward expanding intensifications. They are all spatially connected to polar cap arcs, and occur within a few minutes and <~ 10° longitudes. They are major disturbances within our observing time intervals and longitudinal ranges, and such disturbances do not occur until polar cap arcs contact the oval and initiate right around the contacting longitudes. Such direct spatial connection and proximity in time and location indicates that these intensifications are not coincidental but closely related to, and possibly triggered by, the flows identified by the arcs.

Our statistical study based on over 6 years of data suggests that almost all (85%) polar cap arcs substantially impact activity within the nightside auroral oval as they impinge on the oval. This impact is often localized (<~ 1 h MLT) and consistently initiates within a few minutes delay and at almost the same longitude. Our events mostly occur under $-Bx$, $+By$, and $+Bz$ conditions, with By component dominating Bz. Consistent with $+Bz$, our geomagnetic conditions are generally quiet.

Chapter 8. Conclusion and Open Questions

We have examined the large-scale equatorward boundaries of the nightside auroral oval utilizing coordinated observations of MSPs from NORSTAR and white light ASIs from THEMIS. The utilized 630.0 nm emission contains information of low energy electron precipitation, and thus enables a more reliable detection of the location of the electron aurora than the previous work. Both the electron and the proton auroras contribute to the diffuse glow at the equatorward border of the auroral oval in white light observations, suggesting the potential of utilizing THEMIS ASIs to study the 2-D spatiotemporal evolution of the inner magnetosphere. The proton and the electron auroras are latitudinally displaced from each other, the relative displacement dependent on geomagnetic activity. Both types of auroras expand equatorward with increasing geomagnetic activity and the expansion is more prominent for the electron aurora than the proton aurora. Such optical observation is verified by conjunct satellite particle measurements.

We investigated whether the occurrence of PBIs, one important meso-scale aurora generated by magnetotail reconnection, is statistically related to localized enhanced flows near the nightside auroral poleward boundary in the polar cap in 1-D. We utilized coordinated observations of a white light ASI from THEMIS and a radar located at the same place from SuperDARN. The identified polar cap flow-PBI relation is consistent with the limited case studies presented in previous work, i.e. PBIs being associated with narrow fast flows near the PBI longitude and extending toward the auroral poleward boundary. Such association almost always occur (~90%). Flows occur simultaneously with or 1–2 min prior to PBIs and have a duration and width comparable to those of PBIs.

In order to examine the source and prior evolution, as well as the basic properties, of the observed polar cap flows, we explore the feasibility of 2-D flow tracing using airglow patches.

The polar cap 630.0 nm ASI has broad FOV and provides 2-D monitoring, complementing limitations of radar measurements from SuperDARN. The coordinated observation shows that localized polar cap flow enhancements are commonly (67%) collocated with airglow patches and their shape, speed, and 2-D direction are well reflected by the simultaneous shape, speed, and motion of airglow patches. This indicates that airglow patches can be used as an optical tracer of these flows, i.e., using radars to detect localized flows in their limited echo region and employing an ASI to infer their shape and direction in 2-D.

Utilizing this flow-patch association, we found that localized polar cap flow enhancements typically propagate at ~600 m/s, persist a few tens of minutes within our FOV, and are of a few hundred km width in the ionosphere. They mostly occur under $\pm B_y$-dominated, are orientated quasi-parallel to the noon-midnight meridian, and propagate in a direction consistent with IMF *By* component. They substantially contribute to the convection across the polar cap.

Equipped with optical tracing, we then determined how localized polar cap flow enhancement impact nightside auroral oval activity over long distance and in 2-D based on an array of 630.0 nm ASIs from NASCAM and OMTI and radars from SuperDARN. The optically faint and diffuse nature of airglow patches does not allow for accurate determination of the flow propagation. Therefore we used polar cap arcs, which are bright and discrete and can thus highlight when and where flows contact the nightside auroral oval with high accuracy. Arcs well represent the location and motion of localized flow enhancements and as they impinge on the auroral poleward boundary, they are always (85%) followed by intensifications within the auroral oval that are spatially connected to them, and occur within a few minutes and <~ 10° longitudes. Such intensifications are major disturbances within our observing time intervals and longitudinal ranges, and they do not occur until the impingement of polar cap arcs. This suggests that these intensifications are not coincidental but closely related to, and possibly

triggered by, the flows identified by the arcs. The studied polar cap arcs mostly occur under –*Bx*, +*By*, and +*Bz* conditions, with *By* component dominating *Bz*.

The above results are achieved based on our innovative combination of radars and ASIs which have been only available in recent years, and the simultaneous examination of the convection and the auroral evolution systematically and statistically. These new observational results imply nightside reconnection to be externally triggered and to develop upon the intrusion of lobe flow bursts. However, the generalization of this process requires further flow tracing under –*Bz* and active conditions because of the much larger plasma sheet disturbances under such conditions and their importance for magnetic flux and energy flux transport. Radar measurements suggest that at least some of these disturbance are preceded by polar cap flows in the vicinity, although the prior flow evolution remains ambiguous. Tracing these flows all the way from deep in the polar cap requires continuous monitoring of airglow patches, and their optically faint and diffuse nature requires high-sensitivity 630.0 nm imaging. Such ASIs have been recently deployed in 2014, and future observations will be useful for such studies under geomagnetic active conditions. These ASIs can be further used to evaluate the percentage of PBIs/reconnection being externally triggered, providing information on the dominant mechanism for them to develop.

The magnetospheric counterpart of localized flow enhancements in the polar cap is unclear. This can be examined using satellite conjunctions with airglow patches and polar cap arcs whose wide spatial extents provide more chances for conjunctions than the limited radar echoes.

Although our results trace the origin of nightside geomagnetic disturbance to the polar cap, how localized flow features there are created is another open question. Flows that are traced by airglow patches are assumed to be originated from dayside magnetic reconnection. However, despite of the repetitive occurrence of dayside flow bursts, flows in the polar cap are

observed with a much lower frequency. Whether this is due to our observation limitation or truly reflects a low survival rate is unknown, and the solution requires instantaneous observations of both dayside and polar cap convection, which has been scheduled to operate both on ground and in the magnetosphere in the upcoming years. If it is the latter, conditions favoring prolonged flow lifetime are worthwhile to investigate. On the other hand, the source of flows that are traced by polar cap arcs is controversial and one helpful approach is to examine the in-situ precipitating particles during the temporal development of these arcs.

Nevertheless, our results suggest that locally enhanced nightside auroras, and the associated magnetic reconnection, can be preceded by, and developed around, localized flow enhancements arriving at the poleward boundary of the auroral oval from the polar cap. This preceding signature in the polar cap is essential to understand the development of magnetotail reconnection, and gives the potential of forecasting the specific time and location of disturbances in the plasma sheet and the auroral oval by 1-2 hour. It also implies that an enhanced meso-scale convection system is regulating the dynamic perturbations of the magnetosphere.

References/Bibliography

Anderson, D. N., D. T. Decker, and C. E. Valladares (1996), Modeling boundary blobs using time varying convection, *Geophys. Res. Lett.*, **23**, 579–582, doi:10.1029/96GL00371.

Angelopoulos, V., W. Baumjohann, C. F. Kennel, F. V. Coroniti, M. G. Kivelson, R. Pellat, R. J. Walker, H. Lühr, and G. Paschmann (1992), Bursty bulk flows in the inner central plasma sheet, J. Geophys. Res., 97(A4), 4027–4039, doi:10.1029/91JA02701.

Angelopoulos, V., C. F. Kennel, F. V. Coroniti, R. Pellat, M. G. Kivelson, R. J. Walker, C. T. Russell, W. Baumjohann,W. C. Feldman, and J. T. Gosling (1994), Statistical characteristics of bursty bulk flow events, *J. Geophys. Res.*,**99**(A11), 21,257–21,280, doi:10.1029/94JA01263.

Baker, J. B., C. R. Clauer, A. J. Ridley, V. O. Papitashvili, M. J. Brittnacher, and P. T. Newell (2000), The nightside poleward boundary of the auroral oval as seen by DMSP and the Ultraviolet Imager, *J. Geophys. Res.*, **105**(A9),21,267–21,280, doi:10.1029/1999JA000363.

Barbier, D., F. E. Roach, and W. R. Steiger, The summer intensity variations of [OI] 6300 A in the tropics, J. Res. NBS, 66D, 145, 1962

Basu, S., E. MacKenzie, Su. Basu, P. F. Fougere, N. C. Maynard, W. R. Coley, W. B. Hanson, J. D. Winningham, M. Sugiura, and W. R. Hoegy (1988), Simultaneous density and electric field fluctuation spectra associated with velocity shears in the auroral oval, J. Geophys. Res., 93, 115–136, doi:10.1029/JA093iA01p00115.

Basu, S., S. Basu, E. MacKenzie, W. R. Coley, J. R. Sharber, and W. R. Hoegy (1990), Plasma structuring by the gradient drift instability at high latitudes and comparison with velocity shear driven processes, *J. Geophys. Res.*,**95**(A6), 7799–7818, doi:10.1029/JA095iA06p07799.

Baumjohann, W. J., G. Paschmann, and H. Lühr (1990), Characteristics of high-speed flows in the plasma sheet,*J. Geophys. Res.*, **95**, 3801–3809, doi:10.1029/JA095iA04p03801.

Baumjohann, W., and R. A. Treumann (1997), Basic Space Plasma Physics, 2nd ed., Imperial College Press, London.

Blanchard, G. T., L. R. Lyons, J. C. Samson, and F. J. Rich (1995), Locating the polar cap boundary from observations of 6300 Å auroral emission, J. Geophys. Res., 100(A5),7855–7862, doi:10.1029/94JA02631.

Blanchard, G. T., L. R. Lyons, and J. C. Samson (1997), Accuracy of 6300 Å auroral emission to identify the separatrix on the night side of the Earth, *J. Geophys. Res.*, **102**, 9697–9703.

Boakes, P. D., S. E. Milan, G. A. Abel, M. P. Freeman, G. Chisham, B. Hubert, and T. Sotirelis (2008), On the use of IMAGE FUV for estimating the latitude of the open/closed magnetic field line boundary in the ionosphere,*Ann. Geophys.*, **26**(9), 2759–2769.

Burch, J., S. Fields, and R. Heelis (1979), polar cap electron acceleration regions, J. Geophys. Res. 84(A10), 5863–5874, doi:10.1029/JA084iA10p05863.

Cao, J., et al. (2008), Characteristics of middle- to low-latitude Pi2 excited by bursty bulk flows, J. Geophys. Res.,113, A07S15, doi:10.1029/2007JA012629.

Carbary, J. F., T. Sotirelis, P. T. Newell, and C.-I. Meng (2003), Auroral boundary correlations between UVI and DMSP, *J. Geophys. Res.*, **108**(A1, 1018), doi:10.1029/2002JA009378.

Carlson, C. W., R. F. Pfaff, and J. G. Watzin (1998), The Fast Auroral Snapshot (FAST) mission, *Geophys. Res. Lett.*,**25**, 2013–2016, doi:10.1029/98GL01592.

Carlson, H. C., K. Oksavik, J. Moen, and T. Pedersen (2004), Ionospheric patch formation: Direct measurements of the origin of a polar cap patch, *Geophys. Res. Lett.*, **31**, L08806, doi:10.1029/2003GL018166.

Carlson, H. C., and S. W. H. Cowley (2005), Accelerated polar rain electrons as the source of Sun-aligned arcs in the polar cap during northward interplanetary magnetic field conditions, J. Geophys. Res.,110, A05302, doi:10.1029/2004JA010669.

Carlson, H. C., J. Moen, K. Oksavik, C. Nielsen, I. W. McCrea, T. Pedersen and P. Gallop (2006), Direct observations of injection events of subauroral plasma into the polar cap, *Geophys. Res. Lett.*, **33**, L05103, doi:10.1029/2005GL025230.

Chang, S.-W., et al. (1998), A comparison of a model for the theta aurora with observations from Polar, Wind, and SuperDARN, *J Geophys. Res.*, **103**, 17,367.

Chisham, G., et al. (2007), A decade of the Super Dual Auroral Radar Network (SuperDARN): Scientific achievements, new techniques and future directions, *Surv. Geophys.*, **28**, 33–109, doi:10.1007/s10712-007-9017-8.

Cogger, L., J. Walker, J. Meriwether Jr., and R. Burnside (1980), *F* region airglow: Are ground-based observations consistent with recent satellite results?, J. Geophys. Res., 85(A6), 3013–3020, doi:10.1029/JA085iA06p03013.

Creutzberg, F., R. L. Gattinger, F. R. Harris, S. Wozniak, and A. V. Jones (1988), Auroral Studies with a chain of meridian scanning photometers: 2. Mean distributions of proton and electron aurora as a function of magnetic activity, J. Geophys. Res., 93(A12), 14,591–14,601, doi:10.1029/ JA093iA12p14591.

Crowley, G., A. J. Ridley, D. Deinst, S. Wing, D. J. Knipp, B. A. Emery, F. Foster, R. Heelis, M. Hairston, and B. W. Reinisch (2000), Transformation of high-latitude ionospheric F region patches into blobs during the March 21, 1990, storm, J. Geophys. Res., 105, 5215 – 5230.

Davidson, G. T. (1965), Expected spatial distribution of low-energy protons precipitated in the auroral zones, J. Geophys. Res., 70(5), 1061–1068, doi:10.1029/JZ070i005p01061.

de la Beaujardière, O., L. R. Lyons, J. M. Ruohoniemi, E. Friis-Christensen, C. Danielsen, F. J. Rich, and P. T. Newell (1994), Quiet-time intensifications along the poleward auroral boundary near midnight, *J. Geophys. Res.*,**99**, 287–298, doi:10.1029/93JA01947.

Donovan, E. F., B. J. Jackel, I. Voronkov, T. Sotirelis, F. Creutzberg, and N. A. Nicholson (2003),Ground-based optical determination of the b2i boundary: A basis for an optical MT-index, J. Geophys. Res., 108, 1115, doi:10.1029/2001JA009198, A3.

Donovan, E.*, et al. (*2003*),* Auroral imaging in Canadian CANOPUS and NORSTAR programs*, paper presented at* the 30th Annual European Meeting on Atmospheric Studies by Optical Methods*, Univ. Courses on Svalbard,* Longyearbyen, Norway.

Donovan, E., et al. (2006), The THEMIS all-sky imager array–system design and initial results from the prototype imager, J. Atmos. Sol. Terr. Phys., 68, 1472–1487, doi:10.1016/j.jastp.2005.03.027.

Drury, E. E., S. B. Mende, H. U. Frey, and J. H. Doolittle (2003), Southern Hemisphere poleward moving auroral forms, *J. Geophys. Res.*, **108**(A3), 1114, doi:10.1029/2001JA007536.

Eastwood, J. P., T. D. Phan, R. C. Fear, D. G. Sibeck, V. Angelopoulos, M. Øieroset, and M. A. Shay (2012), Survival of flux transfer event (FTE) flux ropes far along the tail magnetopause, J. Geophys. Res., 117, A08222, doi:10.1029/2012JA017722.

Eather, R. H. (1968), Spectral intensity ratios in proton-induced auroras, J. Geophys. Res., 73(1), 119–125, doi:10.1029/JA073i001p00119. A06206

Eather, R. H., and S. B. Mende (1972), High-latitude particle precipitation and source regions in the magnetosphere, in Magnetosphere Ionosphere Interactions, edited by K. Folkestad, pp. 139–154, Univ. Press, Oslo.

Echim, M. M., Maggiolo, R., Roth, M., and De Keyser, J.: A magnetospheric generator driving ion and electron acceleration and electric currents in a discrete auroral arc observed by Cluster and DMSP, Geophys. Res. Lett., 36, L12111, doi:10.1029/2009GL038343, 2009.

Elphic, R. C., M. Lockwood, S. W. H. Cowley, and P. E. Sandholt (1990), Flux transfer events at the magnetopause and in the ionosphere, *Geophys. Res. Lett.*, **17**, 2241–2244, doi:10.1029/GL017i012p02241.

Fairfield, D. H., and A. F. Viñas (1984), The inner edge of the plasma sheet and the diffuse aurora, J. Geophys. Res., 89(A2), 841–854, doi:10.1029/JA089iA02p00841.

Fang, X., M. W. Liemohn, J. U. Kozyra, and S. C. Solomon (2005), Study of the proton arc spreading effect on primary ionization rates, J. Geophys. Res., 110, A07302, doi:10.1029/2004JA010915.

Fasel, G. J. (1995), Dayside poleward moving auroral forms: A statistical study, *J. Geophys. Res.*, **100**,11,891–11,905, doi:10.1029/95JA00854.

Fear, R. C., and S. E. Milan (2012), The IMF dependence of the local time of transpolar arcs: Implications for formation mechanism, J. Geophys. Res., 117, A03213, doi:10.1029/2011JA017209.

Frank, L. A., and J. D. Craven (1988), Imaging results from Dynamics Explorer 1, Rev. Geophys., 26(2), 249–283, doi:10.1029/RG026i002p00249.

Frey, H. U., S. B. Mende, C. W. Carlson, J.-C. Gérard, B. Hubert, J. Spann, R. Gladstone, and T. J. Immel (2001), The electron and proton aurora as seen by IMAGE-FUV and FAST, Geophys. Res. Lett., 28(6), 1135–1138, doi:10.1029/2000GL012352.

Fukunishi, H. (1975), Dynamic relationship between proton and electron auroral substorms, J. Geophys. Res., 80(4), 553–574, doi:10.1029/ JA080i004p00553.

Fuselier, S. A., S. P. Gary, M. F. Thomsen, E. S. Claflin, B. Hubert, B. R. Sandel, and T. Immel(2004), Generation of transient dayside subauroral proton precipitation, J. Geophys. Res., 109, A12227, doi:10.1029/2004JA010393.

Gilson, M. L., J. Raeder, E. Donovan, Y. S. Ge, and L. Kepko (2012), Global simulation of proton precipitation due to field line curvature during substorms, J. Geophys. Res., 117, A05216, doi:10.1029/2012JA017562.

Gorin, J. D., A. V. Koustov, R. A. Makarevich, J.-P. St. Maurice, and S. Nozawa (2012), Velocity of E-region HF echoes under strongly-driven electrojet conditions, *Ann. Geophys.*, **30**, 235–250, doi:10.5194/angeo-30-235-2012.

Grocott, A., T. K. Yeoman, R. Nakamura, S. W. H. Cowley, H. Reme, and B. Klecker (2004), Multi-instrument observations of the ionospheric counterpart to a bursty bulk flow in the near-Earth plasma sheet, *Ann. Geophys.*, **22**, 1061–1075, doi:10.5194/angeo-22-1061-2004.

Gussenhoven, M. S., D. A. Hardy, and W. J. Burke (1981), DMSP/F2 electron observations of equatorward auroral boundaries and their relationship to magnetospheric electric fields, J. Geophys. Res., 86(A2), 768–778, doi:10.1029/JA086iA02p00768.

Gussenhoven (1982), M. S., Extremely high-latitude auroras, J. Geophys. Res., 87, 2401.

Gussenhoven, M. S., D. A. Hardy, and N. Heinemann (1987), The equatorward boundary of auroral ion precipitation, J. Geophys. Res., 92(A4), 3273–3283, doi:10.1029/JA092iA04p03273.

Haaland, S. E., G. Paschmann, M. Förster, J. M. Quinn, R. B. Torbert, C. E. McIlwain, H. Vaith, P. A. Puhl-Quinn, and C. A. Kletzing (2007), High-latitude plasma convection from Cluster EDI measurements: Method and IMF-dependence, *Ann. Geophys.*, **25**, 239–253, doi:10.5194/angeo-25-239-2007.

Haldoupis, C. (1989), A review on radio studies of auroral E-region ionospheric irregularities, *Ann. Geophys.*, **7**,239–258.

Hardy, D. A., M. S. Gussenhoven, and D. Brautigam (1989), A statistical model of auroral ion precipitation, J. Geophys. Res., 94(A1), 370–392, doi:10.1029/JA094iA01p00370.

Hardy, D. A., W. McNeil, M. S. Gussenhoven, and D. Brautigam (1991), A statistical model of auroral ion precipitation: 2. Functional representation of the average patterns, J. Geophys. Res., 96(A4), 5539–5547, doi:10.1029/90JA02451.

Hardy, D. A., E. G. Holeman, W. J. Burke, L. C. Gentile, and K. H. Bounar (2008), Probability distributions of electron precipitation at high magnetic latitudes, J. Geophys. Res., 113, A06305, doi:10.1029/2007JA012746.

Henderson, M. G., J. S. Murphree, and J. M. Weygand (1996), Observations of auroral substorms occurring together with preexisting "quiet time" auroral patterns, J. Geophys. Res., 101(A11),24621–24640, doi:10.1029/96JA01252.

Hesse, M., and J. Birn, On dipolarization and its relation to the substom current wedge, J. Geophys. Res., 96, 19,417-19,426, 1991.

Horwitz, J. L., S. Menteer, J. Turnley, J. L. Burch, J. D. Winningham, C. R. Chappell, J. D. Craven,L. A. Frank, and D. W. Slater (1986), Plasma boundaries in the inner magnetosphere, J. Geophys. Res., 91(A8), 8861–8882, doi:10.1029/JA091iA08p08861.

Hosokawa, K., K. Shiokawa, Y. Otsuka, T. Ogawa, J.-P. St-Maurice, G. J. Sofko, and D. A. Andre (2009a), Relationship between polar cap patches and field-aligned irregularities as observed with an all-sky airglow imager at Resolute Bay and the PolarDARN radar at Rankin Inlet, *J. Geophys. Res.*, **114**, A03306, doi:10.1029/2008JA013707.

Hosokawa, K., T. Kashimoto, S. Suzuki, K. Shiokawa, Y. Otsuka, and T. Ogawa (2009b), Motion of polar cap patches: A statistical study with all-sky airglow

imager at Resolute Bay, Canada, *J. Geophys. Res.*, **114**, A04318, doi:10.1029/2008JA014020.

Hosokawa, K., J. I. Moen, K. Shiokawa, and Y. Otsuka (2011), Decay of polar cap patch, J. Geophys. Res., 116, A05306, doi:10.1029/2010JA016297.

Hosokawa, K., J. I. Moen, K. Shiokawa, and Y. Otsuka (2011), Motion of polar cap arcs, J. Geophys. Res., 116, A01305, doi:10.1029/2010JA015906.

Hull, A. J., J. W. Bonnell, F. S. Mozer, and J. D. Scudder, A statistical study of large-amplitude parallel electric fields in the upward current region of the auroral acceleration region, J. Geophys. Res.,108(A1), 1007, doi:10.1029/2001JA007540, 2003.

Hull, A. J., M. Wilber, C. C. Chaston, J. W. Bonnell, J. P. McFadden, F. S. Mozer, M. Fillingim, and M. L. Goldstein (2010), Time development of field-aligned currents, potential drops, and plasma associated with an auroral poleward boundary intensification, J. Geophys. Res., 115, A06211, doi:10.1029/2009JA014651.

Jackel, B., F. Creutzberg, E. Donovan, and L. Cogger (2003), Triangulation of auroral oxygen red line heights, Sodankylä Geophys. Obs. Publ., 92, 97–100.

Johnstone, A. D., D. M. Walton, R. Liu, and D. A. Hardy (1993), Pitch angle diffusion of low-energy electrons by whistler mode waves, J. Geophys. Res., 98(A4), 5959–5967, doi:10.1029/92JA02376.

Kamide, Y., and J. Winningham (1977), A statistical study of the 'instantaneous' nightside auroral oval: The equatorward boundary of electron precipitation as observed by the Isis 1 and 2 Satellites, J. Geophys. Res., 82(35), 5573–5588, doi:10.1029/JA082i035p05573.

Kauristie, K., J. Weygand, T. I. Pulkkinen, J. S. Murphree, and P. T. Newell (1999), Size of the auroral oval: UV ovals and precipitation boundaries compared, *J. Geophys. Res.*, **104**(A2), 2321–2331, doi:10.1029/1998JA900046.

Kennel, C. F., F. L. Scarf, R. W. Fredricks, J. H. McGehee, and F. V. Coroniti (1970), VLF electric field observations in the magnetosphere, J. Geophys. Res., 75(31), 6136–6152, doi:10.1029/JA075i031p06136.

Kepko, L. and Kivelson, M. G.: Generation of Pi2 pulsations by bursty bulk flows, J. Geophys. Res., 104, 25021–25034, 1999.

Kissinger, J., R. L. McPherron, T.-S. Hsu, and V. Angelopoulos (2011), Steady magnetospheric convection and stream interfaces: Relationship over a solar cycle, J. Geophys. Res., 116, A00I19, doi:10.1029/ 2010JA015763.

Knight, S., Parallel electric fields, Planet. Space Sci., 21, 741, 1973.

Koustov, A. V., D. W. Danskin, R. A. Makarevitch, and J. D. Gorin (2005), On the relationship between the velocity of E-region HF echoes and E B plasma drift, *Ann. Geophys.*, **23**(2), pp. 371–378, 0992-7689.

Koustov, A. V., D. André, E. Turunen, T. Raito, and S. E. Milan (2007), Heights of SuperDARN F region echoes estimated from the analysis of HF radio wave propagation, *Ann. Geophys.*, **25**, 1987–1994.

Koustov, A. V., J.-P. St.-Maurice, G. J. Sofko, D. Andre, J. W. MacDougall, M. R. Hairston, R. A. Fiori, and E. E. Kadochnikov (2009), Three-way validation of the Rankin Inlet PolarDARN radar velocity measurements, *Radio Sci.*, **44**, RS4003, doi:10.1029/2008RS004045.

Koustov, A., Hosokawa, K., Nishitani, N., Ogawa, T., and Shiokawa, K. (2008): Rankin Inlet PolarDARN radar observations of duskward moving Sun-aligned optical forms, Ann. Geophys., 26, 2711-2723, doi:10.5194/angeo-26-2711-2008.

Koustov, A. V., K. Hosokawa, N. Nishitani, K. Shiokawa, and H. Liu (2012), Signatures of moving polar cap arcs in the F-region PolarDARN echoes, *Ann. Geophys.*, **30**, 441–455, doi:10.5194/angeo-30-441-2012.

Kullen, A., M. Brittnacher, J. A. Cumnock, and L. G. Blomberg, Solar wind dependence of the occurrence and motion of polar auroral arcs: A statistical study, J. Geophys. Res., 107(A11), 1362, doi:10.1029/2002JA009245, 2002.

Kullen, A., and P. Janhunen (2004), Relation of Polar auroral arcs to magnetotail twisting and IMF rotation: A systematic MHD simulation study, *Ann. Geophys.*, **22**, 951.

Kuo, H., C. T. Russell, and G. Le (1995), Statistical studies of flux transfer events, J. Geophys. Res., 100(A3), 3513–3519, doi:10.1029/94JA02498.

Lassen, K., and C. Danielsen, Quiet time pattern of auroral arcs for different directions of the interplanetary magnetic field in the yz-plane, J. Geophys. Res., 83, 5277, 1978.

Lavraud, B., Opitz, A., Gosling, J. T., Rouillard, A. P., Meziane, K., Sauvaud, J.-A., Fedorov, A., Dandouras, I., Génot, V., Jacquey, C., Louarn, P., Mazelle, C., Penou, E., Larson, D. E., Luhmann, J. G., Schroeder, P., Jian, L., Russell, C. T., Foullon, C., Skoug, R. M., Steinberg, J. T., Simunac, K. D., and Galvin, A. B.: Statistics of counter-streaming solar wind suprathermal electrons at solar minimum: STEREO observations, Ann. Geophys., 28, 233-246, doi:10.5194/angeo-28-233-2010, 2010.

Le, G., C. T. Russell, and H. Kuo, Flux transfer events: Spontaneous or driven? Geophys. Res. Lett., 20, 791, 1993

Lee, L. C. and Fu, Z. F.: A theory of magnetic flux transfer at the Earth's magnetopause, Geophys. Res. Lett., 12, 105–108, 1985

Liou, K., P. T. Newell, and C.-I. Meng (2001), Seasonal effects on auroral particle acceleration and precipitation, J. Geophys. Res., 106(A4), 5531–5542, doi:10.1029/1999JA000391.

Liu, Z. X. and Fu, Y. D.: Local magnetic reconnection caused by vortices in the flow field, Geophys. Res. Lett., 15, 1752–1575, 1988.

Lockwood, M., P. E. Sandholt, A. D. Farmer, S. W. H. Cowley, B. Lybekk, and V. N. Davda (1990), Auroral and plasma flow transients at magnetic noon, *Planet. Space Sci.*, **38**, 973–993.

Lockwood, M., and H. C. Carlson (1992), Production of polar cap electron density patches by transient magnetopause reconnection, *Geophys. Res. Lett.*, **19**, 1731–1734, doi:10.1029/92GL01993.

Lockwood, M., and M. N. Wild (1993), On the quasi-periodic nature of magnetopause flux transfer events, *J. Geophys. Res.*, **98**,5935–5940.

Lockwood, M., H. C. Carlson Jr., and P. E. Sandholt (1993), Implications of the altitude of transient 630-nm dayside auroral emissions, *J. Geophys. Res.*, **98**(A9), 15,571–15,587, doi:10.1029/93JA00811.

Lorentzen, D. A., N. Shumilov, and J. Moen (2004), Drifting airglow patches in relation to tail reconnection,*Geophys. Res. Lett.*, **31**, L02806, doi:10.1029/2003GL017785.

Lorentzen, D. A., J. Moen, K. Oksavik, F. Sigernes, Y. Saito, and M. G. Johnsen (2010), In situ measurement of a newly created polar cap patch, *J. Geophys. Res.*, **115**, A12323, doi:10.1029/2010JA015710.

Lummerzheim, D., M. Galand, J. Semeter, M. J. Mendillo, M. H. Rees, and F. J. Rich (2001), Emission of OI (630 nm) in proton aurora, J. Geophys. Res., 106(A1), 141–148, doi:10.1029/2000JA002005.

Lummerzheim, D., M. Galand, and M. Kubota (2003), Optical emissions from proton aurora, *Sodankylä Geophys. Obs. Publ.*, 92, 1–5.

Lynch, K. A., D. Hampton, M. Mella, B. Zhang, H. Dahlgren, M. Disbrow, P. M. Kintner, M. Lessard, E. Lundberg, and H. C. Stenbaek-Nielsen (2012), Structure and dynamics of the nightside poleward boundary: Sounding rocket and ground-based observations of auroral

electron precipitation in a rayed curtain, *J. Geophys. Res.*,**117**, A11202, doi:10.1029/2012JA017691.

Lyons, L. R., G. T. Blanchard, J. C. Samson, J. M. Ruohoniemi, R. A. Greenwald, G. D. Reeves, and J. D. Scudder(1998), Near Earth plasma sheet penetration and geomagnetic disturbances, in New Perspectives on the Earth's Magnetotail, edited by A. Nishida, S. W. H. Cowley, and D. N. Baker, p. 241, AGU, Washington, D. C.

Lyons, L. R., T. Nagai, G. T. Blamchard, J. C. Samson, T. Yamamoto, T. Mukai, A. Nishida, and S. Kokubun (1999),Association between GEOTAIL plasma flows and auroral Poleward Boundary Intensifications observed by CANOPUS photometers, *J. Geophys. Res.*, **104**, 4485–4500, doi:10.1029/1998JA900140.

Lyons, L. R., Y. Nishimura, X. Xing, V. Angelopoulos, S. Zou, D. Larson, J. McFadden, A. Runov, S. Mende, and K.-H. Fornacon (2010), Enhanced transport across entire length of plasma sheet boundary field lines leading to substorm onset, *J. Geophys. Res.*, **115**, A00I07, doi:10.1029/2010JA015831.

Lyons, L. R., Y. Nishimura, H.-J. Kim, E. Donovan, V. Angelopoulos, G. Sofko, M. Nicolls, C. Heinselman, J. M. Ruohoniemi, and N. Nishitani (2011), Possible connection of polar cap flows to pre- and post-substorm onset PBIs and streamers, *J. Geophys. Res.*, **116**, A12225, doi:10.1029/2011JA016850.

MacDougall, J. W., and P. T. Jayachandran (2001), Polar cap convection relationships with solar wind, *Radio Sci.*,**36**(6), 1869–1880, doi:10.1029/2001RS001007.

Maynard, N. C., et al. (2003), Responses of the open–closed field line boundary in the evening sector to IMF changes: A source mechanism for Sun-aligned arcs, *J. Geophys. Res.*, **108**(A1), 1006, doi:10.1029/2001JA000174.

McEwen, D. J. (1998), Ionospheric dynamics in the central polar cap, *Adv. Space Res.*, **22**(9), 1327–1336.

McWilliams, K. A., Yeoman, T. K., and Provan, G.: A statistical survey of dayside pulsed ionospheric flows as seen by the CUTLASS Finland HF radar, Ann. Geophys., 18, 445–453, 2000.

Mella, M. R., K. A. Lynch, D. L. Hampton, H. Dahlgren, P. M. Kintner, M. Lessard, D. Lummerzheim,E. T. Lundberg, M. J. Nicolls, and H. C. Stenbaek-Nielsen (2011), Sounding rocket study of two sequential auroral poleward boundary intensifications, J. Geophys. Res., 116, A00K18, doi:10.1029/2011JA016428.

Mende, S. B., H. U. Frey, C. W. Carlson, J. McFadden, J.-C. Gérard, B. Hubert, S. A. Fuselier, G. R. Gladstone, and J. L. Burch (2002), IMAGE and FAST observations of substorm recovery phase aurora, Geophys. Res. Lett., 29(12), 1602, doi:10.1029/2001GL013027.

Mende, S. B., H. U. Frey, B. J. Morsony, and T. J. Immel (2003), Statistical behavior of proton and electron auroras during substorms, J. Geophys. Res., 108(A9), 1339, doi:10.1029/2002JA009751.

Mende, S. B., S. E. Harris, H. U. Frey, V. Angelopoulos, C. T. Russell, E. Donovan, B. Jackel, M. Greffen, and L. M. Peticolas (2008), The THEMIS array of ground-based observatories for the study of auroral substorms, *Space Sci. Rev.*, doi:10.1007/s11214-008-9380.

Mende, S. B., H. U. Frey, V. Angelopoulos, and Y. Nishimura (2011), Substorm triggering by poleward boundary intensification and related equatorward propagation, *J. Geophys. Res.*, **116**, A00I31, doi:10.1029/2010JA015733.

Meredith, N. P., R. B. Horne, R. M. Thorne, and R. R. Anderson (2009), Survey of upper band chorus and ECH waves: Implications for the diffuse aurora, J. Geophys. Res., 114, A07218, doi:10.1029/2009JA014230.

Milan, S. E., M. Lester, S. W. H. Cowley, K. Oksavik, M. Brittnacher, R. A. Greenwald, G. Sofko, and J.-P. Villain (2003), Variations in polar cap area during two substorm cycles, *Ann. Geophys.*, **21**, 1121–1140.

Milan, S. E., A. Grocott, C. Forsyth, S. M. Imber, P. D. Boakes, and B. Hubert (2009), A superposed epoch analysis of auroral evolution during substorm growth, onset and recovery: Open magnetic flux control of substorm intensity, Ann. Geophys., 27, 659–668, doi:10.5194/angeo- 27-659-2009.

Moen, J., N. Gulbrandsen, D. A. Lorentzen, and H. C. Carlson (2007), On the MLT distribution of F region polar cap patches at night, *Geophys. Res. Lett.*, **34**, L14113, doi:10.1029/2007GL029632.

Moen, J., Y. Rinne, H. C. Carlson, K. Oksavik, R. Fujii, and H. Opgenoorth (2008), On the relationship between thin Birkeland current arcs and reversed flow channels in the winter cusp/cleft ionosphere, *J. Geophys. Res.*,**113**, A09220, doi:10.1029/2008JA013061.

Moen, J., H. C. Carlson, Y. Rinne, and Å. Skjæveland (2012), Multi-scale features of solar terrestrial coupling in the cusp ionosphere, *J. Atmos. Sol. Terr. Phys.*, **87–88**, 11–19, doi:10.1016/j.jastp.2011.07.002.

Murphree, J. S., L.L. Cogger, C.D. Anger, D.D. Wallis, G.G. Shepherd (1987), Oval intensification associated with polar arcsGeophysical Research Letters, 14, p. 403

Nagai, T., M. Fujimoto, Y. Saito, S. Machida, T. Terasawa, R. Nakamura, T. Yamamoto, T. Mukai, A. Nishida, andS. Kokubun (1998), Structure and dynamics of magnetic reconnection for substorm onsets with Geotail observations, *J. Geophys. Res.*, **103**, 4419–4440.

Nagai, T., I. Shinohara, M. Fujimoto, M. Hoshino, Y. Saito, S. Machida, and T. Mukai (2001),Geotail observations of the Hall current system: Evidence of magnetic

reconnection in the magnetotail, J. Geophys. Res., 106(A11), 25929–25949, doi:10.1029/2001JA900038.

Nakamura, R., W. Baumjohann, R. Schödel, M. Brittnacher, V. A. Sergeev, M. Kubyshkina, T. Mukai, and K. Liou (2001), Earthward flow bursts, auroral streamers, and small expansions, J. Geophys. Res., 106(A6), 10791–10802, doi:10.1029/2000JA000306.

Nakamura, R., et al. (2005), Localized fast flow disturbance observed in the plasma sheet and in the ionosphere, *Ann. Geophys.*, **23**, 553–566, doi:10.5194/angeo-23-553-2005.

Neudegg, D. A., Yeoman, T. K., Cowley, S. W. H., Provan, G., Haerendel, G., Baumjohann, W., Auster, U., Fornacon, K.-H., Georgescu, E., and Owen, C. J.: A flux transfer event observed at the magnetopause by the Equator-S spacecraft and in the ionosphere by the CUTLASS HF radar, Ann. Geophys., 17, 707–711, 1999.

Newell, P. T., and D. G. Sibeck (1993), Upper limits on the contribution of flux transfer events to ionospheric convection, *Geophys. Res. Lett.*, **20**, 2829–2832, doi:10.1029/93GL02843.

Newell, P. T., Y. I. Feldstein, Y. I. Galperin, and C.-I. Meng (1996), Morphology of nightside precipitation, J. Geophys. Res., 101(A5), 10,737–10,748, doi:10.1029/95JA03516.

Newell, P. T., Sotirelis, T., Ruohoniemi, J. M., Carbary, J. F., Liou, K., Skura, J. P., Meng, C.-I., Deehr, C., Wilkinson, D., and Rich, F. J.: OVATION: Oval variation, assessment, tracking, intensity, and online nowcasting, Ann. Geophys., 20, 1039-1047, doi:10.5194/angeo-20-1039-2002, 2002.

Newell, P. T., T. Sotirelis, and S. Wing (2009), Diffuse, monoenergetic, and broadband aurora: The global precipitation budget, J. Geophys. Res., 114, A09207, doi:10.1029/2009JA014326.

Nishimura, Y., L. Lyons, S. Zou, V. Angelopoulos, and S. Mende (2010a), Substorm triggering by new plasma intrusion: THEMIS all-sky imager observations, *J. Geophys. Res.*, **115**, A07222, doi:10.1029/2009JA015166.

Nishimura, Y., et al. (2010b), Preonset time sequence of auroral substorms: Coordinated observations by all-sky imagers, satellites, and radars, *J. Geophys. Res.*, **115**, A00I08, doi:10.1029/2010JA015832.

Nishimura, Y., L. R. Lyons, S. Zou, V. Angelopoulos, and S. B. Mende (2011), Categorization of the time sequence of events leading to substorm onset based on THEMIS all-sky imager observations, in The Dynamic Magnetosphere, edited by W. Liu, and M. Fujimoto, pp. 133–142, Springer Netherlands, Dordrecht. [online] Available from: http://www.springerlink.com/content/x170k84772368516/.

Nishimura, Y., L. R. Lyons, T. Kikuchi, V. Angelopoulos, E. F. Donovan, S. B. Mende, and H. Lühr (2012), Relation of substorm pre-onset arc to large-scale field-aligned current distribution, *Geophys. Res. Lett.*, **39**, L22101, doi:10.1029/2012GL053761.

Nishimura, Y., L. R. Lyons, K. Shiokawa, V. Angelopoulos, E. F. Donovan, and S. B. Mende (2013), Substorm onset and expansion phase intensification precursors seen in polar cap patches and arcs, *J. Geophys. Res. Space Physics*, **118**, 2034–2042, doi:10.1002/jgra.50279.

Nishimura, Y., L. R. Lyons, X. Xing, V. Angelopoulos, E. F. Donovan, S. B. Mende, J. W. Bonnell, and U. Auster (2013), Tail reconnection region versus auroral activity inferred from conjugate ARTEMIS plasma sheet flow and auroral observations, J. Geophys. Res. Space Physics, 118,5758–5766, doi:10.1002/jgra.50549.

Nishimura, Y., et al. (2014), Day-night coupling by a localized flow channel visualized by polar cap patch propagation, *Geophys. Res. Lett.*, **41**, 3701–3709, doi:10.1002/2014GL060301.

O.A. Troshichev, M.G. Gusev, S.V. Nickolashkin, V.P. Samsonov (1988), Features of the polar cap aurorae in the southern polar region, Planet. Space Sci., 36, p. 429

Øieroset, M., T. D. Phan, M. Fujimoto, R. P. Lin, and R. P. Lepping, *In situ* detection of collisionless reconnection in the Earth's magnetotail, *Nature*, **412**, 414, 2001.

Oksavik, K., J. Moen, and H. C. Carlson (2004), High-resolution observations of the small-scale flow pattern associated with a poleward moving auroral form in the cusp, *Geophys. Res. Lett.*, **31**, L11807, doi:10.1029/2004GL019838.

Oksavik, K., J. Moen, H. C. Carlson, R. A. Greenwald, S. E. Milan, M. Lester, W. F. Denig, and R. J. Barnes (2005), Multi-instrument mapping of the small-scale flow dynamics related to a cusp auroral transient, *Ann. Geophys.*,**23**, 2657–2670.

Oksavik, K., V. L. Barth, J. Moen, and M. Lester (2010), On the entry and transit of high-density plasma across the polar cap, *J. Geophys. Res.*, **115**, A12308, doi:10.1029/2010JA015817.

Ono, T., T. Hirasawa, and C. I. Meng (1987), Proton auroras observed at the equatorward edge of the duskside auroral oval, Geophys. Res. Lett., 14(6), 660–663, doi:10.1029/GL014i006p00660.

Ono, T., T. Hirasawa, and C.-I. Meng (1989), Weak auroral emissions and particle precipitations in the dusk auroral oval, J. Geophys. Res., 94(A9), 11,933–11,947, doi:10.1029/JA094iA09p11933.

Østgaard, N., N. A. Tsyganenko, S. B. Mende, H. U. Frey, T. J. Immel, M. Fillingim, L. A. Frank, and J. B. Sigwarth (2005), Observations and model predictions of substorm auroral asymmetries in the conjugate hemispheres, Geophys. Res. Lett., 32, L05111, doi:10.1029/2004GL022166.

Panov, E. V., et al. (2010a), Plasma sheet thickness during a bursty bulk flow reversal, J. Geophys. Res., 115, A05213, doi:10.1029/2009JA014743.

Panov, E. V., et al. (2010b), Multiple overshoot and rebound of a bursty bulk flow, Geophys. Res. Lett., 37, L08103, doi:10.1029/2009GL041971.

Paschmann, G., G. Haerendel, I. Papamastorakis, N. Sckopke, S. J. Bame, J. T. Gosling, and C. T. Russell (1982), Plasma and magnetic field characteristics of magnetic flux transfer events, J. Geophys. Res., 87(A4), 2159–2168, doi:10.1029/JA087iA04p02159.

Pellinen, R. J., H. E. J. Koskinen, T. I. Pulkkinen, J. S. Murphree, G. Rostoker, and H. J. Opgenoorth (1990), Satellite and ground-based observations ofa fading transpolar arc, J. Geophys. Res., 95, 5817-5824.

Phan, T.-D. *et al.* Extended magnetic reconnection at the Earth's magnetopause from detection of bi-directional jets. *Nature* **404**, 848−850 (2000)

Phan, T. *et al.* Simultaneous Cluster and IMAGE observations of cusp reconnection and auroral proton spot for northward IMF. *Geophys. Res. Lett.* **30**, doi:10.1029/2003GL016885 (2003)

Pitkänen, T., A. T. Aikio, and L. Juusola (2013), Observations of polar cap flow channel and plasma sheet flow bursts during substorm expansion, *J. Geophys. Res. Space Physics*, **118**, 774–784, doi:10.1002/jgra.50119.

Prikryl, P., P. T. Jayachandran, S. C. Mushini, and I. G. Richardson (2012), Toward the probabilistic forecasting of high-latitude GPS phase scintillation, Space Weather, 10, S08005, doi:10.1029/2012SW000800.

Raeder, J., R. L. McPherron, L. A. Frank, S. Kokubun, G. Lu, T. Mukai, W. R. Paterson, J. B. Sigwarth, H. J. Singer, and J. A. Slavin (2001), Global simulation of the Geospace Environment Modeling substorm challenge event, J. Geophys. Res., 106(A1), 381–395, doi:10.1029/2000JA000605.

Rairden, R. L., and S. B. Mende, Properties of 6300-A auroral emission at south pole, J. Geophys. Res., 94, 1402,1989.

Rees, M. H., and D. Luckey (1974), Auroral electron energy derived from ratio of spectroscopic emissions 1. Model computations, J. Geophys. Res., 79(34), 5181–5186, doi:10.1029/JA079i034p05181.

Rees, M. H., G. J. Romick, H. R. Anderson, and R. T. Casserly Jr. (1976), Calculation of auroral emissions from measured electron precipitation: Comparison with observation, J. Geophys. Res.,81(28), 5091–5096, doi:10.1029/JA081i028p05091.

Rees, M. H., Stewart, A. I., Sharp. W. E., Hays, P. B., Hoffman, R. A., Brace, L. II.. Doering. J. P. and Peterson, W. K. (1977) Coordinated rocket and satebite measurements of an amoral event, I. Satellite observations and analysis. J. geophys. Rex 82, 2250.

Rees, H., R. G. Roble, Excitation of O(^1D) atoms in aurorae and emission of the [OI] 6300-Å line, *Canadian Journal of Physics*, 1986, 64:1608-1613, 10.1139/p86-284

Retino, A., et al. (2005), Cluster multispacecraft observations at the highlatitude duskside magnetopause: Implications for continuous and component magnetic reconnection, Ann. Geophys., 23, 461 – 473.

Richmond, A. D., and Y. Kamide (1988), Mapping electrodynamic features of the high-latitude ionosphere from localized observations: Technique, *J. Geophys. Res.*, **93**(A6), 5741–5759, doi:10.1029/JA093iA06p05741.

Rinne, Y., J. Moen, K. Oksavik, and H. C. Carlson (2007), Reversed flow events in the winter cusp ionosphere observed by the European Incoherent Scatter (EISCAT) Svalbard radar, *J. Geophys. Res.*, **112**, A10313, doi:10.1029/2007JA012366.

Robinson, R. M., R. R. Vondrak, E. Friis-Christensen (1987), Ionospheric currents associated with a sun-aligned arc connected to the auroral oval, Geophys. Res. Lett., 14, p. 656

Rodger, A. S., M. Pinnock, J. R. Dudeney, K. B. Baker, and R. A. Greenwald (1994), A new mechanism for polar patch formation, *J. Geophys. Res.*, **99**(A4), 6425–6436, doi:10.1029/93JA01501.

Runov, A., et al. (2003), Current sheet structure near magnetic X-line observed by Cluster,Geophys. Res. Lett., 30, 1579, doi:10.1029/2002GL016730, 11.

Ruohoniemi, J. M., and K. B. Baker (1998), Large-scale imaging of high-latitude convection with Super Dual Auroral Radar Network HF radar observations, *J. Geophys. Res.*, **103**(A9), 20797–20811, doi:10.1029/98JA01288.

Ruohoniemi, J. M., and R. A. Greenwald (2005), Dependencies of high-latitude plasma convection: Consideration of interplanetary magnetic field, seasonal, and universal time factors in statistical patterns, *J. Geophys. Res.*, **110**, A09204, doi:10.1029/2004JA010815.

RUSSELL, C. T. The Magnetospheres of The Earth and Jupiter edited by V. Formisano, pp. 39-53, D. Reidel Publishing Co., Dordrecht-Holland, 1975

Russell, C. T., and R. C. Elphic (1979), ISEE observations of flux transfer events at the dayside magnetopause, Geophys. Res. Lett., 6(1), 33–36, doi:10.1029/GL006i001p00033.

S. Ismail, D.D. Wallis, L.L. Cogger (1977), Characteristics of polar cap sun-aligned arcs, J. geophys. Res., 82, p. 4741

Sandholt, P. E., C. J. Farrugia, and W. F. Denig (2004), Dayside aurora and the role of IMF ｜By｜/｜Bz｜: Detailed morphology and response to magnetopause reconnection, *Ann. Geophys.*, **22**, 613–628, doi:10.5194/angeo-22-613-2004.

Sandholt, P. E., and C. J. Farrugia (2007), Poleward moving auroral forms (PMAFs) revisited: Responses of aurorae, plasma convection and Birkeland currents in the pre- and postnoon sectors under positive and negative IMF BY conditions, *Ann. Geophys.*, **25**, 1629–1652.

Saunders, M. A., Russell, C. T. and Sckopke, N. (1984), Flux transfer events: Scale size and interior structure. Geophys. Res. Lett., 11: 131–134. doi:10.1029/GL011i002p00131

Scholer, M.: Magnetic flux transfer at the magnetopause based on single X line bursty reconnection, Geophys. Res. Lett., 15, 291– 294, 1988.

Secan, J. A., R. M. Bussey, E. J. Fremouw, and S. Basu (1997), High-latitude upgrade to the Wideband ionospheric scintillation model, *Radio Sci.*, **32**(4), 1567–1574, doi:10.1029/97RS00453.

Sergeev, V. A., and N. A. Tsyganenko (1982), Energetic particle losses and trapping boundaries as deduced from calculations with a realistic magnetic field model, Planet. Space Sci., 30(10), 999–1006, doi:10.1016/ 0032-0633(82)90149-0.

Sergeev, V. A., E. M. Sazhina, N. A. Tsyganenko, J. A. Lundblad, and F. Soraas (1983), Pitch-angle scattering of energetic protons in the magnetotail current sheet as the dominant source of their isotropic precipitation into the nightside ionosphere, Planet. Space Sci., 31, 1147–1155, doi:10.1016/0032-0633(83)90103-4.

Sergeev, V. A., and B. B. Gvozdevsky, Mt-index: A possible new index to characterize the magnetic configuration of the magnetotail, Ann. Geophys., 13, 1093, 1995.

Sergeev, V. A., K. Liou, C.-I. Meng, P. T. Newell, M. Brittnacher, G. Parks, and G. D. Reeves (1999), Development of auroral streamers in association with impulsive injections to the inner magnetotail, Geophys. Res. Lett., 26, 417–420, doi:10.1029/1998GL900311.

Sergeev, V. A., J.-A. Sauvaud, D. Popescu, R. A. Kovrazhkin, K. Liou, P. T. Newell, M. Brittnacher, G. Parks, R. Nakamura, T. Mukai, and G. D. Reeves, Multiple-spacecraft observation of a narrow transient plasma jet in the Earth's plasma sheet, Geophys. Res. Lett., 27, 851 – 854, 2000.

Sergienko, T., Sandahl, I., Gustavsson, B., Andersson, L., Brändström, U., and Steen, Å.: A study of fine structure of diffuse aurora with ALIS-FAST measurements, Ann. Geophys., 26, 3185-3195, doi:10.5194/angeo-26-3185-2008, 2008.

Shi, Y., E. Zesta, L. R. Lyons, J. Yang, A. Boudouridis, Y. S. Ge, J. M. Ruohoniemi, and S. Mende (2012), Two-dimensional ionospheric flow pattern associated with auroral streamers, *J. Geophys. Res.*, **117**, A02208, doi:10.1029/2011JA017110.

Shi, Y., and E. Zesta (2014), Global-scale ionospheric flow and aurora precursors of auroral substorms: Coordinated SuperDARN and IMAGE/WIC observations, *J. Geophys. Res. Space Physics*, **119**, 4860–4871, doi:10.1002/2013JA019175.

Shiokawa, K., Y. Katoh, M. Satoh, M. K. Ejiri, T. Ogawa, T. Nakamura, T. Tsuda, and R. H. Wiens (1999),Development of optical mesosphere thermosphere imagers (OMTI), *Earth Planets Space*, **51**, 887–896.

Shiokawa, K., Y. Otsuka, and T. Ogawa (2009), Propagation characteristics of nighttime mesospheric and thermospheric waves observed by optical mesosphere thermosphere imagers at middle and low latitudes,*Earth Planets Space*, **61**, 479–491.

Sitnov, M. I., N. Buzulukova, M. Swisdak, V. G. Merkin, and T. E. Moore (2013), Spontaneous formation of dipolarization fronts and reconnection onset in the magnetotail, Geophys. Res. Lett., 40, 22–27, doi:10.1029/2012GL054701.

Sojka, J. J., M. D. Bowline, R. W. Schunk, D. T. Decker, C. E. Valladares, R. Sheehan, D. N. Anderson, and R. A. Heelis (1993), Modeling polar cap *F*-region patches using time varying convection, *Geophys. Res. Lett.*, **20**(17),1783–1786, doi:10.1029/93GL01347.

Solomon, S. C., P. B. Hays, and V. J. Abreu (1988), The Auroral 6300 Å Emission: Observations and Modeling, J. Geophys. Res., 93(A9), 9867–9882, doi:10.1029/JA093iA09p09867.

Song, P., and V. M. Vasyliūnas, Solar wind-magnetosphere-ionosphere coupling: Signal arrival time and perturbation relations, J. Geophys. Res., 107(A11), 1358, doi:10.1029/2002JA009364, 2002.

Söraas, F., H. R. Lindalen, K. Måseide, A. Egeland, T. A. Sten, and D. S. Evans (1974), Proton precipitation and the Hb emission in a postbreakup auroral glow, J. Geophys. Res., 79(13), 1851–1859, doi:10.1029/ JA079i013p01851.

Tsunoda, R. T. (1988), High-latitude F region irregularities: A review and synthesis, Rev. Geophys., 26(4), 719–760, doi:10.1029/RG026i004p00719

Tsyganenko, N. A. (2002a), A model of the near magnetosphere with a dawn-dusk asymmetry: 1. Mathematical structure, J. Geophys. Res., 107(A8), 1179, doi:10.1029/2001JA000219.

Tsyganenko, N. A. (2002b), A model of the near magnetosphere with a dawn-dusk asymmetry: 2. Parameterization and fitting to observations, J. Geophys. Res., 107(A8), 1176, doi:10.1029/2001JA000220.

Valladares, C. E., and H. C. Carlson Jr. (1991), The electrodynamic, thermal, and energetic character of intense Sun-aligned arcs in the polar cap, J. Geophys. Res., 96(A2), 1379–1400, doi:10.1029/90JA01765.

Valladares, C. E., H. C. Carlson Jr., and K. Fukui (1994), Interplanetary magnetic field dependency of stable sun-aligned polar cap arcs, J. Geophys. Res., 99(A4), 6247–6272, doi:10.1029/93JA03255.

Valladares, C. E., D. T. Decker, R. Sheehan, D. N. Anderson, T. Bullett, and B. W. Reinisch (1998), Formation of polar cap patches associated with north-to-south transitions of the interplanetary magnetic field, *J. Geophys. Res.*, **103**(A7), 14,657–14,670, doi:10.1029/97JA03682.

Weber, E. J., and J. Buchau (1981), Polar cap F-layer auroras, *Geophys. Res. Lett.*, **8**(1), 125–128, doi:10.1029/GL008i001p00125.

Weber, E. J., J. A. Klobuchar, J. Buchau, H. C. Carlson Jr., R. C. Livingston, O. de la Beaujardiere, M. McCreday, J. G. Moore, and G. J. Bishop (1986), Polar cap F layer patches: Structure and dynamics, *J. Geophys. Res.*, **91**,12,121–12,129, doi:10.1029/JA091iA11p12121.

Weiss, L. A., E. J. Weber, P. H. Reiff, J. L. Sharber, J. D. Winningham, F. Primdahl, I. S. Mikkelsen, C. Seifring, andE. M. Wescott (1993), Convection and electrodynamic

signatures in the vicinity of a Sun-aligned arc: Results from the polar acceleration regions and convection study (polar arcs), in Auroral Plasma Dynamics, *Geophys. Monogr. Ser.*, vol. 80, edited by R. L. Lysak, p. 69, AGU, Washington D. C.

Wernik, A. W., L. Alfonsi, and M. Materassi (2007), Scintillation modeling using in situ data, *Radio Sci.*, **42**, RS1002, doi:10.1029/2006RS003512.

Weygand, J. M., J. S. Murphree, M. G. Henderson, and G. A. Enno (2001), Simultaneous closed magnetic field line polar arcs and substorms, J. Atmos. Terr. Phys., 63, 643–655.

Wiens, R. H., and A. Vallance Jones (1969), Studies of auroral hydrogen emissions in west-central Canada, Can. J. Phys., 47, 1493–1503, doi:10.1139/p69-192.

Wing, S. and Zhang, Y. L.: The nightside magnetic field line open–closed boundary and polar rain electron energy-latitude dispersion, Ann. Geophys., 33, 39-46, doi:10.5194/angeo-33-39-2015, 2015.

Winningham, J. D., and W. J. Heikkila (1974), Polar cap auroral electron fluxes observed with Isis 1, *J. Geophys. Res.*, **79**(7), 949–957, doi:10.1029/JA079i007p00949.

Wygant, J. R., et al., Evidence for kinetic Alfvén waves and parallel electron energization at 4–6 *RE*altitudes in the plasma sheet boundary layer, J. Geophys. Res., 107(A8), doi:10.1029/2001JA900113,2002.

Xiao, F., Q. Zong, Y. Wang, Z. He, Z. Su, C. Yang, and Q. Zhou (2014), Generation of proton aurora by magnetosonic waves, *Sci. Rep.*, **4**, 5190, doi:10.1038/srep05190.

Xing, X., L. R. Lyons, V. Angelopoulos, D. Larson, J. McFadden, C. Carlson, A. Runov, and U. Auster(2009), Azimuthal plasma pressure gradient in quiet time plasma sheet, Geophys. Res. Lett., 36, L14105, doi:10.1029/2009GL038881.

Xing, X., L. R. Lyons, Y. Nishimura, V. Angelopoulos, E. Donovan, E. Spanswick, J. Liang, D. Larson, C. Carlson, and U. Auster (2011), Near-Earth plasma sheet azimuthal

pressure gradient and associated auroral development soon before substorm onset, J. Geophys. Res.,116, A07204, doi:10.1029/2011JA016539.

Xing, Z. Y., et al. (2012), Poleward moving auroral forms (PMAFs) observed at the Yellow River Station: A statistical study of its dependence on the solar wind conditions, *J. Atmos. Sol. Terr. Phys.*, **86**, 25–33.

Zesta, E., L. Lyons, and E. Donovan (2000), The auroral signature of earthward flow bursts observed in the magnetotail, *Geophys. Res. Lett.*, **27**(20), 3241–3244, doi:10.1029/2000GL000027.

Zesta, E., E. Donovan, L. Lyons, G. Enno, J. Murphree, and L. Cogger (2002), Two-dimensional structure of auroral poleward boundary intensifications, *J. Geophys. Res.*, **107**(A11, 1350), doi:10.1029/2001JA000260.

Zesta, E., L. Lyons, C.-P. Wang, E. Donovan, H. Frey, and T. Nagai (2006), Auroral poleward boundary intensifications (PBIs): Their two-dimensional structure and associated dynamics in the plasma sheet, J. Geophys. Res., 111, A05201, doi:10.1029/2004JA010640.

Zesta, E., et al. (2011), Ionospheric convection signatures of tail fast flows during substorms and Poleward Boundary Intensifications (PBI), *Geophys. Res. Lett.*, **38**, L08105, doi:10.1029/2011GL046758.

Zhang, Q. H., et al. (2013), Direct observations of the evolution of polar cap ionization patches, *Science*, **339**,1597–1600.

Zhu, L., J. J. Sojka, R. W. Schunk, and D. J. Crain (1993), A time-dependent model of polar cap arcs, J. Geophys. Res., 98(A4), 6139–6150, doi:10.1029/92JA01600.

Zhu, L., R. W. Schunk, and J. J. Sojka (1997), Polar cap arcs: A review, J. Atmos. Sol. Terr. Phys., 59, 1087-1126.

Zou, S., et al. (2010), Identification of substorm onset location and preonset sequence using Reimei, THEMIS GBO, PFISR, and Geotail, *J. Geophys. Res.*, **115**, A12309, doi:10.1029/2010JA015520.

Zou, Y., Y. Nishimura, L. R. Lyons, and E. F. Donovan (2012), A statistical study of the relative locations of electron and proton auroral boundaries inferred from meridian scanning photometer observations, *J. Geophys. Res.*, **117**, A06206, doi:10.1029/2011JA017357.

Zou, Y., Y. Nishimura, L. R. Lyons, E. F. Donovan, J. M. Ruohoniemi, N. Nishitani, and K. A. McWilliams (2014),Statistical relationships between enhanced polar cap flows and PBIs, *J. Geophys. Res. Space Physics*, **119**,151–162, doi:10.1002/2013JA019269.

Zou, Y., Y. Nishimura, L. R. Lyons, K. Shiokawa, E. F. Donovan, J. M. Ruohoniemi, K. A. McWilliams, and N. Nishitani (2015a), Localized polar cap flow enhancement tracing using airglow patches: Statistical properties, IMF dependence, and contribution to polar cap convection. J. Geophys. Res. Space Physics,120, 4064–4078. doi: 10.1002/2014JA020946.

Zou, Y., Y. Nishimura, L. R. Lyons, E. F. Donovan, K. Shiokawa, J. M. Ruohoniemi, K. A. McWilliams, and N. Nishitani (2015b), Polar Cap Precursor of Nightside Auroral Oval Intensifications Using Polar Cap Arcs. J. Geophys. Res. Space Physics, submitted

Zwickl, R. D., D. N. Baker, S. J. Bame, W. C. Feldman, J. T. Gosling, E. W. Hones Jr., D. J. McComas, B. T. Tsurutani, and J. A. Slavin (1984), Evolution of the Earth's distant magnetotail: ISEE 3 electron plasma results, *J. Geophys. Res.*, **89**, 11,007–11,012.